CARBON NANODOT: SELF-ASSEMBLY OF MOLECULAR FLUOROPHORES AND POTENTIAL APPLICATIONS

Thesis submitted in partial fulfillment

for the Award of Degree

Doctor of Philosophy

by

SURJA KANTA PAL

Department of Sciences & Humanities
RAJIV GANDHI INSTITUTE OF PETROLEUM TECHNOLOGY
JAIS, -229304

PC19-004 ***2024***

CERTIFICATE

It is certified that the work contained in the thesis titled **“Carbon Nanodot: Self-Assembly of Molecular Fluorophores and Potential Applications”** by **“Surja Kanta Pal”** has been carried out under my supervision and this work has not been submitted elsewhere for a degree.

It is further certified that the student has fulfilled all the requirements of Comprehensive, Candidacy, and SOTA.

Supervisor
Dr. Debashis Panda

DECLARATION BY THE CANDIDATE

I, “Surja Kanta Pal”, certify that the work embodied in this thesis is my own bona fide work and carried out by me under the supervision of **“Dr. Debashis Panda”** from “August 2019” to “December 2023”, at Rajiv Gandhi Institute of Petroleum Technology, Jais.

The matter embodied in this thesis has not been submitted for the award of any other degree. I declare that I have faithfully acknowledged and given credits to the research workers wherever their works have been cited in my work in this thesis. I further declare that I have not willfully copied any other’s work, paragraphs, text, data, results, etc., reported in journals, books, magazines, reports dissertations, theses, etc., or available at websites and have not included them in this thesis and have not cited as my own work.

Place: RGIPT
Date:

Surja Kanta Pal
Roll No.-PC19-004

CERTIFICATE BY THE SUPERVISOR(S)

It is certified that the above statement made by the student is correct to the best of my knowledge.

Dr. Debashis Panda
(Supervisor)

Prof. A. K. Choubey
(Head of Department, S&H)

CERTIFICATE

Certified that the work contained in the thesis titled **"Carbon Nanodot: Self-Assembly of Molecular Fluorophores and Potential Applications"** by **Mr. Surja Kanta Pal** has been carried out under my supervision. It is also certified that he fulfilled the mandatory requirement of TWO quality publications arose out of his thesis work.

It is further certified that the two publications (copies enclosed) of the aforesaid Mr. Surja Kanta Pal have been published in the Journals indexed by —

(a) SCI

(b) SCI Extended

(c) SCOPUS

(Supervisor)
Dr. Debashis Panda

(Convenor, DPGC)
Dr. Praveen Kumar Srivastava

COPYRIGHT TRANSFER CERTIFICATE

Title of the thesis: "Carbon Nanodot: Self-Assembly of Molecular Fluorophores and Potential Applications"
Name of the student: Surja Kanta Pal

Copyright Transfer

The undersigned hereby assigns to the Rajiv Gandhi Institute of Petroleum Technology, Jais all rights under copyright that may exist in and for the above thesis submitted for the award of the" Doctor of Philosophy".

Place: RGIPT
Date:

Surja Kanta Pal
Roll No. PC19-004

Dedicated to My Parents

Acknowledgement

“Life is like riding a bicycle. To keep your balance, you must keep moving.’’

Albert Einstein

It brings me immense pleasure to finally arrive at the moment when I can submit my doctoral thesis. But before I do, I take a special moment to thank ‘GOD’ for bestowing upon me all the favourable circumstances that allowed me to smoothly traverse this decisive path in my life. Additionally, there are several individuals whom I would like to express my gratitude to for their love, care, support, and efforts.

In particular, I extend my heartfelt appreciation to my doctoral thesis Supervisor, Dr. Debashis Panda, for his invaluable guidance, encouragement, academic stimulus, and generous assistance. I am deeply grateful for the numerous helpful discussions and suggestions I received during the thesis preparation process. I will always cherish his words, “A Ph.D. is not only a degree but a journey.”

I will not forget those enjoyable and enlightening discussions with my supervisors at each stage of my writing, which often extended for several hours. These discussions have ultimately led me to the completion of this thesis.

Beyond my supervisor, I would like to express my gratitude to the rest of my RPEC committee: Dr. Umaprasana Ojha and Dr. Milan Kumar, for their insightful comments and encouragement, as well as for posing challenging questions that prompted me to broaden my research from various perspectives.

I would also like to extend my thanks to my lab mates who are also my friends: Suvadeep, Prerna, Basab, Pooja, Utsav, Raman, Arvind, and Karan for the stimulating discussions and the positive lab environment we shared during our time working together over the past four years.

I would like to thank our BTP group and summer intern members Mohit Parashar, Arnab Mandal, Baldeep, Aritra Nandi, Amrit Kumar, Shivam, Sukpreet, Amulya, Chetna, and Kritika for their support as helping hands in the experiments.

I warmly extend my appreciation to my seniors: Dr. Suman Debnath, Dr. Subhankar Mandal, Dr. Ramesh Narikula, Dr. Shruti Bhardwaj, and my friends Ajeet, Yogendra, Vinamra, Rakesh, Chandan, Santosh, Dipak, Pralay, Ashish, Shrinkhala, Parvez, Taniya, Amit, Rituraj, for their help and support.

I take into account the remarkable collaboration and timely assistance provided by my friends: Prof. E Siva Subramaniam Iyer, Prof. Priyankar Paira, Vikas Jha, Nilmadhab Roy, Dr. Ujjawal Ghosh Da, Dr. Shyamal Kanti Bera Da, Dr. Souradipta Dasgupta Da, Dr. Soumen Payra Da, Dr. Atanu Betal, Dr. Surajit Panda, Dr. Shyamal Pramanik, Dr. Pran Gobinda Nandi.

I would like to express my heartfelt gratitude to the teachers who have been instrumental in shaping my academic journey at various stages of my life – from school to bachelors and postgraduate studies. Their unwavering support and motivation have been invaluable. I extend my appreciation to Kalipada Bankura sir, Goutam Chandra sir, Partharaj Misra sir, Dr. Subash Banerjee sir, Dr. Goutam Patra sir, and Dr. Pathik Maji sir.

I owe an immense debt to my beloved parents and family. Their enduring love, unwavering confidence, and constant support for my hard work have spurred me to advance in my studies and career. The boundless affection and encouragement from my parents have consistently propelled me forward. My father warmth has always filled me with peace and positivity. The support from my brother and sister has motivated me to reach unprecedented heights.

Last but certainly not least, my life is profoundly indebted to all my family members for their love, patience, support, and sacrifices. I would never have attained such heights without their blessing.

…. Surja Kanta Pal

Contents

Page

List of Abbreviations iv

List of Figures v

List of Schemes ix

List of Tables x

Preface xii

Chapter 1 **Page**

1.1. Introduction 1

1.2. Emerging Synthetic Method 5

1.3. Purification Technique 12

1.4. Optical Properties 13

1.5. Elemental Doping of CNDs and Emission Tunability 18

1.6. Applications 24

Chapter 2 ***Materials, Characterizations, and Synthesis Methods***

2.1. Materials 30

2.2. Experimental Techniques

2.2.1. UV-vis absorption spectroscopy 31

2.2.2. Steady-state fluorescence measurement 31

2.2.3. Determination of the fluorescence quantum yield 32

2.2.4. Time-resolved fluorescence measurements 33

2.2.5. Analysis of the fluorescence decay 34

2.2.6. Time-resolved fluorescence anisotropy 36

2.2.7. Transient absorption measurement 36

2.2.8. Fourier transform infrared (*FT-IR*) spectroscopy 37

2.2.9. *X*-ray photoelectron spectroscopy (*XPS*) 37

2.2.10. Field emission scanning electron microscopy (*FE-SEM*) 38

2.2.11. Transmission electron microscopy (*TEM*) 38

2.2.12. Small-angle X-ray scattering (*SAXS*) 39

2.2.13. Dynamic light scattering (*DLS*) 39
2.2.14. Elemental analysis (*CHNS*) 39
2.2.15. High resolutions mass spectroscopy (*HRMS*) 39
2.2.16. Nuclear magnetic resonance (NMR) 40

2.3. Synthesis Methods

2.3.1. Red (P^R) and green (P^G) emissive products 40
2.3.2. Methanol-directed transformation of the red emissive product ($P^{R\rightarrow G*}$) 41
2.3.3. Solvothermal reaction of gallic acid derived yellow emissive product 41
2.3.4. Description of the home-built flow reactor 42
2.3.5. Continuous method to synthesize yellow emissive product (P^Y) from pyrogallol 43
2.3.6. Preparation of fluorophore-doped PVA-PVP film 44
2.3.7. Preparation of fluorophore-doped PVDF film 44
2.3.8. Isolation of chloroplast and concentration determination of chlorophyll 45
2.3.9. Cell Culture 45
2.3.10. Protocol for Intracellular Co-localization study 46

Chapter 3 ***Connecting the Dots of Carbon Nanodot-Molecular Assembly***

3.1. Introduction 49

3.2. Results and Discussion

3.2.1. Product manipulation by solvent reactivity 53
3.2.2. Electrostatic sequestration by cationic surfactant 62
3.2.3. Switchability of red emissive product 65
3.2.4. Fast kinetics of Hill Reaction-Enhancing the photosynthesis 67
3.2.5. Fluorescent-tagging of protein 69
3.3. Conclusion 70

Chapter 4 ***Molecular Origin of Excitation-independent Emission of Carbon Nanodot***

4.1. Introduction 74

4.2. Results and Discussion

4.2.1. Excitation-Independent emission 77
4.2.2. Molecular identification by tracing the steps of solvent engineering 79
4.2.3. Corroborative evidences 83
4.2.4. Excited state emission dynamics-red edge effect 85
4.2.5. Proton-triggered aggregation-induced emission 88
4.2.6. Intracellular co-localization of product 90
4.2.7. Trivalent metal ion sensing ability 91
4.3. Conclusion 93

Chapter 5 ***Scalable and Sustainable Photoluminescent Self-assembly from Pyrogallol***

5.1. Introduction 97

5.2. Results and Discussion

5.2.1. Why is the coil-in-spiral reactor advantageous 101
5.2.2. Building of red emissive self-assembly in solution 103
5.2.3. Electrostatic sequestration by anionic surfactant 108
5.2.4. Exciton dynamics of self-assembly in solution 109
5.2.5. Structural basis of self-assembly 112
5.2.6. Mechanofluorescence by ordering aggregates in polymer 115
5.3. Conclusion 117

Chapter 6 ***Summary and Future Scope***

6.1. Conclusion 120
6.2. Future scope 122

Appendix 123
Reference 134
List of Publications 153
Participation in National and International Conferences 154

List of Abbreviations

Term	Meaning
ACQ	Aggregation Caused Quenching
CNDs	Carbon Nanodots
CA	Citric Acid
CTAB	Cetyltrimethylammonium bromide
SDS	Sodium dodecyl sulphate
U	Urea
PPDA	Para-phenylenediamine
AT	Ammonium Thiocyanate
EDDA	Ethylenediamine-N,N-diacetic acid
ETDA	2,2′-(ethylenedithio)diacetic acid
LED	Light emitting diode
DMF	N, N-dimethyl formamide
EA	Ethanolamine
FM	Formamide
BA	Boric Acid
CPDs	Carbonized Polymer Dots
EDTA	Ethylene diamine tetra acetic acid
SC	Sodium Citrate
ST	Sodium Thiosulfate
EDA	Ethylenediamine
Arg	Arginine
NDA	Naphthalene Dianhydride
THAM	Tris-(hydroxymethyl) amin
MW	Microwave
MWCNTs	Multi-walled carbon nanotubes
Cys	Cysteine
LG	Lemon Juice
TA	Thiourea
GT	Glutathione
HER	Hydrogen Evolution Reaction
OER	Oxygen Evolution Reaction
FWHM	Full width at half maxima
FRET	Forster resonance energy transfer process
ESA	Excited State Absorption
TAS	Transient Absorption Spectra
CE	Counter Electrode
SDS	Sodium dodecyl sulphate
p-PDA	*p*-phenylenediamine
CSR	Coil-in-spiral reactor
o-PDA	*o*-phenylenediamine
TCSPC	Time-correlated single-photon count
UNSDG	United Nations Sustainable Development Group
CNTs	Carbon Nanotubes

MOF	Metal-organic framework
HTC	Hydrothermal method
CTAB	Cetyltrimethylammonium bromide

List of Figures

Chapter 1		Page
Figure1.1	Important timeline of the Carbon Nanodots family based on fundamental understanding source of luminescent property. This timeline includes the discoveries of carbon nanodots (2004); Bright and colorful photoluminescence from surface passivation by polyethylene glycol (2006); Photoluminescent nanoparticle based on fullerene-silica hybridization (2009); Luminescent Carbon Nanodots: Emergent Nanolights (2010); Enhancing the luminescence of carbon dots with a reduction pathway (2011); Highly Photoluminescent Carbon Dots for Multicolor Patterning, Sensors, and Bioimaging (2013); Common Origin of Green Luminescence in Carbon Nanodots and Graphene Quantum Dots (2014); Carbon Dots: A Unique Fluorescent Cocktail of Polycyclic Aromatic Hydrocarbons (2015); Graphitic Nitrogen Triggers Red Fluorescence in Carbon Dots (2017); 53% Efficient Red Emissive Carbon Quantum Dots for High Color Rendering and Stable Warm White-Light-Emitting Diodes (2017); Full-Color Inorganic Carbon Dot Phosphors for White-Light-Emitting Diodes (2017); sp2–sp3 Hybridized Atomic Domains Determine Optical Features of Carbon Dots (2019); Toward Bright Red-Emissive Carbon Dots through Controlling Interaction among Surface Emission Centers (2020); Absorption and emission of light in red emissive carbon nanodots (2021)	4
Figure 1.2	Primary Synthesis Techniques for CNDs. Methods falling under the top-down category encompass arc discharge, laser ablation, chemical exfoliation, combustion, and electrochemical synthesis. On the other hand, bottom-up approaches consist of microwave, hydrothermal/solvothermal, thermal pyrolysis, ultrasound, and the MOF-assisted approach, respectively.	6
Chapter 2		
Figure 2.1	[A-B]. Experimental set-up for continuous synthesis and representative image of Coil-in-Spiral reactor.	42
Chapter 3		

Figure 3.1	[A] Solvothermal method employed with two different solvents-MeOH and DMF for the synthesis of fluorescent products. The products separated using a chromatographic method are placed in an ambient atmosphere and under irradiation at 530 nm (for P^R) and 405 nm (for P^G). [B-C] Absorption spectrum overlayed with excitation spectrum and steady-state emission spectra at different excitation wavelengths of-product, P^R (B), and P^G (C). [D] Time-resolved emission of products in methanol – P^R at 620 nm, P^G at 520 nm. Fitted line in yellow color. Solid grey line shows the Instrument Response function. [E] Time-dependent fluorescence anisotropy of products – P^R at 620 nm, P^G at 520 nm. Fitted lines are represented accordingly. TEM image of products- P^R [F] and P^G [G]; Inset - particle size distribution.	54
Figure 3.2	[A] FT-IR spectra, [B] Cyclic voltammetry, and [C] Full survey XPS spectra of red-emissive product, P^R (red line) and green-emissive product, P^G (green-line). High-resolution XPS of- [D] the C 1s core level, [E] the O 1s core level, and [F] N 1s core level of product, P^R, and P^G.	57
Figure 3.3	Optimized molecular structure of- [A] red emissive product, P^R and [B] green emissive product, P^G. The orientations of dipole moments are shown. The variation of the Stokes's Shift ($\Delta\nu$), quantum yield (ϕ_f), and average lifetime (τ_f) of products with the empirical micropolarity, E_T (30) - [C] red emissive product, P^R and [D] green emissive product, P^G The solvents used are Ethyl acetate (EA), Dimethyl formamide (DMF), ethanol, methanol, and water.	62
Figure 3.4	Emission spectra and Fluorescence decays of products in aqueous solutions at different concentrations of CTAB- [A, C] red emissive product, PR and [B, D] green emissive product, PG respectively. Variation of fluorescence quantum yield and average emission lifetime of- [E] product, P^R and [F] product, P^G.	63
Figure 3.5	Contour plot of emission spectrum with corresponding excitation wavelengths- [A] switched green product, $P^{R\rightarrow G*}$ and [B] green emissive product, P^G. [C] Fluorescence decay of products, $P^{R\rightarrow G*}$ (pink dots) and P^G (green dots). Fitted lines are shown accordingly. [D] Time-dependent fluorescence anisotropy of products, $P^{R\rightarrow G*}$ and P^G	66
Figure 3.6	[A] Absorption spectra of red emissive product (red line), isolated chloroplast (green line) and hybrid photosynthetic system i.e., chloroplast-red emissive product (pink line). Inset shows the color of corresponding solutions in an ambient condition. [B] Fluorescence spectra recorded at 510 nm excitation wavelength of red emissive product (red line), isolated chloroplast (green line) and hybrid photosynthetic system (pink line). Light harvesting activity of hybrid photosynthetic system. [C] Ferricyanide reduction assay of red emissive	68

	product (hollow circle), isolated chloroplast (green filled circle) and hybrid photosynthetic system (pink triangle).	
Figure 3.7	[A] Absorption spectra (red line), [B] Emission spectra (red line), [C] Fluorescence decay (red dots), and [D] SDS-gel electrophoresis of BSA-tagged red emissive product. [E] Absorption spectra (green line), [F] Emission spectra (green line) and [G] Fluorescence decays and [H] SDS-gel electrophoresis of BSA-tagged green emissive product. Fluorescence decay of unbound products are shown in grey dots for clarity and corresponding data of control experiments are also included for comparison purpose.	70
Chapter 4		
Figure 4.1	[A] Fluorescence spectra of product in ethyl acetate at different excitation wavelengths, [B] Emission spectra of products in various solvents, [C] Fluorescence decay traces at 580 nm emission wavelengths, λ_{exc}=405 nm. Water (blue dot), methanol (red dot), ethyl acetate (green color), tetrahydrofuran (THF). IRF is represented in grey scale.	78
Figure 4.2	[A] Full survey XPS spectra of product. The high resolution XPS of- [B] C 1s core level and [C] O 1s core level of the product. [D] N 1s core level of the product.	81
Figure 4.3	[A] ATR FT-IR spectra of- (i) Product (red line); (ii) gallic acid (cyan line). Comparison of Relevant stretching frequencies with that of computed value. [B] Molecular structure of the Product, and [C] the Protonated form of the product. The orientations of dipole moments are shown. [D] TEM image of product; Inset - particle size distribution, [E] HRTEM image of product with lattice spacing of approx. 0.22 nm (Inset).	84
Figure 4.4	[A] The fluorescence decays of product in ethyl acetate recorded over emission wavelengths at λexc=405 nm. [B] The time-resolved emission spectra of product in ethyl acetate. With the increase in delay-time, a second peak starts to emerge. The time-resolved area-normalized emission spectra (TRANES) of product in ethyl acetate- [C] between time 0 and 1 ns and [D] between time 2 ns and 20 ns.	86
Figure 4.5	[A] Absorption spectra of product in aqueous solution- without addition of acid (dark green line) and with acid (magenta line). Inset: color change of solution under ambient light. [B] The emission spectra recorded at various excitation wavelengths. [C] The fluorescence decays of product in acidic environment recorded over emission wavelengths, λexc=510 nm: [D] Zeta potential of product in water- in absence of acid (blue line) and with addition of acid (red line). Inset: schematic representation of molecular arrangements contributing to respective emissions. [E] TEM image of product; Inset - particle size	89

	distribution, [F] HRTEM image of product with lattice spacing of approx. 0.22 nm (Inset).	
Figure 4.6	Co-localization study of the products in colon cancer cell line HT-29. [A-B] Aggregated product of P. [C] product, P [D] Aggregated product of Product, P2.	91
Figure 4.7	[A] The absorption, and [B] fluorescence titration spectra of product with gradual addition of trivalent, aluminum ion (AlIII). [C] The Stern-Volmer plots of product at different concentrations of trivalent ions- AlIII (blue circle), FeIII (green circle), CeIII (red circle) where I0 and I are the fluorescence intensities of product without and with ions, respectively. KSV is the Stern Volmer constant and Q represents quenchers (i.e., metal ions). [D] Schematic representation – effect of increased size of metal ions on their binding affinity with product, color change visible even under ambient light	92

Chapter 5

Figure 5.1	Dependence of operating conditions – flow rate and temperature on product formation (% Yield). 2D projection of data sets	102
Figure 5.2	[A] Absorption spectrum (blue solid line) overlayed with excitation spectrum (green dashed line) of monomer, P^Y, [B] Contour plot of emission spectra with corresponding excitation wavelengths of monomer, P^Y in methanol. Inset –P^Y under ambient light. [C] Absorption spectrum (grey solid line) overlayed with excitation spectrum (red dashed line) of self-assembly (SA^R). [D] Contour plot of emission spectra with corresponding excitation wavelengths of self-assembly in methanol, SA^R. Inset – self-assembly under ambient light. [E] Time-resolved emission of products in methanol – P^Y at 560 nm, SA^R at 640 nm. Fitted line in blue color. Solid grey line shows the Instrument Response function. [F] Time-dependent fluorescence anisotropy of products – P^Y at 560 nm (red solid circles), SA^R (hollow green squares) at 640 nm in methanol. Fitted lines are represented accordingly.	106
Figure 5.3	[A-B] Temperature-dependent absorbance spectra and absorbance maxima at 450 nm & 630 nm of product P^Y. [C-D] Temperature-dependent fluorescence emission spectra and emission maxima at 580 & 650 nm of product P^Y. [E-F] Concentration-dependent absorbance maxima at 450 & 630 nm and fluorescence emission maxima at 580 & 650 nm of product P^Y.	107
Figure 5.4	Fluorescence Emission spectra and decays of products in aqueous solutions at different concentrations of SDS- [A, B] yellow emissive product, PY and [D, E] Self-Assemble red emissive product, SAR respectively. [C, F] Variation of fluorescence quantum yield, the concentrations of surfactant, SDS, and average emission lifetime of the	108

	products, PY and SAR respectively. The quantum yield and average lifetime are represented as filled triangles and filled circles.	
Figure 5.5	2D contour plot of transient absorption spectra of- [A] product, P^Y and [B] its self-Assembly (SA^R) respectively. The time axes are linear up to 10 ps and logarithmic thereafter. Time evolution of transient absorption spectra for- [C] product, PY and [D] its self-Assembly (SAR) respectively. Globally fitted lifetime spectra (EADS) of- [E] product, PY and its self-assembly (SA^R) respectively. Grey rectangles only block the pump scatter.	110
Figure 5.6	SAXS 2D scattering map of- [A] monomer, P^Y and [B] self-assembly, SA^R. [C] SAXS profiles of monomer (green squares) and self-assembly (red squares) in methanol. [D] SEM images of rod-like structures formed by trigonal pyramidal structures. [E] Isolated trigonal pyramidal structures of self-assembly. [F] Layer-by-layer stacking of triangular pyramid structure. [G] Molecular arrangements of different-sized triangular plates, Inset: Molecular structure of monomer highlighting origin of 120o angle. [H] Layer-by-layer stacking of triangular pyramid structure of Self-assembly.	113
Figure 5.7	[A-E] Growth of smaller triangular plate on top of a large-sized triangular plate, [F-H] SEM images of layer-by-layer stacking of self-assembly, SA^R	115
Figure 5.8	[A] Peak-Normalized Emission Spectra of Self-assembly doped polymer films. [B] Ratio of Intensities (Iintense peak /Ishoulder peak) for Self-assembly doped polymer films. [C] Representative photographs Self-assembly doped PVA-PVP films under axial states (I→ 0%, II→ 33.3%, III→ 70.4 %, IV→ 103.7%, and V→ 140.7%). Images of polymer films under Ambient light (blue strips) and under 530 nm irradiation (red strips). [D] Ratio of Intensities (I651 nm /I717 nm) at different stretching states of Self-assembly (0.062 mg/mL) doped (2%) PVA-PVP film (λexc = 630 nm).	116

List of Schemes

Chapter 1		**Page**
Scheme 1.1	General purification technique of the Carbon Nanodots	13
Chapter 2		
Scheme 2.1	Schematic representation of the synthesis of yellow emissive product from gallic acid, column chromatography, absorbance, and emission maxima in one non-polar solvent (THF), and polar solvent (H_2O) respectively	42

Chapter 3		
Scheme 3.1	Schematic representation of the solvent-directed synthesis of red and green emissive products with the same starting precursors (top). Routine practices and ad-hoc hypothesis of carbon nanodot research (bottom).	51
Scheme 3.2	Proposed reaction mechanism of the synthesized green emissive product, (P^{G})	59
Scheme 3.3	Proposed reaction mechanism of the synthesized red emissive product, (P^{R})	60
Scheme 3.4	Proposed reaction mechanism of the synthesized, $P^{R\rightarrow G^*}$ product.	67
Chapter 4		
Scheme 4.1	Schematic representation of the single-precursor strategy adopted in this work and the most common practices in carbon nanodot research, R is a reagent of interest.	76
Scheme 4.2	Proposed reaction mechanism of formation product, Aminohydroxy-substituted Xantheone (P) from the reaction of gallic acid and solvent, dimethyl formamide.	83
Scheme 4.3	Schematic representation of excited-state processes in the synthesized product in neat solvents.	87
Chapter 5		
Scheme 5.1	Highlighting the research gap in photoluminescent organic nanostructure by self-assembly of fluorophores. Our 360° approach: scalable synthesis, sustainable precursor, and light-harvesting applications.	99
Scheme 5.2	Schematic diagram of steps involved in the formation of self-assembly.	102
Scheme 5.3	Proposed reaction mechanism of synthesized product. This mechanism has been based on previous reports	104
Scheme 5.4	Excited state dynamics of Product, PY, and its self-assembly under optical pumping at 450 and 630 nm respectively. Under the 450 nm pumping, product molecules, PY are promoted to the high-lying excited Sn state and relax to the top of the S1 excited state (~ 2 ps component). Excited PY molecules can then get solvated (19 ps component). The 630 nm pumping promotes self-assembly to the top of the S1 exciton band. In this case, ~100 ps component is the relaxation time scale.	112

List of Tables

Chapter 1		
Table 1.1	Overview of the Elemental Doping, tunning of photoluminescent property and methods of different Carbon Nanodot Models.	22

Chapter 3		
Table 3.1	The average fluorescence lifetime of red emissive (P^R) and green emissive (P^G) products in MeOH solvent.	55
Chapter 4		
Table 4.1	Fluorescence decay parameters of synthesized fluorescent probe, P in various solvents. The excitation and emission wavelengths are- λexc = 405 nm, λems = 580 nm	79
Chapter 5		
Table 5.1	Steady-state and Time-Resolved Fluorescence Properties of Product and its Self-Assembly in MeOH solvent.	105

Preface

Scope of the Thesis: The serendipitous observation of excitation-energy-dependent photoluminescence from nanoscale carbon particles in 2004 has rejuvenated the search for solution-processed, biocompatible, and photoluminescent carbon quantum dots. Even over a decade in pursuit of photoluminescent carbon quantum dot has created opportunities and left a huge void in its fundamental understanding. Their applications cover the most demanding areas of research in recent times, such as bioimaging, light-emitting diodes, hydrogen gas production, and green fertilizers. The scope of the thesis is to deepen our fundamental understanding of Carbon Nanodot and simultaneously explore potential applications. The questions that I choose to answer in this thesis are-

(i) Why does carbon nanodot exhibit excitation-(in)dependent emission?
(ii) What is the role of the graphitic core in photoluminescence properties of carbon nanodot?
(iii) Is carbon nanodot an organic semiconductor or assembly of molecular fluorophores?

Chapter 1 *Introduction*:

It contains a detailed literature survey on carbon nanodot covering studies in solution and solid states, in-vivo and in-silico as well. Emerging synthetic methods, photoluminescent properties have also been presented. Elemental-doping of carbon nanodot and emission tunability of doped nanodots have been elaborated. An emerging perspective of photoluminescent molecular self-assembly such as J-aggregate, H-aggregates for organic electronics has been outlined. A wide range of applications such as cell-imaging, biomedical, organo-catalysis, light-emitting diodes, H_2 production, and CO_2 reduction have been illustrated.

Chapter 2 *Materials and Methodology*:

It includes a list of chemicals used, various equipment employed, synthetic methods, and chromatographic separation, spectroscopic and microscopic characterizations. Experimental setup for flow chemistry, photocatalysis, and time-correlated single photon counting have been included. Methods of spectroscopic and microscopic data analysis have been presented as well.

Chapter 3 *Connecting the Dots of Carbon Nanodot-Molecular Assembly*:

In this chapter, solvent reactiveness has been found to manipulate the emission properties of the products derived from a one-pot solvothermal reaction. The excellent superimposition of absorption and excitation spectra and excitation-energy-independent emission of green- and red-emissive products are suggestive of their molecular nature. The best-known graphitic-N in the carbon nanodot turns out to be the nitrogen of citrazinic acid. The synthesized emitters exhibit reverse solvatochromism, surfactant-induced aggregation, and electrostatic sequestration at the micellar surface. An unprecedented solvent-directed green switching of the red-emissive product (PR) has been presented here, and the transformed product (PR→G*) shows an uncanny resemblance of spectroscopic properties with the green-emissive product (PG). The products can easily bind to bovine serum albumin and retain their emissive properties in bound state, as signalled by the augmentation of fluorescence properties. Being a hybrid photosynthesis system, the chloroplast-red-emissive product is found to exhibit a markedly higher rate of reduction of ferricyanide than that of chloroplast alone.

Chapter 4 ***Molecular Origin of Excitation-independent Emission of Carbon Nanodot*****:**

In this chapter, a single-precursor approach has been adopted here for the synthesis of the yellow-fluorescent probe by using a bioresource, gallic acid. The synthesized probe exhibits excitation-energy-independent emission, a typical molecular behaviour, but shows an emission-wavelength-dependent lifetime that is often attributed to the red-edge effect most commonly observed for nanodots. It has been propose here that the observation of the red-edge effect for a synthesized probe in neat solvents is due to proton-transfer controlled solvation, a unique photo-process. Characterization and computational results of the synthesized product clearly suggest the formation of a molecular fluorophore. The presence of multiple phenolic-OH groups in the probe allows the easy formation of molecular chains of crystals on transmission electron microscopy grids, causing the observation of lattice spacing that remains unchanged in an aggregated state as well. It has been also explored its possible applications in bioimaging and trivalent metal ion sensing. It has better cell-membrane permeability but remains predominantly in the cytoplasm. The product molecule possesses a sub-micromolar detection limit for aluminium ions as well, further confirming the unaltered position of phenolic-OH groups present in the product and substrate.

Chapter 5 ***Scalable and Sustainable Photoluminescent Self-Assembly from Pyrogallol*****:**

In this chapter, the existing challenges in the development of self-assembly based on π-conjugated molecules have been addressed− (i) feeble photoluminescence caused by poor molecular orientational ordering, (ii) costly fluorescent monomer owing to lack of atom/step/energy economical synthetic method. A bright yellow fluorescent Xanthene analog capable of instantly forming self-assembly can be synthesized by a home-build coil-in-spiral reactor using an inexpensive precursor, pyrogallol has been synthesized. Stimuli such as temperature (35° C), acid fumes, and apolar solvent can trigger the formation of red-emissive self-assembly. In solution, the orientation of about 13 molecules yielding Hydrogen-bonded self-assembly has a direct resemblance with a Coulomb-coupled J-aggregate highlighted in the Kasha model. In the solid state, the self-assembly retains the submicron-sized trigonal pyramidal structures by layer-by-layer stacking of triangular plates. This self-assembly doped in polymer even exhibits mechanofluorescence.

Chapter 6 ***Summary and Future Scope*****:** In this chapter, results have been summarized and the future scope of the work has been outlined.

Chapter 1

Introduction

Detailed literature survey on synthesis of carbon nanodot and its optical properties, their broad applications have been presented in this chapter. Reported synthetic methodology using both the top-down and bottom-up approaches, and attempted purification methods of carbon nanodot through filtration, centrifugation, solvent dialysis, column chromatography, and electrophoresis have been outlined. The role of various steady-state and time-domain spectroscopic methods for monitoring of optical dynamics of nanodot have been elucidated. Widely reported emission tunable characteristics of nanodot through elemental (B, N, S, and P) doping has been emphasized. Potential applications in the areas of energy conversion, bio-imaging, metal ion sensing, and photocatalysis of carbon nanodot has been included in this chapter.

1.1. Introduction:

In the current scenario, the two most indispensable research areas are biomedical and renewable energy. Bio-imaging is a crucial part of medical research, similarly finding sustainable alternatives to conventional fossil fuels is an important step toward the United Nations Sustainable Development Group (UNSDG). For a long time, fluorescent semiconductor quantum dots have sparked considerable enthusiasm due to their potential applications in diverse fields, particularly in biology and medicine.[1] Yet, their recognized toxicity, fixed range of emission property, poor solubility in aqueous medium, and possible environmental risks in both laboratory and living organism applications pose significant constraints.[2,3,4] Consequently, there is a persistent quest for alternative nanomaterials with comparable optical characteristics that are safe and environmentally friendly.[5,6] However, in 2004, a new type of carbon-based nanomaterial was accidentally discovered. This material is highly biocompatible, exhibits bright fluorescent properties, and encompasses a wide range of spectra.[7,8] It is commonly known as Carbon Nanodot, carbon quantum dot, graphene quantum dot, or carbon dot.[9,10] Carbon nanodots have evolved through the years attributing to the extensive focus on their multi-faceted applications in biological imaging, biological sensing, drug delivery, gene delivery, fluorescent ink, anticounter fitting, metal-ion sensing, organic transformation reaction, LED, CO_2 reduction, metal-free photocatalysis to generate green hydrogen production.[9,11,10,12] Despite all the advancements, the origin of luminescent property is still not known. Many hypotheses have emerged as a result of the structural uncertainty of the carbon dot.[13] The initial hypothesis claimed carbon nanodot to be an allotrope of carbon with a shell-like structure and accredited the luminescent property to the surface state of the carbon core.[14,15,16] Another claimed that different types of fluorophores are present inside the carbon-core structure, followed by both core and surface being responsible for luminescence, and later size of the carbon dot was predicted to contribute to the varying fluorescence.[17,18,19,20,21,22] However, the debate of carbon dot being an aggregate or a molecule remains unsettled (Fig 1.1).[23,24,25] Further research is required to address the issues of fundamental understanding of the fluorescence and structure of the carbon dot.

A highly debated aspect of nanodot research revolves around the observation of excitation-dependent fluorescence. In the spectroscopic analysis, zero-dimensional CNDs exhibit excitation wavelength-dependent emission spectra, challenging the Kasha-Vavilov rule of molecular emission. Only a handful of research groups have managed to achieve an excitation wavelength-independent emission peak.[26,27,28,29] However, one question that remains inadequately addressed in the study of carbon nanodots is why they exhibit excitation-dependent emission spectra. From a material characterization perspective, CNDs represent a new type of zero-dimensional carbon allotrope, functioning as quasi-particles with an average size below 10 nm. They possess highly fluorescent properties with broad spectra in the visible range and are biocompatible.[9] The main contributing factor to the excitation wavelength-dependent emission spectra is the formation of spheres in different sizes.[21] The small size of the sphere results in blue emission, the medium size causes green emission, and the relatively large size produces red emission, all coexisting simultaneously.

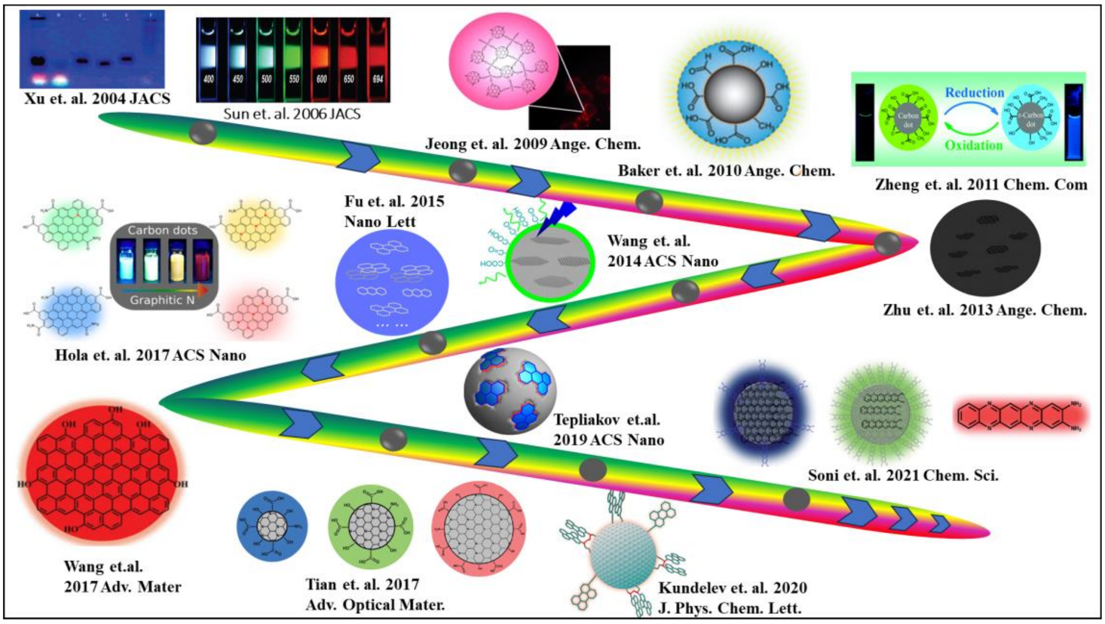

Figure 1.1: Important timeline of the Carbon Nanodots family based on fundamental understanding source of luminescent property. This timeline includes the discoveries of carbon nanodots (2004); Bright and colorful photoluminescence from surface passivation by polyethylene glycol (2006); Photoluminescent nanoparticle based on fullerene-silica hybridisation (2009); Luminescent Carbon Nanodots: Emergent Nanolights (2010); Enhancing the luminescence of carbon dots with a reduction pathway (2011); Highly Photoluminescent Carbon Dots for Multicolor Patterning, Sensors, and Bioimaging (2013); Common Origin of Green Luminescence in Carbon Nanodots and Graphene Quantum Dots (2014); Carbon Dots: A Unique Fluorescent Cocktail of Polycyclic Aromatic Hydrocarbons (2015); Graphitic Nitrogen Triggers Red Fluorescence in Carbon Dots (2017); 53% Efficient Red Emissive Carbon Quantum Dots for High Color Rendering and Stable Warm White-Light-Emitting Diodes (2017); Full-Color Inorganic Carbon Dot Phosphors for White-Light-Emitting Diodes (2017); sp2−sp3-Hybridized Atomic Domains Determine Optical Features of Carbon Dots (2019); Toward Bright Red-Emissive Carbon Dots through Controlling Interaction among Surface Emission Centres (2020); Absorption and emission of light in red emissive carbon nanodots (2021).

The unresolved question pertains to the type of sphere formed. Initially, literature predicted the formation of graphene-type spheres, but graphene lacks emission properties. Subsequently, it was suggested that nitrogen-doped graphene spheres are formed, evidenced by various elemental nitrogen peaks in XPS analysis. The increasing presence of nitrogen in the synthesis precursor leads to emissions ranging from blue to green and red.[30] What makes it particularly noteworthy is the ease with which carbon nanodots can be synthesized using a one-step process involving various reaction methodologies, employing simple and cost-effective polyol/poly acids and amine precursors. Alternatively, bioresource products such as various vegetables, bark, leaves, and waste materials can serve as carbon sources, elemental nitrogen sources, and single nitrogen-containing organic materials, all of which are sufficient to yield the same properties.[31, 32,33]

1.2. Emerging Synthetic Methods:

Over the last two decades, various methods have been proposed for the synthesis of carbon nanodots (CNDs). These approaches can typically be classified as "top-down" or "bottom-up" methods, and they may undergo adjustments either during the preparation phase or in post-treatment. In this discourse, I have explored the main techniques utilized in the production of CNDs.

A. Top-down Route:

In this strategy, CNDs can be synthesized from a variety of carbon-based raw materials such as activated carbon, carbon fibers, graphite, and allotropes of carbon such as graphene, CNTs, and fullerene through a variety of techniques.

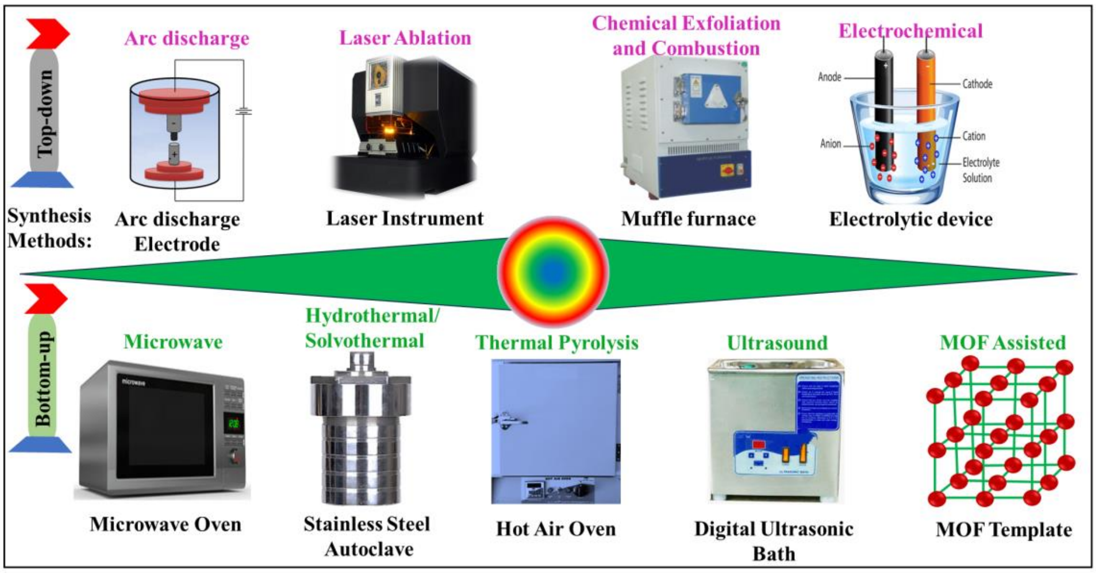

Figure 1.2: Primary Synthesis Techniques for CNDs. Methods falling under the top-down category encompass arc discharge, laser ablation, chemical exfoliation, combustion, and electrochemical synthesis. On the other hand, bottom-up approaches consist of microwave, hydrothermal/solvothermal, thermal pyrolysis, ultrasound, and the MOF-assisted approach, respectively.

1.2.1. Arc-Discharge Technique:

The arc-discharge technique is an energetic process where a bulk carbon source decomposes within an anode electrode. This occurs in the presence of plasma, created between two electrodes positioned at an ideal distance, all within a sealed reactor subjected to high voltage and high temperature reaches above 3000 ºC[34]. At this high temperature, carbon atoms evaporate from the anode, displaying intense fluorescence characteristics without requiring surface treatment[35] and also possible to elemental doping of boron and nitrogen from the source of diborane and ammonia respectively[36]. The drawback lies in the complexity of purifying CNDs produced through this method due to intricate impurities. Nonetheless, their particle size grows, resulting in a reduction of active reaction sites in the electrocatalytic process[10].

1.2.2. Laser-Ablation Technique:

Laser ablation is a well-established and sophisticated method for producing carbon nanodots with various shapes and structures[37,38].Sun and coworkers derived CNDs via laser ablation technique of a carbon target in the presence of water vapour with argon as a carrier gas at 900^{o}c and 75kPa. The produced sample, according to electron microscopy analyses, was dominated by nanoscale carbon particle in aggregated state of various size. There was no detectable photoluminescence from the sample and its aqueous suspension. The sample was refluxing HNO_3 for 12h after that also no detectable photoluminescent. However, upon the surface passivation by attaching simple organic species such as diamine-terminated oligomeric polyethylene glycol to the acid-treated carbon particles exhibit bright luminescent emission[7]. Hu *et. al.* reported the synthesis of fluorescent CNDs by laser irradiation of a suspension of carbon materials in an organic solvent[39]. Using selecting organic solvents, the surface states of the CNDs could be modified to achieve tuneable light emission. Based on control experiments, the origin of the luminescence was attributed to the surface states related to the ligands on the surface of the CNDs

1.2.3. Chemical Exfoliation and Combustion:

This method involves the creation of carbon nanodots (CNDs) by utilizing electrochemical processes to break down starting materials such as graphene, carbon nanotubes (CNTs), graphite rods, and graphene oxide. This method follows the radical mechanism to generate $H^{\bullet}$ and $OH^{\bullet}$ from oxidation of water in electrochemical reaction. The exfoliation process mainly started from edge side and after get accelerated at the defective side. For organic solvents the process of exfoliation depends on electric stress and continued intercalation of the anions between the layers of graphene. It means carbon nanodots are simply synthesized by the combustion method. Most of the waste raw materials such as paraffin putty, candle soot, and natural gas soot have been used with exhibiting multicolour fluorescence, water compatibility, and an average size below 2 nm[40]. The candle soot refluxed with nitric acid and combustion to prepare CNDs. Some important aspects are used in the combustion process- (a) fragmentation of aggregates of CNDs into nanosized carbon particles. (b) Surface modification to increase water dispersibility. (c) Fluorescence property modifications. Overall, this technique is used to synthesize strong fluorescence, high stability, better quality of purity, and promising materials for drug delivery, biosensors, bioimaging, and solar cell applications.

1.2.4. Electrochemical Technique:

This synthesis method is useful for economic and high productivity purposes in the synthesis of CNDs.[41,42,43] It was demonstrated by Zhou and co-workers to prepare deep-blue luminescent CND materials using a starting material of multi-walled carbon nanotubes (MWCNTs).[41] In this process after the synthesis of CNDs, which is degassed by acetonitrile with 0.1(M) tetrabutylammonium perchlorate to a three-electrode system consisting of working electrode of carbon paper with the chemical-vapour-deposited, counter electrode (CE) of platinum wire and a reference electrode of $Ag/AgClO_4$. One of the easy routes demonstrated by Lu *et. al.* is to obtain the same materials by using a graphite rod inserted as an anode in ionic liquid-assisted electrochemical exfoliation.[42] This setup was prepared by two different anodes, one is a graphitic rod and another one is highly oriented pyrolytic graphite, as two different experiments by using a platinum wire CE in 1-methyl -3-butyl imidazolium tetrafluoroborate and 1-methyl-3-butylimidazolium chloride ionic liquid electrolyte system. The synthesized CNDs exhibit uniform size distribution and high crystallinity and could potentially be used for chemical analysis and bio-related[44] applications.

B. Bottom-Up Approach:

In the bottom-up approach, generally organic molecules such as citric acid[45,46], chitosan, banana juice, lemon juice, saccharides[47-48,] and amine precursors are used as building blocks for the synthesis of CNDs. Under the bottom-up approach, the commonly used techniques of microwave synthesis, high pressure, and temperature-based solvothermal and hydrothermal, thermal pyrolysis, and pore-confined metal-organic framework as templates to synthesize CNDs are briefly explained below.

1.2.5. Microwave Synthesis:

In this technique, electromagnetic waves around 1 mm to 1m are used to break chemical bonds to prepare CNDs with an average size of less than 10 nm.[49,50] Zhu *et.al.* produced CND employing a microwave pyrolysis approach, using poly(ethylene glycol) and saccharides (glucose, fructose) as building blocks.[48] Glucose derived highly luminescent blue emissive, water-soluble, average size is below 2 nm, and white light generation CNDs prepared by microwave-assisted hydrothermal approach.[47] Zhai *et al.* promoted microwave-mediated pyrolysis of citric acid with various amine molecules to synthesize highly luminescent CND. The amine molecules, especially primary amine molecules, play dual functions as N-doping precursors as well as surface modification agents for the CND, which enhanced the photoluminescent property of the same. The Quantum yield values greatly increased with an increase of N content elements in CNDs fabricated from citric acid and 1,2-ethylenediamine.[49] The overall result of CNDs is highly biocompatible and has great potential for biomedical applications.[33]

1.2.6. Hydrothermal/ Solvothermal Synthesis:

One of the very simple methods, a low-cost, eco-friendly, easy scalability, and nontoxic route to produce novel carbon-based materials from hydrothermal or solvothermal carbonization using various precursors.[51,52] Typically a solution of organic precursor is sealed in a Teflon-coated stainless-steel autoclave reactor at high temperature (160-200 °C), whether water as a solvent in the hydrothermal or organic solvent used in the solvothermal reaction. CNDs prepared from HTC have many precursors such as glucose, citric acid, chitosan,[53] *o*-phenylenediamine,[51] banana juice, orange juice, and protein. Sahu *et. al.* prepared highly PL green color CNDs from orange juice and demonstrated them as an excellent probe in cellular imaging.[54] Yang *et. al.* reported highly amino-functionalized fluorescent carbon nanoparticles(CNDs) from the hydrothermal reaction of chitosan. The synthesized CNDs used in bioimaging of human lung adenocarcinoma cells exhibit low cytotoxicity and excellent biocompatibility.[53] Bhunia *et. al.* synthesized two types of CNDs, hydrophobic by fatty amine and hydrophilic with acid or water treatment of carbonization of carbohydrates. The synthesis product is used for biological staining and diagnostics.[55] CND synthesis via the one-step hydrothermal technique was also reported by utilizing glucose and monopotassium phosphate (KH_2PO_4).[56] To this method size of the CNDs and fluorescent properties are tunable by simply adjusting the concentration of monopotassium phosphate.

1.2.7. Thermal Pyrolysis:

Giannelis and colleagues were the first to showcase this method for the preparation of CNDs.[57] The synthesized surface-functionalized carbogenic nanoparticle exhibit unique optical property. The functionalized NPs are obtained in a single step of thermal decomposition of different ammonium citrate or 4-aminotipyrine. The average size of NPs is below 10 nm and highly dispersible in organic or aqueous solvents depending on modification of surface functionalization. The ammonium carboxylate moieties undergo thermal dehydration to form -NHCO-bonding between the organic network and cores. The same research gr. demonstrated the mechanism of formation of carbogenic CNDs via CA and ethanolamine(EA) pyrolysis under the influence of different temperatures. Under lower temperatures (at 180 ºC) of pyrolysis, the luminescence property is due to dehydration of CA-EA. Otherwise, in high temperatures like 230 ºC they noticed a formation of molecular fluorophores and carbogenic core, which collectively form the PL spectrum. Furthermore, temperature increases by 300 ºC to 400 ºC on pyrolysis they achieve PL property due to the carbogenic core.[58] It is one of the cost-effective, scalable techniques to prepare CNDs from abundant low-cost materials, encapsulation of this for biocompatible polymers makes them useful to biomedical applications such as bimodal imaging and drug delivery.[59]

1.2.8. Ultrasound Synthesis Technique:

This technique utilizes high-energy ultrasound vibration to prepare zero carbon nanomaterials in a very small-time gap and ambient conditions. For this case structurally modified CNDs of morphology, chemical composition, solubility, and aggregation[60]. Change in the formation of an acoustic cavity suddenly disrupts liquid bubbles as hydrodynamic cavitation is initiated by an intensive local pressure decrease due to supersonic liquid jets[61]. This exhibited a critical bubble formation which further induces the fragmentation of macro-size carbon materials to transformed CNDs.[62]

1.2.9. MOF Template-Assisted Approach:

MOFs are selective well-defined pores that used as templates for the synthesis of CNDs with average size below 5 nm and utilise wide range of applications in photocatalysis, sensor, bioimaging etc.[63,64,65] It is the latest approach first reported by Gu *et. al*.[66] In this study used the host templates of MOFs has three pore, approximately sizes from 1.35 nm to 3.4 nm. The MOF pores filled by glucose solutions and heated at high temperature (200 ºC). The selectively decompose the glucose filled in the MOF pores. Then collect the synthesized CNDs through the washing of MOF template by KOH solution. Similarly, Xiao and colleagues meticulously crafted arrays of chiral carbon nanodots (chirCND) through a controlled synthesis process. They achieved this by subjecting a chiral amino acid-loaded metal-organic framework (MOF) to low-temperature calcination, resulting in pronounced circularly polarized luminescence.[67]

1.3. Purification Techniques:

The obtained product from top-down or bottom-up methods contained a mixture of product, side product, and some unreacted precursors, which can be carbonized from, and condensed to small organic molecules, polymeric chains, and large organic or polymeric fragments. Thus, it should be effectively used for separated and purified forms before characterizations and applications. Most of the common separation and purification methods are used for synthesized CNDs as filtration, centrifugation, membrane dialysis, column chromatography, and gel electrophoresis.

Filtration and centrifugation are suitable for the separation of larger size particles or higher order agglomeration as a supernatant or precipitate of solid form in the presence of liquid product and similarly, remove side products of liquid form of small molecules from the target one. In dialysis selectively remove the small molecules or unreacted precursors due to their containing appropriate pore size of dialysis bag or membrane. This is a time-consuming process generally used as 6h, 9h, 12h, etc and distilled water is repeatedly used for the whole process. Column chromatography (CC) is one of the best techniques to properly purify molecular PL properties[68] or different types of aggregates and fluorophore purify separately.[25] Column chromatography utilized different pore sizes of silica gel as a stationary phase and different ratios of solvent (polar/ non-polar) mixture are used as a mobile phase. The mixture of products spread out in CC based on polarity and easily visualized the different colours of blue, green, yellow, orange, and so on. The electrophoresis separation technique is very rarely used for CND purification. The separation in electrophoresis relies on the speed affected by the charge, size, and shape of particles. Consequently, electrophoresis can distinguish between various sizes of CNDs, but the procedure is somewhat laborious.

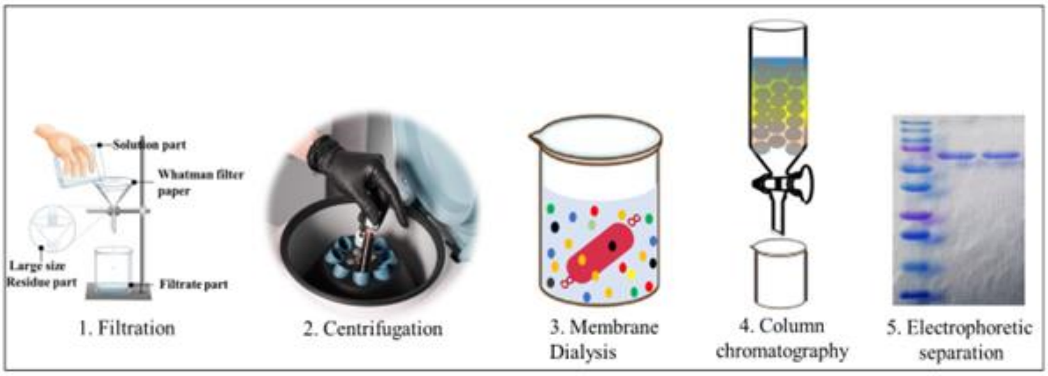

Scheme 1.1: General purification technique of the Carbon Nanodots

1.4. Optical Properties:

1.4.1. Absorption: Absorbance created by CNDs mainly due to their multiple conjugated forms of C=C pi-bond and the presence of hetero-atom (B/N/S/O/P) in conjugated form.[69,70] The transition can be π-π^* and n-π^* which is due to C=C, and C=O, C=N, C=S, C=P gr. etc present in a conjugated form or surface of functional groups.[71] Otherwise, an organic fluorophore of sp^2 hybridized carbon domain on the surface of the carbon core and sp^3 hybridized amorphous core by heteroatom doping.[23,72] The single peak at 255 nm and shoulder peak at 282 nm due to the corresponding π-π* transition of C=C and C=N bond respectively.[68] Based on the literature survey the CNDs typically exhibit two types of absorption maxima (A). Broad range of absorption maxima: In this case presence of a wide range of wavelength area covered by absorption spectra and which contains multiple absorption peak maxima depending on the expansion of pi-conjugation.[70] In conclusion, different types of heteroatom-doped graphene present in synthesized products or different sizes of carbon core states present in synthesized products.[30,25] Another one is (B). Single or two absorption peak maxima on the UV-Vis range. Which depends on PL property only one absorbance maxima peak over the whole absorption wavelength range.[45]

1.4.2. Fluorescence: The important feature of the CNDs is a broad range of excitation-dependent emission wavelengths and excellent intensity. Whether this occurs because of the optical selection of differently sized nanoparticles, different emissive traps on the CNDs surface or another mechanism is currently unresolved.[22] Moreover, the requirement for surface passivation is only partially understood but appears to be linked to the synthetic method. However, more and more cases have emerged with an excitation-independent emission position. Which may be attributed to their uniform size and surface chemistry.[25,11,57]

1.4.3. Phosphorescence:

The room temperature phosphorescence with a very long lifetime of about 380 ms and from blue CNDs embedded in a PVA matrix of solid state. Utilised the synthesis methodology of CNDs by pyrolysis of the Sodium salt of ethylenediamine tetra-acetic acid (EDTA-2Na) at 400C in an inert atmosphere. The product is bright blue in color to the naked eye and highly soluble in water.[73] The donor-acceptor energy transfer concept (EnT) based modulate aluminum phosphate zeolite framework of CNDs metrics synthesized by solvothermal method. Which can tune the behavior of blue emission of room temperature (RTP) with 22.32 ms in doping of heteroatom Zn and similarly doping of Mn metrics exhibit 1.184 ms of RTP of red emission. Here, the EnT process occurs between the Mn-doped zeolite and Zn-doped matrix as acceptor and CNDs as donor.[74] The combining of green CNDs and Rhodamine B (RhB) is confined into a hydrophilic silica shell to prepare a CNDs-Rh@silica nanocomposite of red emissive afterglow and near-infrared region luminous. The efficient energy transfer from donor CNDs to acceptor of rhodamine (RhB) via the Forster resonance energy transfer process (FRET).[75] Blue, green, yellow, and orange flexible phosphorescence films are produced by realizing the brighter triplet excitons of CNDs by embedding them into PVA matrices. In addition to PVA chains' ability to effectively isolate the CNDs, which prevents the transfer of electrons/energy from the triplet excited state and further protects the triplet excitons, created hydrogen bonds also play a critical function in controlling the vibration and rotation of the CNDs. Achieve Multicolour phosphorescence films have lifetimes that can be as long as 567, 1387, 726, and 311 ms.[76] Recently enhance the authentication of these signatures, artificial intelligence (AI) technology has been introduced, ensuring fast and accurate signature verification. The utilization of low-cost CNDs through hydrogen bonding to fibres-based phosphorescent ink, coupled with the 100% accuracy achieved through AI authentication, holds great promise for practical applications in real-life scenarios.[77]

1.4.4. Up-Conversion Photoluminescence (UCPL):

Göppert-Mayer introduced the multiphoton excitation theory in the 1930s, and its experimental validation occurred in 1961.[78,79] Following the development of the initial two-photon scanning microscope during the 1990s, multiphoton microimaging has emerged as a pivotal technique for visualizing intricate biological processes.[80] Under normal circumstances, a molecule typically absorbs one photon, transitioning from its ground state to an excited state. However, at sufficiently high light intensities, a phenomenon known as multiphoton transition takes place. This allows the simultaneous absorption of more than one photon, propelling the molecule to a higher energy state. Subsequently, after relaxation, the molecule undergoes a spontaneous transition, emitting a fluorescent photon at a frequency slightly lower than the combined frequencies of the incident light.[81] Multiphoton imaging offers distinct advantages over conventional techniques such as single-photon excitation fluorescence, laser-scanning confocal, and widefield imaging. It minimizes light-induced damage to biological samples, extends the effective observation period, enables deep tissue penetration, boasts a high fluorescence collection rate, and has minimal demands on optical path detection. This makes it well-suited for analysing complex multicomponent composites and showcasing exceptional optical sectioning capabilities. Therefore, multiphoton imaging stands out as an excellent choice for in vivo imaging.[82,83]

Up-conversion photoluminescence (UCPL) is a phenomenon known for its anti-stokes luminescence behaviour. In this process, a material is stimulated by low-energy, long-wavelength light and emits higher-energy, short-wavelength light. This contradicts stokes' law, which posits that materials typically absorb high-energy light and emit light of lower energy level. Unlike conventional luminescence, which involves just one ground state and one excited state, UCPL necessitates numerous intermediate states to accumulate energy from low-frequency excitation photons. This accumulation happens through the continuous absorption of individual photons or multiphotons.[84] Comparatively, UCPL differs from multiphoton photoluminescence, where multiple photons are absorbed simultaneously. In UCPL, it's more common for multiple photons to be absorbed successively.[85] In terms of the light source for excitation, multiphoton photoluminescence calls for a high-energy pulsed laser, whereas UCPL allows for the use of a lower-energy continuous laser.[86] Obtaining upconversion photoluminescence (UCPL) in zero-dimensional carbon nanomaterials (0D CNMs) can be challenging due to significant nonradiative processes.[87] In 2007, Sun and colleagues employed two-photon fluorescence to generate upconverting carbon nanodots (CNDs) from fullerenes.[83] They observed that CNDs derived from fullerenes outperformed CNDs (carbon nanodots) and NDs (nanodiamonds) in terms of UCPL. The remarkable UCPL exhibited by CNDs can be attributed to several factors, including their large absorption cross-section, effective intramolecular charge transfer facilitated by an extended π-conjugated CNDs system, and reduced energy consumption due to their small particle size. Much like multiphoton imaging, CNDs with UCPL properties are highly suitable for bioimaging applications. They possess the ability to deeply penetrate tissues, offer a narrow emission spectrum with minimal spontaneous fluorescence background and tissue damage. Additionally, they can serve various purposes such as long-lasting warning indicators, biomarkers for monitoring biological processes, aiding in drug therapy, supporting computerized tomography scanning, and enhancing magnetic resonance imaging (MRI).[85]

1.5. Elemental Doping of CNDs and Emission Tunability:

Numerous studies have explored the impact of introducing various elements like nitrogen, sulphur, and boron into carbon nanodots (CNDs) to tune their fluorescence properties. These heteroatoms can influence the optical properties, whether they are incorporated as functional groups on the outer surface of CNDs or embedded within the CNDs as dopants. Increasingly, researchers are turning to molecular modelling to gain insights into how functionalization or doping alters the optoelectronic behaviour of CNDs.[88,11,89] This computational approach also aids in rationalizing the most effective synthetic methods. Indeed, according to material perspective adjusting the band gap size holds significant significance in the field of optoelectronics, serving both technological purposes and contributing to the fundamental understanding of the underlying mechanisms responsible for such adjustments. The HOMO and LUMO energy gap of zero dimensional CNDs are calculated, based on the quantum confinement effect and surface energy trap mechanism.[90] In this mechanism primary focus depend on quantum confinement effect depend on long conjugated domains and edge.[91] Consequently, enlarging the size of sp^2-conjugated domains through the incorporation of highly electronegative heteroatoms can facilitate the $n-\pi^*$ transition and, as a result, reduce the energy gap.[92] Surface energy traps the significant role of surface states in determining the energy gap of 0D CNDs, with surface groups promoting electron transitions across energy levels.[93] To address these aspects, various synthesis and post-synthesis techniques have been developed as widely employed strategies. These methods include element doping, surface functionalization, and material co-assembly.[94,95,96] Furthermore, both the preparation and post-processing stages of 0D CNDs production using these methods offer opportunities for modification through element doping, surface functionalization, and material co-assembly.[97,98] Elemental doping one of the easiest techniques to intrinsically modify the optical property of 0D CNDs from visible to NIR region.[99,100,101] Doping can be used for single element or multiple elements in different type of presynthesis precursor.[102,103,104,105]

1.5.1. Role of the Nitrogen on luminescence property: Elemental doping with nitrogen is one of the most important aspects compared to other elements such as B, S, P, Si, or halogens, due to their electron-donating tendency to the sp^2, sp^3 hybridized network of CNDs or the formation of different types of aromatic heterocyclic fluorophore compounds that contribute to molecular heterogeneity.[106,107,108]. The extension of π-electron conjugation in the aggregated state or luminescent molecular states changes energy levels and promotes radiative combination. This improvement enhances the optical properties, as the emissive property can be tuned from the blue to the red region based on the percentage of N-doping, and the quantum yield increases. For this reason, N-doped CNDs are widely used in the field of optoelectronic devices, catalytic applications, and biological applications.[109,110]

To explore the role of N-and O-elemental doping in 0D CNDs by Sarkar *et. al.* performed a systematic TDDFT calculation study of one or two layers of pyrene and coronene model structure. It was predicted that the graphitic nitrogen is play major factor for red shift of absorption spectrum with compare to undoped model and explain that how to trigger the red emission of graphitic-N.[111,20] The results obtained align with Sudolská *et. al.* findings, where the two-layer model demonstrates a closer match to the experimental absorption spectra compared to the single-layer model. This implies that the average size of the π-conjugated regions in both the experimental and theoretical CNDs are similar. Models incorporating pyridinic, pyrrolic, and amino groups were projected to exhibit UV−vis absorption spectra akin to undoped CNDs, with a slight blue shift observed in the pyridinic case. While the primary focus was on investigating the impact of nitrogen atoms, the study proposed associating the absorption band within the 400−430 nm range with OH/COOH groups, which act as electron donors or withdrawers, and attributing absorptions beyond 400 nm to COOH groups.[112]

1.5.2. Role of the Oxygen on luminescence property:

Due to the way they are prepared in a solution, carbon nanodots (CDs), even when not doped with other elements, are not purely composed of carbon. Typically, their surface contains hydrogen and frequently features oxygen-containing functional groups like carboxyl, carbonyl, hydroxyl, or epoxy groups. The quantity and type of these groups vary based on the synthesis method, and they can be adjusted to not only influence the photoluminescence (PL) properties of the CDs but also other important characteristics like solubility and biocompatibility. The impact of oxygen on CD properties depends on the specific functional group's nature and its concentration, which, in turn, is determined by the synthesis process. Numerous studies have been conducted to comprehend these relationships.

1.5.3. Carboxyl Acid and Esters, Hydroxyl and Epoxy Groups:

Hola *et al.* demonstrated a straightforward pyrolysis approach for 2h at 270 °C to prepare both hydrophobic and hydrophilic carbon nanodots (CNDs) by subjecting three distinct gallate-based molecular precursors. Initially, they produced organo-dispersible CNDs from three gallic acid derivatives, each distinguished by varying alkyl chain lengths. This not only controlled the particle's lipophilicity/ Hydrophilicity but also its nano size in TEM Images. By converting the surface alkyl chains of the CNDs into carboxylate groups through a base hydrolysis process, they successfully obtained water-dispersible CNDs. Photoluminescence (PL) measurements revealed that the co-related emission significantly dominates in organo-dispersible CNDs and lauryl gallate to methyl gallate, propyl gallate deriver CNDs exhibit about 40 nm emission wavelength redshift.[113] The study conducted by Sudolska *et al.* delves into the examination of various oxygenated moieties (such as hydroxyl, carboxyl, and epoxy) on model Carbon Nano Dots (CNDs). These CNDs are configured as either single-layer or multi-layer structures of coronene and pyrene, each endowed with oxygenated functional groups. Their investigation utilizes TDDFT analysis, which primarily scrutinizes the collective and distinct influences of the functional groups, as well as considers factors like stacking interactions and solvent impact on the UV−vis spectra.[112]

Table 1.1 Overview of the Elemental Doping, tunning of photoluminescent property and methods of different Carbon Nanodot Models

Synthesis Method	**Precursor**	**Solv.**	**Fluorescence Property**	**Proposed Concept for Emission**	**Reference**
Solvothermal Treatment	CA+ U	DMF	Orange emissive CNDs And less Excitation dependent Emission.	Conjugated sp^2 domain controlling and Surface charge engineering.	Qu *et.al.* 2016[72]
Thermal Pyrolysis	CA+U	-	Blue and yellow emissive CNDs excitation dependent Emission	Core state: Core/edge/molecular/Surface band.	Sharma *et.al. 2017*[114]
Hydrothermal	U + p-PDA	H_2O	Blue, Green, Yellow and Red CNDs, Excitation Independent Emission	Degree of surface oxidation of CNDs.	Ding *et.al.* 2016[68]
Hydrothermal	(i). CA+AT (ii). CA+U	H_2O	EWDES EWIES	Size and surface state of sp^2 cluster of graphene.	Qu *et.al.* 2013[115]
Hydrothermal	CA+EDA	H_2O	EWDES	Polymer like CNDs of Carbon core and surface/molecule state.	Zhu *et.al.* 2013[17]
Refluxtion Treatment	CA + 3EDA	-	EWIES	2-Pyridon derivatives aggregated through π-π stacking and H-bonding interaction.	Das *et.al.* 2017[116]
Microwave assisted Hydrothermal	Arg + EDA	H_2O	EWDES	Carbon core of graphene and Surface state.	Arcudi *et.al.* 2019[31]
a). MW b).Electrochemical	CA + U Graphitic rods Graphene Oxide	-	EWDES for all cases	Edge state and graphitic core	Wang *et.al.* 2014[117]

c). Solvothermal					
MW	(a). CA + EA (b).CA+ THAM	H_2O	EWDES of both cases	-	Zhang *et.al*. 2016[50]
Synthesis Method	**Precursor**	**Solv.**	**Fluorescence Property**	**Proposed Concept for Emission**	**Reference**
Solvothermal Reaction	CA + U + FM	-	EWIES	N-Doped graphitic core	Hola *et.al.* 2017[30]
Hydrothermal	CA + L-Cys	H_2O	EWIES	Surface state	Dong *et.al.* 2013[26]
Hydrothermal	SC + ST	H_2O	EWIES at 440 nm	Homogeneous surface state	Xu et.al. 2014[118]
Hydrothermal	(a). LJ + TA (b). GT + TA	H_2O	EWIES of both cases	Two molecular fluorophore system	Kaleem *et.al.* 2018[71]
Heating	CA+EDDA+ETDA	H_2O	EWDES	N,S-Doped carbon framework	Do *et.al. 2016*[119]
Hydrothermal	Cys + CA	H_2O	EWIES	N, S-Doped carbogenic core and surface state	Zhang et.al. 2015[120]
Solvothermal	(I). CA + U (II).CA+BA + U	DMF	EWIES of orange and red CDs	Concept of graphitic-N vs Pyridinic-N of graphene.	Ghosh *et.al.* 2022[46]
Solvothermal	o-PDA	H_2O/ HCl	EWIES of red, EWDES of blue and green	Core states, edge/surface states, molecular states.	Soni *et.al.* 2021[25]

*EWDES=Excitation wavelength emission spectra and *EWIES=Excitation wavelength independent emission spectra

1.6. Applications:

1.6.1. Light-Emitting Diode:

The present market exhibits a significant demand for vibrant lighting, with LEDs playing a crucial role in fulfilling this need. Through the process of electron-hole recombination, LEDs effectively convert electrical energy into light energy, making them versatile in applications across lighting, electronic displays, and medical devices. As an organic material for LEDs, Carbon nanodots (CNDs) are gaining popularity due to their robust stability, cost-effectiveness, low toxicity, eco-friendly properties, and consistent fluorescence emission.[121] This marks a departure from traditional LEDs utilizing rare-earth phosphors and heavy-metal-based semiconductor quantum dots.[22] WLEDs are presently sought after for their energy efficiency, enduring performance, uniform luminosity, and environmentally friendly characteristics. Furthermore, luminescent films incorporating PVA-PVP and CNDs were developed to emit white light, where wide range of emission spectrum of CNDs used. The CNDs were synthesized through a straightforward one-step solvothermal reaction involving citric acid and ammonium-thiocyanate in a DMF medium for 24 hours at 160 °C.[29] The resulting polymer film not only offers mechanical support but also facilitates the proper dispersion of CNDs, safeguarding against solid-state quenching.

1.6.2. Bioimaging:

Bioimaging plays a crucial role in various scientific and biomedical fields by providing a means to visualize and comprehend biological structures, functions, and processes. Several reasons underscore the importance of bioimaging. It serves as a cornerstone in modern medicine and biological research, facilitating non-invasive visualization of living organisms. This capability offers insights into the intricacies of life across different scales, playing a pivotal role in enhancing diagnostics treatment, and our overall understanding of biology and medicine.[12,10,122] In this context, a gallic acid-derived stimuli-responsive red emission product has been developed from a yellow emissive precursor. Both products find application in bio-imaging. To comprehend the subcellular localization of the product, a co-localization study is conducted. An aggressive colorectal cell line is employed within the lower pH environment characteristic of cancer cells. The results demonstrate an excellent superposition of fluorescence emission from the products, indicating that the synthesized product and its aggregated form can easily traverse the cancer cell membrane and penetrate the interior of the cell.[123]

1.6.3. Metal ion Sensing:

Carbon nanodots are widely used as sensing probes in environmental pollution and biological systems due to their easily synthesized method, low cost, bright fluorescence properties, and fast sensing response. Their very small size, large surface area, and multiple functional groups result in reactive and highly sensitive carbon nanodots. These nanodots selectively interact with the surrounding environment, including solvents, temperature, acid/base, and metal ions, leading to changes in their optical properties, mainly turning on and off fluorescence intensity. Carbon nanodots (CNDs) are commonly employed for detecting cations and anions such as Pt^{2+}, Pd^{2+}, Au^{3+},[124] Hg^{2+},[125] Zn^{2+},[126] Fe^{3+},[127] $ONOO^{-}$,[128] and ClO^{-},[129] They can bind through surface groups like carboxyl, amino, and hydroxyl, forming coordination bonds or electrostatic interactions.[9] Yang et al. reported on-off fluorescence sensing of ethylenediaminetetraacetic acid (EDTA) and Zn^{2+} ions through the depassivation and repassivation of Z-CDs.[126] Additionally, orange-emissive CPDs can be used in pH-sensitive cotton cloth for wound pH monitoring of medical purpose via fluorescence and calorimetric changes. But selectively trivalent metal ions sensing is limited and huge challenges of science. Therefore, here developed a gallic acid-derived yellow emissive product that can be selectively binds with trivalent metal ions at a micro-molar level of sensitivity, enabling colorimetric detection.[130]

1.6.4 Photocatalysis:

The rapid growth of industrialization and economy as a result huge demands of consumption of fossil fuels, energy conservation, environmental issue, and climate problem. So, the exploration of renewable source to mitigate real problems is essential for global development. Newly developing carbon-based material CNDs widely applied on photocatalysis such as pollutant degradation mainly organic dyes[131,132] and metal ions,[133,134,135] water splitting,[136,137,138] CO_2 reduction,[138,139] organic synthesis.[140] CDs with nitrogen atoms located at the edge sites of the aromatic domains enable efficient interfacial electron transfer and further lead to an increased photo- catalytic hydrogen generation from water.[141,142] In generally, CNDs crossbred with nanomaterials like Fe_2O_3, g-C_3N_4 used as light absorber or electron acceptor in the hetero- junction to modified the photocatalytic performance but in this case major issue is solubility of nanomaterial.[143] In this context of investigation, the chloroplasts in plants are recognized for conducting photosynthesis through the absorption of sunlight. However, the chlorophylls within chloroplasts utilize only a specific segment of the solar radiation spectrum. Consequently, there is a continued focus in energy research on developing a hybrid photosynthesis system to enhance coverage and utilization of the full spectral range of solar radiation. This system often involves fluorescent molecules with biocompatibility and photocatalytic activity. The choice of a red-emissive product is favoured due to its superior coverage of the solar radiation spectrum, enhanced electrostatic interaction with the surfactant CTAB, and ease of binding with proteins while maintaining straightforward biophysical properties. In the context of investigating the photocatalytic activity of the hybrid system, the study specifically explores the chloroplast-red-emissive product combination, employing a model redox reaction from ferricyanide to ferrocyanide, mirroring the Hill reaction of photosynthesis where isolated chloroplasts release oxygen through water splitting under light and in the presence of an electron acceptor, ferricyanide.

Chapter 2

Materials and Experimental Methods

This chapter encompasses all the chemicals used throughout the experiment, providing detailed synthesis methods for citric acid-derived red and green emissive products. The synthesis of MeOH-directed green switching product obtained from the red emissive product, as well as the yellow emissive product derived from gallic acid has been presented. Additionally, the fabrication of home-built coil reactor for continuous and scalable synthesis of pyrogallol-derived products has been illustrated. The chapter also includes the extraction process of chloroplasts from spinach leaves, the preparation of fluorophore-doped polymer film, and various characterization techniques.

2.1. Materials

Citrazinic acid, PVDF (Polyvinylidene Fluoride) from Alfa Aesar, citric acid from Fisher Scientific, borax, $Al(NO_3)_3$, $9H_2O$ from Molychem, Anhydrous ferric chloride ($FeCl_3$), DMSO-d6 from Merck, Ethanol (EtOH) from CH Fine Chemicals, Gallic acid, pyrogallol, 3,4-dihydroxybenzoic acid, ammonium thiocyanate, Fumaric acid, guanidine hydrochloride, dimethylformamide, methanol (MeOH), ethyl acetate (EA), acetonitrile, acetyl chloride, hydrochloric acid, Triethanolamine (TEOA), Triethylamine(TEA), silica-gel 100–200 mesh, cetyltrimethylammonium bromide (CTAB), sodium dodecyl sulphate (SDS), poly vinyl alcohol (PVA), Cerium chloride ($CeCl_3$, $6H_2O$), and Whatman filter paper (pore size 125 mm) were obtained from SDFCL. All of the experiments were conducted using analytical-grade chemicals, without any further purification.

Type-1 water from the Millipore Direct-Q5 water purifier (18.2 mΩ) has been used throughout the experiments. Stainless steel capillary tube 304 from MP Jain Steel Tubing Solutions, Maharashtra, India, has been obtained.

2.2. Experimental Techniques:

2.2.1. UV-vis absorption spectrophotometry

The absorption spectra have been measured at room temperature on a LABINDIA UV 3200 spectrophotometer. The absorbance (A) of an absorber is defined as-

$$A = \log\left(\frac{I_0}{I}\right) = \varepsilon \times C \times l \qquad (2.1)$$

Where I_0 and I are the intensities of the incident light and transmitted light respectively, l is the path length (in cm) of the traversed light, C is the molar concentration of the absorber and Ɛ is the molar excitation coefficient at the specified wavelength. In all the experiments in the solution phase, the path length of the cuvette was 1 cm. 2 mL of the solvents were placed in both sides as the sample side and reference side for baseline correction. After that 20 µL of solvent decant from sample cuvette and the same amount was replaced by fluorophore solution and record the absorbance spectra. In the case of polymer films PVDF, PVA-PVP baseline correction was performed using a transparent glass slide placed in both sides. Then the luminescent polymer film was loaded on a glass slide and record the absorbance spectra. The absorbance of fluorophores is generally kept less than 0.1 for the solution state and below 0.6 for films.

2.2.2. Steady-state fluorescence measurement:

The fluorescence spectra were recorded using a Varian Cary Eclipse fluorescence spectrophotometer for capturing steady-state fluorescence spectra. A pulsed Xe-lamp served as the excitation source. Corrections for the spectral sensitivity of the photomultiplier (Hamamatsu R928) were applied to the fluorescence spectra. Bandwidths ranging from 5 nm to 10 nm were utilized. Measurements were conducted at a right angle to the incident light direction, and the fluorescence intensity was regulated by the excitation slit gap. Synchronous fluorescence studies were carried out by concurrently scanning the excitation and emission monochromators of the fluorimeter, maintaining a constant offset (20 nm) between the two. Concentration levels were consistently maintained to prevent the inner-filter effect.

2.2.3. Determination of the fluorescence quantum yield :

The fluorescence quantum yield (ϕ_f) is defined as the ratio of the number of photons emitted to the number of quanta absorbed as given by the following equation.

$$(\phi_f) = \frac{\text{number of emitted photons}}{\text{number of absorbed photons}} \tag{2.2}$$

The change in absorption was also taken into consideration (equation 2.3). The relative quantum yield of the samples of which absolute quantum yield to be determined were corrected by using the following equation.

$$(\phi_f) = \frac{\text{Area under the fluorescence specturm}}{1-10^{-\text{absorbance}}} \tag{2.3}$$

Here absorbance of the sample corresponds to the wavelength, at which the sample has been excited to record the fluorescence spectra. The absolute fluorescence quantum yield (ϕ_f) of the sample is defined as-

$$\phi_f = \frac{\phi_{rel}^{sample}}{\phi_{rel}^{ref}} \times \phi_f^{ref} \tag{2.4}$$

Where ϕ_{rel}^{sample}, ϕ_{rel}^{ref} is the relative quantum yield of the sample and reference respectively. ϕ_f^{ref} is the absolute quantum yield of reference.

The absolute fluorescence quantum yield (ϕ_f) of the sample is determined by the equation,

$$\phi_f = \phi_r \frac{\eta^2}{\eta_r^2} \frac{I}{A} \frac{A_r}{I_r} \tag{2.5}$$

where ϕ_r is the quantum yield of the reference, Coumarin 102, η is the refractive index of the solvent, I is the integrated fluorescence intensity, A is the absorbance at the excitation wavelength, 420 nm, and the subscript, r stands for the reference. Similarly, it has been taken another reference, Rhodamine-b the absorbance at the excitation wavelength, 540 nm.

2.2.4. Time-resolved fluorescence measurements:

After excitation with a pulsed laser, the excited fluorophore depopulates to the ground state with emission which is characteristic of an emissive state. In such a process the change in fluorescence intensity, I(t) with time (t) exponentially follows the following equation.

$$I(t) = I_0 \exp(-t/\tau) \tag{2.6}$$

Where I_0 is the initial intensity and τ is the fluorescence lifetime. The fluorescence lifetime, τ represents the average time spent by the fluorophore in the excited state before coming to the ground state. However, the excitation pulse should be considered as a δ-pulse.

The Time-Correlated Photon Counting Technique (TCSPC) measures the probability of a single emitted photon being detected at a time (t) after the excitation of the sample. This probability is calculated by sampling the emission resulting from a large number of excitation pulses. The probability p(t) for the detection of a single photon is taken as the intensity distribution I(t) of all emitted photons as a result of excitation. The excitation pulse is triggered with an electronic pulse. The delay between the excitation pulse and the emitted photon to arrive is back-calculated.

The schematic representation is shown in figure 2.1

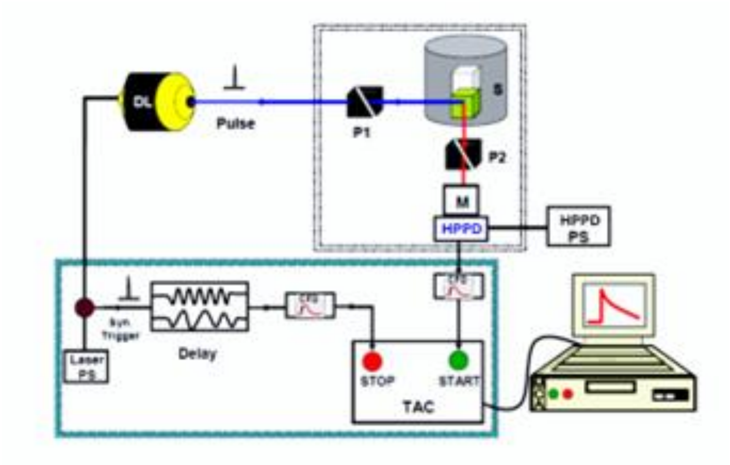

Figure 2.1: Time-correlated single photon counting setup for time-resolved fluorescence measurements. PS: Power supply, DL: Diode light source, P1: Excitation polariser, S: Sample chamber, P2: Emission Polariser, HPPD: High-performance photon detector, CFD: Constant fraction discriminator, TAC: Time to amplitude converter, MCA: Multichannel Analyzer.

The instrument response function (IRF) has been recorded using LUDOX as a scattering solution. All the measurements are performed by keeping the excitation polarizer at the vertical position and the emission polarizer at the magic angle (55°) concerning the excitation polarizer. The number of counts at the peak of the time-resolved fluorescence is kept between 6000 and 8000.

2.2.5 Analysis of the fluorescence decay:

The time-resolved fluorescence intensity function I(t) is fitted as a sum of n-exponentials as shown in equation (2.7), where τ_i and α_i are the lifetime and the corresponding pre-exponential factor (amplitude) of the i^{th} component.

$$I(t) = \sum_{i=1}^{n} \alpha_i e^{-t/\tau_0} \tag{2.7}$$

A major problem of analysis arises due to the fact the excitation pulse is not an δ-function pulse, rather it has a finite width. This complicates the decay profile considerably, especially for short fluorescence lifetimes. The observed time-resolved fluorescence N(t) can no longer be considered to be the true fluorescence response function I(t) from the sample, but is a convolution of the instrument response function R(t) and I(t) as is shown in the equation (2.8)

$$\mathrm{N(t)} = \int_0^t R(t' + \delta) I(t - t')\, dt \tag{2.8}$$

Where δ is the shift parameter. The instrument response function (IRF) of having finite width can be considered as a sequence of δ-functions, each producing its own fluorescence decay. The observed fluorescence profile is simply the sum of the responses to these δ-function responses. The shift is necessary because of the instrument response function is measured at a wavelength near to the excitation wavelength whereas fluorescence is detected at a wavelength far away from the excitation. As the time response of the detector (photomultiplier) depends upon the wavelength (due to the wavelength dependence of the energies of the electrons ejected from the photocathode), the arrival of the signal at TAC (time-to-amplitude converter) from the PMT is wavelength-dependent and hence the shift parameter is necessary in the analysis. Represent a block diagram for TCSPS measurements-

The deconvolution is done by an iterative deconvolution method to determine the pre-exponential factors and lifetimes. Ez-time program first generates a set of guess values for the amplitudes and lifetime depending upon the time scale of decay to be fitted. For each value of amplitudes and lifetimes, the program then yields the decay profile, convolutes it numerically with the instrument response function collected experimentally, and then, compares the generated curve with the experimentally observed decay, using nonlinear regression. The values of the parameters are adjusted in successive iterations till a good fit is obtained, i.e. convergence is achieved. The goodness of the fits is judged by the closeness of the value of the reduced χ^2 to unity. χ^2 being defined as

$$\chi^2 = \frac{1}{n-p}\sum_{k=1}^{n} \frac{[N[(t_k) - N_c(t_k)]^2}{\sigma_k^2} \approx 1.0 \tag{2.9}$$

where $N(t_k)$ and $N_c(t_k)$ are the experimental and calculated values of time-resolved fluorescence intensity at time t_k, k being the number of data points fitted and p is the number of free parameters in the equation. σ_k is the standard deviation associated with the i^{th} data point and is defined as in equation 2.10 (based on Poisson statistics).

$$\sigma_k = \sqrt{N(t_k)} \tag{2.10}$$

The goodness of the fit is also judged by the randomness of the weighted residuals of the experimental data with that of the calculated data. The weighted residuals $r(t_k)$ of the data are defined as

$$r(t_k) = \frac{N(t_k) - N_c(t_k)}{\sigma_k} \tag{2.11}$$

For best-fitted experimental data, the weighted residuals $r(t_k)$ should be distributed randomly about zero.

2.2.6. Time-resolved fluorescence anisotropy:

The time-dependent anisotropy, r(t), is constructed from the decays at parallel and perpendicular directions to that of the excitation polarization $I_{||}(t)$ and $I_{\perp}(t)$ respectively as-

$$r(t) = \frac{I_{||}(t) - GI_{\perp}(t)}{I_{||}(t) + 2GI_{\perp}(t)} \tag{2.12}$$

The G factor is calculated from the tail matching of the decays. The decays of r(t) are fitted to single and multiexponential functions as required, using the formula-

$$r(t) = r_0 \sum_i a_i exp\left[-\frac{t}{(\tau_r)_i}\right] \quad (2.13)$$

Where r_0 is the anisotropy at time t=0, $(\tau_r)_i$ is the rotational correlation time and a_i is the amplitude of the ith species. The initial anisotropy r_0 is related to the angle (δ) between the absorption and emission dipoles of the fluorophore and the relation is given in equation as

$$r_0 = \frac{2}{5}\left(\frac{3\cos^2\theta - 1}{2}\right) \quad (2.14)$$

The value r_0 can vary between 0.4 and -0.2 as the angle (θ) varies between 0° to 90° respectively.

2.2.7. Transient Absorption Measurement:

Femtosecond Transient absorption measurements has been performed on a Helios fire transient absorption spectrometer (Ultrafast systems, USA) to ascertain the excited state dynamics of monomer, $P^{Y,}$ and its self-assembly, SA^R. The stock solution of P^Y and SA^R are diluted using ethanol bought from Simson pharma to get an absorbance of 0.25 at the excitation wavelength of 450 and 630 nm in a cuvette of path length 2 mm, respectively. The pump pulses are generated using Opera Solo OPA (Coherent, USA) pumped by 35 fs, 1.5 mJ/pulse centred at 800 nm light produced from Astrella Amplifier operating at 1kHz. A broadband probe light is generated by focusing a fraction of the amplified output on the CaF_2 or Sapphire window. The monomer and its self-assembly are irradiated with 450 nm and 630 nm, respectively. The pulse energy used is ~ 150 nJ per pulse. The samples are stirred throughout the measurement with a magnetic stirrer. The sample integrity is being checked by measuring absorption spectra at various intervals during the experiment. The transient absorption spectra are analysed using Surface Xplorer (v4).

2.2.8. Fourier Transform Infrared (FT-IR) spectroscopy:

The Perkin Elmer Spectrum Two FT-IR spectrometer was used to record the FT-IR spectra of the vacuum-dried samples. The samples were recorded using "attenuated total reflectance" (ATR) mode. The PIKE MIRacleTM single reflection horizontal ATR accessory is used for recording the FT-IR spectra. This technique was employed for the identification of functional groups present in the synthesized product. The apply of stretching and bending vibrational modes correlated to confirm the presence of the functional group in CNDs as N–H, COO–H, O–H, C–H, S–H, C=O, SCN, C=C, C–N, C–O, C–S, C–O–C, etc.

2.2.9. X-ray Photoelectron Spectroscopy (XPS):

This technique was carried out by using a Thermo-Scientific K-Alpha X-ray photoelectron spectrometer with an Al Kα micro-focus monochromatic X-ray source and ultra-low energy electron flood gun. The sample was drop-casted on a thin glass slide and dried before measurements. The pass energy for survey spectra is 200 eV. A 50-eV pass energy was used for high-resolution, element-specific XPS spectra. Spectra are analysed with Advantage XPS software. Used this technique to understand the elemental composition and high-resolution scan to predict the bonding environment of synthesized product. Where O1s at 532±3 eV is an elemental peak and the corresponding bonding environment are C=O, C–O, C=C, C–O–C, C1s at 285±3 eV and corresponding chemical environment are C=C, C–N/C–O, C=O, N1s at 400±2 and corresponding bonding environment is amine, ammonium, citrazinic-N, pyrrolic-N.

2.2.10. Field-Emission Scanning Electron Microscopy (FE-SEM):

Performed FE-SEM, JSM7900F (Jeol Ltd.) with an EDAX system has been used to image the samples, line-scanning, and elemental mapping. Samples are prepared by drop-casting of the solution on copper tape and dried by using a vacuum oven. This technique was employed to determine particle size (100 nm to 1μm), shape, and elemental composition of the synthesized product.

2.2.11. Transmission Electron Microscopy (TEM):

The samples were imaged by a high-resolution transmission electron microscope (HR-TEM FEI, Tecnai G2, F30) mounted with field emission gun FEG TEM at 300 kV accelerating voltage. The samples for TEM were prepared on amorphous carbon films supported on a copper//nickel grid. The average values were expressed as mean ± standard deviation (SD). This technique is employed to identify the nano range of particle size average below 10 nm and corresponding lattice spacing 0.22 nm, or 0.25 nm.

2.2.12. Small-angle X-ray scattering (SAXS):

This spectroscopic technique can be utilized to easily differentiate the presence of molecular and aggregated states in synthesized products. For that purpose, Studied the Xeuss 3.0 (XENOCS S.A. France) with an advanced beam stop-less Q-zoom acquisition system. A 30 W Cu X-ray source is used for the measurements with a single photon counting hybrid pixel Pilatus with temperature 301 K and the distance between sample to detector is kept at 1.5 meter. It has been taken liquid sample of monomer and acid treatment product in two different capillaries (length- 80 mm and wall thickness-0.01 mm) and the total run time is 10 min.)

2.2.13. Dynamic Light Scattering (DLS):

This technique was used to measure the hydrodynamic diameter of synthesized product. Similarly, it's employed for the surface charge of nanoparticles in aqueous medium, i.e., zeta potential. I have done Zetasizer Nano ZS (Malvern Instruments Limited, U.K.) was used to measure the average hydrodynamic diameter and zeta potential of the samples. A 633 nm He/Ne laser is the light source, and the scattered light is detected at an angle of 173°. Measurements are performed at 25 °C using the appropriate sample dilution to minimize the undesired scattering events. The average value for each sample is obtained from 10 measurements.

2.2.14. Elemental Analysis(CHNS):

The percentage of elements present in the synthesized product can be determined by this technique. This technique is used to determine % N, %C, %H, and %S. For this experiment, a properly dried (2-5) mg sample was packed in an aluminum pocket and put into a series of holders containing the elemental instrument.

2.2.15. High Resolutions Mass spectra (HRMS):

This characterization to identify the molecular weight of the synthesized product. QTOF I (quadrupole hexapole- TOF) mass spectrometer with an orthogonal Z- spray-electrospray interface on Micro (YA-263) mass spectrometer (Manchester, UK). The sample for the GC experiments was prepared from the crude reaction solutions (MeOH) obtained by adding pure solid product. From this homogeneous solution 1.0 μL was injected into the GC-MS instrument for analysis.

2.2.16. Nuclear Magnetic Resonance Spectroscopy (NMR):

This spectroscopic instrument was employed to identify the chemical surroundings of an atom and functional groups to predict the molecular structure. ^{13}C NMR, ^{1}H-NMR spectra were recorded on a JEOL-400 YH NMR spectrometer at 25 °C probe temperature with DMSO-d6 solvent.

2.3. Synthetic Methods:

2.3.1. Synthesis and purification method of Red(P^R) and Green(P^G) emissive product:

In a typical synthesis, citric acid is dissolved in either dry DMF or methanol, followed by borax and ammonium thiocyanate under constant sonication. The transparent solution is then transferred to a Teflon-coated stainless-steel autoclave (purchased from M/S Shilpa Enterprises, Nagpur, India) for solvothermal reaction at 160 °C followed by incubation for 24h. After cooling the solvothermal reaction product to room temperature, the color of the solution changes to deep red from colourless for solvent DMF, whereas the solution turns dark greenish yellow for methanol. The respective colored solution is then filtered out using Whatman filter paper (pore size 125 mm), filtrate part washout several times by 2:1 ratio of EA and EtOH, and collect the supernatant part through centrifugation. Then supernatant part was dissolved in MeOH solvent and passed through the column chromatography for separation. Thus, the product obtained in the DMF-based method exhibits a bright pink color, whereas that obtained in methanol is bright green in color. The solution is passed through a 0.2 mm syringe membrane filter before characterizations and other studies.

2.3.2. Methanol-Directed Transformation of the Red-Emissive Product ($P^{R\rightarrow G*}$):

100 mg of the purified solid red product is dissolved in dry MeOH through sonication. The bright pink solution is then transferred to a Teflon-coated stainless-steel autoclave at 160 °C for solvothermal reaction and then incubated for 24 h. After cooling the reaction mixture to room temperature, the pink-colored solution turns green. The product obtained is diluted by 20 mL of ethyl acetate and centrifuged at 6000 rpm for

10 min. The supernatant is collected and purified through column chromatography with silica gel as the stationary medium through a ternary solvent mixture. The optical properties of the switched product have been studied by spectroscopic methods.

2.3.3. Solvothermal rection of Gallic Acid derived bright yellow emissive product in DMF and separation:

In a typical synthesis, 0.4 g of gallic acid monohydrate is dissolved in 10 mL of dry DMF (Scheme S1). The transparent solution is then transferred into a Teflon-coated stainless-steel autoclave at 160ºC and incubated for 24 hours. After cooling to room temperature, the color of the solution obtained from the solvothermal reaction is changed to dark yellow from colourless. The colored solution is then added into 30 mL of binary mixture (1:2) of solvents- petroleum ether and ethyl acetate. The diluted solution is thoroughly mixed and filtered to remove large particles. Thereafter, the solution is passed through a column containing silica (100-200 mesh) as a stationary phase and eluted using a ternary mixture (4:4:2) of solvents- DMF, EtOH, and EA. The collected sample is clear bright greenish-yellow in color. The solution has been passed through a 0.2 μM syringe membrane filter prior subjected to characterization methods- optical spectroscopic, dynamic light scattering, mass spectrometry, and all other measurements.

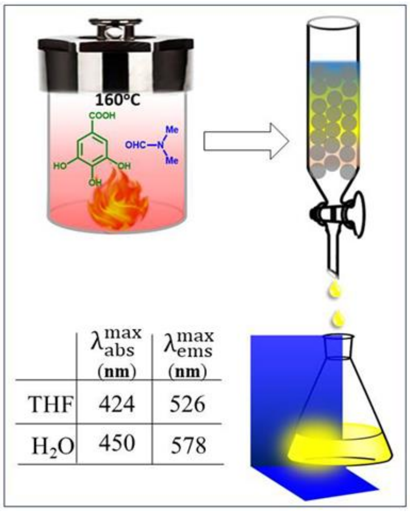

	λ_{abs}^{max} (nm)	λ_{ems}^{max} (nm)
THF	424	526
H_2O	450	578

Scheme-2.1: Schematic representation of the synthesis of yellow emissive product from gallic acid, column chromatography, absorbance, and emission maxima in one non-polar solvent (THF), and polar solvent (H_2O) respectively.

2.3.4. Description of the home-built flow reactor:

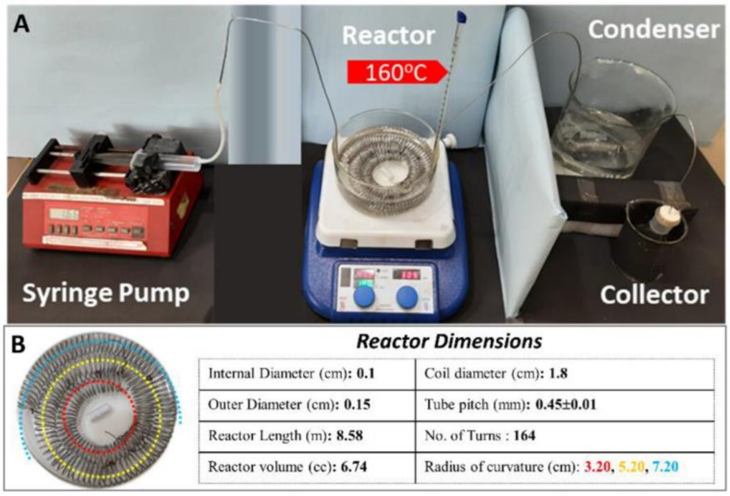

Reactor Dimensions

Internal Diameter (cm): **0.1**	Coil diameter (cm): **1.8**
Outer Diameter (cm): **0.15**	Tube pitch (mm): **0.45±0.01**
Reactor Length (m): **8.58**	No. of Turns : **164**
Reactor volume (cc): **6.74**	Radius of curvature (cm): **3.20**, **5.20**, **7.20**

Figure 2.1: [A] Experimental setup for continuous synthesis of luminescent product. [B] Representee image of coil-in-spiral reactor.

Stainless steel capillary tube 304 has been used for the fabrication of a continuous flow reactor. The inner and outer diameters of the capillary are 0.1 and 0.15 cm, respectively. The total length of the capillary tube is 11.3 m from the inlet to the outlet. The reactor part contains a total number of 164 turns which is covered by 8.58 m of the capillary tube, and the condenser bath contains 23 turns, which is roofed by 1.2 m. The distance between the inlet to the reactor and the condenser to the outlet is the same 45 cm and the in-between distance of the reactor to the condenser is 60 cm.

2.3.5. Continuous method to synthesize yellow emissive product (P^Y) from pyrogallol:

In a typical synthesis, 0.8 g of pyrogallol is dissolved in 20 mL of dry DMF with continuous ultrasonication for 10 min. The transparent solution is then transferred into a syringe and placed in a syringe pump (New Era pump 100). The solution is flowed through the reactor at four different flow rates 0.83 mL/h, 1.66 mL/h, 3.32 mL/h, and

6.64 mL/h. The temperature of the reactor has also been varied from 120 to 180 °C for optimization of reaction conditions. Based on the flow rate of reactant solution and temperature of the reactor, the colour of the resultant solution tends to emerge as dark yellow to dark brown. The colored solution is then mixed with 30 mL of ethyl acetate (EA) and centrifuged for 15 min at 6500 rpm. After that, the supernatant part was filtered out by Whatman filter paper. The filtrate part runs through a column containing silica gel mesh as a stationary phase with a ternary eluted solvent mixture (4:4:2) of DMF, EtOH, and EA. The collected product, P^Y is bright greenish-yellow in colour. It is passed through a 0.2 μM syringe membrane filter before all the spectroscopic and material characterization studies.

2.3.6. Preparation of PVA-PVP Film:

The PVA-PVP film is made using the solvent evaporation process. In summary, 0.2 g of PVA and 0.2 g of PVP were dissolved in 20 ml of Millipore water and stirred for 4 hours on a magnetic stirrer at 70 ºC. The PVA-PVP solution was then chilled to 50 ºC before being separated into two halves, 10ml in each glass beaker. We also made a 5ml stock solution that was dissolved by newly generated 6.25 mg red emissive dry-out product. Now, 1 mL of dye solution was added to one beaker and 0.5 mL to the other. After that, the dye and polymer solution was well mixed and placed into a 4.8 cm diameter (Id) glass petri dish. The solution in the petri dish is dried in a vacuum oven at 50 ºC and 700 mmHg pressure for 48 hours. The dried films were used for the measurement of spectroscopic studies.

2.3.7. Preparation of PVDF Film:

Similar steps were taken to prepare PVDF film. In brief, 20 ml of DMF and 0.2 g of PVDF powder were combined before being sonicated for 20 minutes. A magnetic stirrer was then used to thoroughly mix the solution for an additional hour at 70 ºC. A stock solution containing 2.5 mg of the solid red emissive product and 5 ml of DMF was made in a different set. The 20 ml of translucent polymer solution, which had been chilled to 50 ºC, was divided among four glass Petri dishes of 4.8 cm diameters. To four Petri plates, and individually poured 1 ml, 500 mL, 250 µL, and 125 µL of the stock dye solution and thoroughly mixed them. Using a heated plate at 50 °C for 24 hours, the entire solution dries out. The dried films were utilized for spectroscopic measurements.

2.3.8. Isolation of Chloroplast and determination of concentration of chlorophyll:

Fresh spinach leaves have been used to obtain chloroplast. Inbrief, 30 g cleaned spinach leaves were chopped and then grounded within sucrose buffer (30 ml, pH= 7.3) containing 0.4 M sucrose, 0.01 M KCl, 0.03 M Na_2HPO_4 and 0.02 M KH_2PO_4. Then the mixture was filtered through Whatman no. 1 filter paper and the obtained filtrate was centrifuged at 2000 rpm for 5 minutes. After that, I have made a suspension of chloroplast by dispersing the centrifugal precipitate in sucrose buffer. To determine chlorophyll concentration, 250 µL chloroplast suspension was vortexed in a polypropylene tube with 2.25 ml distilled water and 10 ml pure acetone. The suspension was filtered with Whatman No. 1 filter paper and absorbance value at 652 nm was recorded. The chlorophyll concentration (mg chlorophyll/ml chloroplast suspension) was quantified using the below equation

$$C= (\text{Abs.}652\ \text{nm} \times \text{Dilution factor}) / 34.5$$

The estimated chlorophyll concentration was found to be 19 μg chlorophyll/ml chloroplast suspension.

2.3.9. Cell Culture:

Human colon carcinoma cell line (HT-29), was purchased from the National centre for cell science (NCCS), Pune. HT-29 cells were maintained in DMEM medium (Gibco) supplemented with 10% fatal bovine serum (Himedia, India), 1% penicillin and streptomycin and 1% of Glutmax (Gibco, Thermo Scientific, USA) at 37 °C in 5% CO2. The cells were trypsinized upon reaching 70–80% confluency using 0.25% trypsin-EDTA (Thermo Fisher Scientific, USA).

2.3.10. Protocol for Intracellular Co-localization study:

Briefly, 0.5X106 cells were cultured in a 60 mm dish, after reaching to their suitable confluency the cells were subjected to treatment with different products in 37oC with 5% CO2 for 48 hours. After the incubation, the cells were washed with PBS once followed by staining with 1μM Hoechst 33342 (Sigma cat. # B2261). After 30 min of incubation in the Hoechst staining solution, the staining media was discarded and the cells were replenished with fresh complete media at 37°C. Fluorescent product’s co-localization study was performed using EVOS 5000 imager (Invitrogen, Thermo fisher)

Chapter 3

Connecting the Dots of Carbon Nanodot—Molecular Assembly

Substantial Research on photoluminescent carbon dots has created opportunities in energy & biomedical areas where there exists a gap in fundamental understanding on its structure and more so on the role of graphitic-N in tuning their emission properties. Among the proposed hypothesis on the origin of their emission properties, emerging one that suggests the formation of molecular crystals lacks foundations of molecular transformability. In this article, solvent reactiveness has been found to manipulate the emission properties of the products derived from the one-pot solvothermal reaction. Excellent superimposition of absorption and excitation spectra and excitation-energy-independent emission of green and red emissive products are suggestive of their molecular natures. Best-known graphitic-N in carbon nanodot turns out to be the nitrogen of citrazinic acid. Synthesized emitters exhibit reverse solvatochromism, surfactant-induced aggregation, and electrostatic-sequestration at micellar surface. An unprecedented solvent-directed green switching of the red-emissive product (P^{R}) has been presented here and the transformed product ($P^{R\rightarrow G*}$) shows an uncanny resemblance of spectroscopic properties with the green-emissive product (P^{G}). The products can easily bind to bovine serum albumin and retain their emissive properties in the bound state as signaled by the augmentation of fluorescence properties. A hybrid photosynthetic system, the chloroplast-red emissive product is found to exhibit a markedly higher rate of reduction of ferricyanide than that of chloroplast alone.

3.1. Introduction:

Serendipitous observation of excitation energy-dependent photoluminescence from nanoscale carbon particles in 2004 has rejuvenated the search for solution-processed, biocompatible, and photoluminescent carbon quantum dots.[144] There are a vast number of reports on strategies for the synthesis of such water-soluble, photoluminescent dots, usually termed carbon nanodots (CNDs).[33,145–147] Their potential applications cover the most demanding [8] areas of research in recent times such as intracellular co-localization, light-emitting-diodes, hydrogen gas production, and enhanced photosynthesis.[12,21,123,148–150] The photoluminescence of the reported CNDs is highly sensitive to precursors and solvents used in the synthetic method. And emissions of these CNDs can easily be tuned by the doping of nitrogen, sulfur, and others, yielding a color gamut.[71,119,151,152]

The impetus generated by the carbon nanodot for violating the photochemical principle- Kasha-Vavilov's rule fails to gather steam due to the unavailability and uncertainty in the structural features of carbon nanodot and the mechanism of elemental doping.[153–155] The emergence of excitation energy-independent photoluminescence in this context challenges the foundation of the best-known carbon nanodot.[15,123,156] Recently, it has been shown that aggregates of citrazinic acid alone, at room temperature can exhibit excitation energy-dependent emission and graphitic nanocarbon features.[29] Hence, the term nano in CNDs can be restricted to only solid-state structural aspects, rather than emission characteristics in solution. It's worthy to mention here that the science-based concerns on the origin of their photoluminescence have not been settled yet. A prominent hypothesis on the involvement of graphitic carbon in dictating its emission properties is one-dimensional and devoid of basic principles of organic transformations.[9,24,157,158] Whereas the emerging hypothesis of molecular crystals in solid-state is more insightful, however, it needs to be substantiated with experimental evidence of direct molecular transformability.[25,123,159–162] This has highly intrigued us to identify the routes of molecular transformability for carbon nanodots. To the best of our understanding, this is the first report where such a challenging yet compelling attempt of switching red emissive carbon dot to green emissive one has been made.

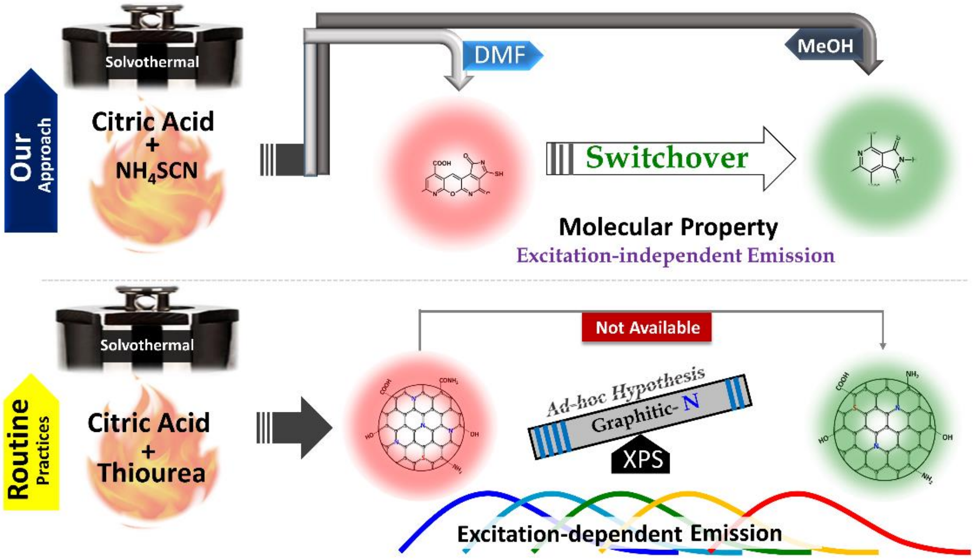

Scheme 3. 1 : Schematic representation of the solvent-directed synthesis of red and green emissive products with the same starting precursors (top). Routine practices and ad-hoc hypothesis of carbon nanodot research (bottom).`

Among the precursors used for the synthesis of carbon nanodot, citric acid along with either amines or thiourea are prevalent ones.[21,163,164] It has, thus, chosen citric acid and ammonium isothiocyanate as precursors for our study. Other than physical parameters such as temperature, pressure, and reaction time, the reactivity of solvents in dictating the photoluminescence property of the product is also resurfacing. Therefore, an advocated concept of solvent engineering is nothing but the formation of different products due to the difference in reactivity and polarity among solvents.[152,165,166] It has been carried out solvothermal reactions of identified precursors in two different solvents- dimethylformamide, a reactive solvent, and methanol, a relatively inert solvent. DMF has a unique ability to take part in reactions by serving as an electrophile or a nucleophile. Moreover, it can provide building blocks of different types, such as CHO, CO, and others.[123,167]

Previously, it has been shown that citric acid with other appropriate precursors under solvothermal conditions yields carbon dots with multiple emission peaks covering the entire visible range- red, green, and blue. However, the molecular origin of citric acid-derived green and red emissive carbon dots remains a challenging task to date due to poor photostability and the inherent difficulty in tracing the product formation pathway.

In, this work, it has been addressed the stability issue and then developed an effective separation method for the isolation of red and green emissive products. One of the objectives of our work is to identify the molecular origins of synthesized products. To achieve this ambitious target, experimental results have been juxtaposed with computational predictions in understanding photophysical properties in neat solvents. Moreover, it has been performed interaction of synthesized products in aqueous micellar media to decipher the surface charge of products through electrostatic sequestration.[168,169] It is anticipated that products will reside in the stern layer of ionic surfactants based on the overall charge by signalling augmented emission properties.[170,171] Solvent-directed switchability of red-emissive product to green-emissive one further corroborates the molecular origin of synthesized products under solvothermal conditions. With such enriching fundamental insights, potential applications of red emissive product have been explored in enhanced photosynthesis.[149,172,173] It should be mentioned here that the protein labelling market is globally a billion-dollar market and demand for low-cost fluorescent markers is at an all-time high. It also report here that the green and red emissive products have commercial significance for potential fluorescent markers of proteins. However, assessing the need for the electrostatic, hydrophobic, and protein-tagging ability for the design of an efficient light-harvesting system, the red emissive product is thus selected for the study. A hybrid photosynthetic system, Chloroplast-red emissive product is developed that can effectively reduce the electron-accepting agent in Hill reactions.

3.2. Results & Discussion:

3.2.1. Product Manipulation by Solvent Reactivity:

Based on their chemical natures, solvents are generally classified into two categories- inert and reactive. The use of reactive solvents for a condensation reaction is frequently practiced in product synthesis. Solvent engineering is perhaps coined due to the untraceability of solvent's role in product formation in a one-pot synthetic condition. Thus, deciphering the role of solvents and corresponding products is the subject of investigation here. DMF and methanol are chosen as solvents owing to their significant difference in physical and chemical properties. Unprecedentedly the DMF yields a red emissive product (P^R) whereas methanol offers a different product- i.e., green emissive (P^G) from the same set of precursors- citric acid, ammonium thiocyanate, and borax under a similar reaction condition as well (Fig.3 1A). It has been developed a separation method of products and its purity is being tested by thin-layer chromatography and superimposing the absorption and excitation spectra of products (Fig 3.1B). A perfect superimposition signals the presence of only one emitting species that is absorbing in the visible spectral range of light. The absorption spectrum of the red-emissive product is relatively broader than that of the green-emissive product.

The steady-state emission spectra of the products in methanol are recorded at different excitation wavelengths for the identification of the excitation energy-dependent dynamics (Fig.3 1B). Surprisingly, both the products, P^R and P^G show excitation energy–independent behavior adhering to the Kasha-Vavilov rule.[174] The emission band maxima of the product, P^R is centered at 630 nm and that of P^G is at 510 nm. The Stoke's shift observed for product, P^R is 65 nm, whereas for P^R is 100 nm. Such as a large Stoke's shift is primarily observed for organic fluorophores.

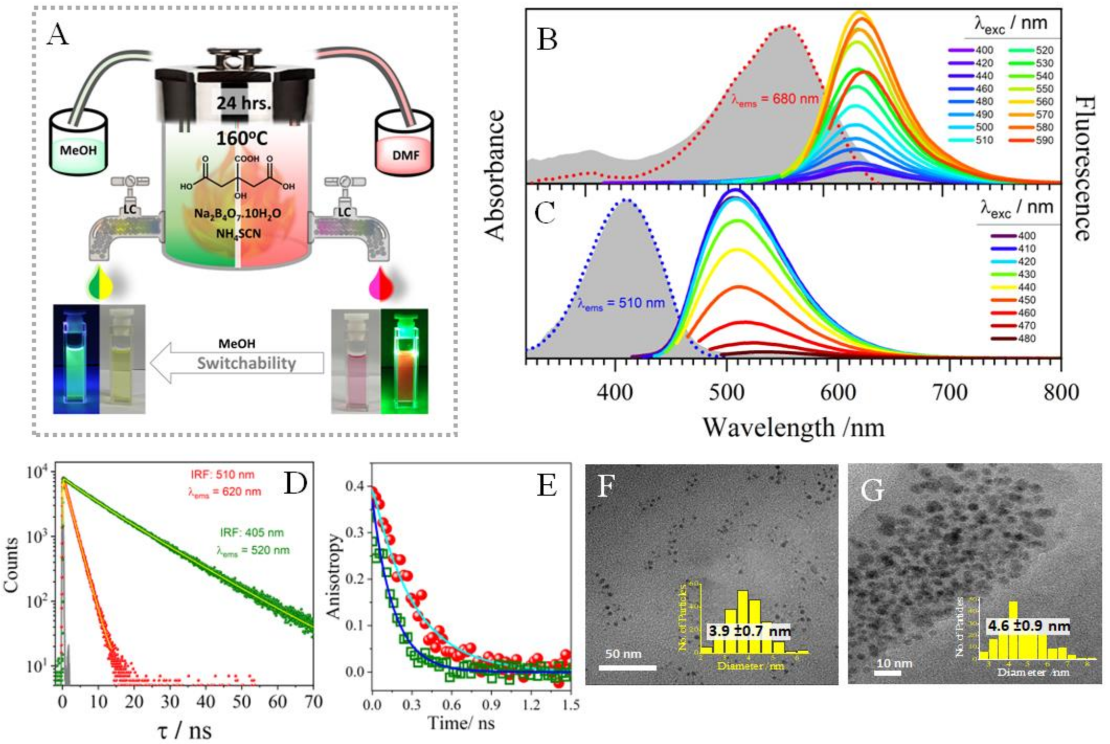

Figure 3. 1. [A] Solvothermal method employed with two different solvents- MeOH and DMF for the synthesis of fluorescent products. The products separated using a chromatographic method are placed in an ambient atmosphere and under irradiation at 530 nm (for P^R) and 405 nm (for P^G). **[B-C]** Absorption spectrum (shaded region) overlayed with excitation spectrum (dotted line) and steady-state emission spectra at different excitation wavelengths of- product, P^R (B), and P^G (C). **[D]** Time-resolved emission of products in methanol – P^R at 620 nm, P^G at 520 nm. Fitted line in yellow color. Solid grey line shows the Instrument Response function. **[E]** Time-dependent fluorescence anisotropy of products – P^R at 620 nm (red solid circles), P^G (hollow green squares) at 520 nm. Fitted lines are represented accordingly. TEM image of products- P^R **[F]** and P^G **[G]**; Inset - particle size distribution.

The quantum yield of red-emissive product, P^R in methanol at 540 nm is 0.14, and that of green emissive product, P^G at 420 nm is 0.40. It is generally perceived that an increase in quantum yield is associated with the structural rigidity and compact size of the product. Thus measured the time-resolved emission properties of synthesized products. The photoluminescence decay of the reported carbon dot is multi-exponential, but its origin remains an enigma. It has been found that fluorescence decay of red-emissive product, P^R in methanol is single-exponential with a lifetime of 2 ns (Fig.

3.1C) whereas that of product, P^G is biexponential with an average lifetime of 12.6 ns (Table 3.1).

Products	λ_{exc}/ nm	λ_{ems}/nm	τ_1/ns	τ_2/ns	a_1	a_2	$<\tau>$/ns	χ^2
P^R	510	620	2.03	-	1.00	-	2.03	1.19
P^G	405	520	6.80	13.7	0.26	0.74	12.64	1.05

Table 3.1: The average fluorescence lifetime of red emissive (P^R) and green emissive (P^G) products in MeOH solvent.

This observation provides a likely explanation for the commonly reported trend of faster-excited state depopulation of carbon dots at longer emission wavelengths and is consistent with the prediction of molecular heterogeneity of carbon dots at a single-particle level.[175,176] The fluorescence anisotropy that contemplates the compactness vis-à-vis structural rigidity of fluorophore originates from its transition moment of absorption and emission along with specific directions. Steady-state anisotropy (r_{ss}) of CNDs has exhibited an increasing trend with emission wavelength and ranges from 0.15 to 0.34 in glycerol media.[114,154] As it is known that the fluorescence anisotropy displays monotonous dependence on solvent viscosity. Moreover, polarity, proticity and chemical nature of solvents are also found to regulate the fluorescence anisotropy of emitting species. Thus, to neutralize this solvents dependence in understanding of structural features (size, and flexibility) of emitting probes, and measured the rotational rate, r(t) of products in methanol that has a viscosity of 0.554 mPa s. The time-dependent anisotropy of red emissive product P^R shows a relatively slower decay with 310 ps correlation time, whereas the correlation time of 160 ps for the green-emissive product, P^G (Figure 3.1E). It's worth mentioning that a typical correlation time associated with anisotropy decay would generally range in the picosecond (ps) for molecular fluorophores, whereas that for proteins and polymers in the nanosecond (ns) range.[174] Thus, it can be predicted that the red emissive product is relatively larger in molecular size than the green emissive product.

Next, untangling the role of H-bonding in the formation of molecular crystals in the solid state of products demands high-resolution imaging by employing transmission electron microscopy (TEM), because organic fluorophores are generally known to form amorphous aggregates but the molecules with multiple hydroxyl, acid groups tend to form crystalline aggregates.[177–179] TEM images clearly show the typical particle formation for both the products and the average diameters of the particles deposited are measured to be 3.9 ± 0.7 nm for red-emissive product and 4.6 ± 0.9 nm for product, P^G (Fig. 3.1F-G, Inset). To our expectation, two-dimensional nanosheets with lattice fringes are found in high-resolution TEM images and such nano-feature is even found beyond dark spots, i.e., amorphous aggregate (Figure A3.1). The observed lattice spacing is measured to be 0.21 nm for product, P^R and 0.26 nm for product, P^G (Figure A3.2, Inset) Thus, it can assert here that the functional groups (hydroxyl, carboxyl groups, amine & others) of product molecules are the reason for the observation of molecular crystalline aggregates in solid-state.

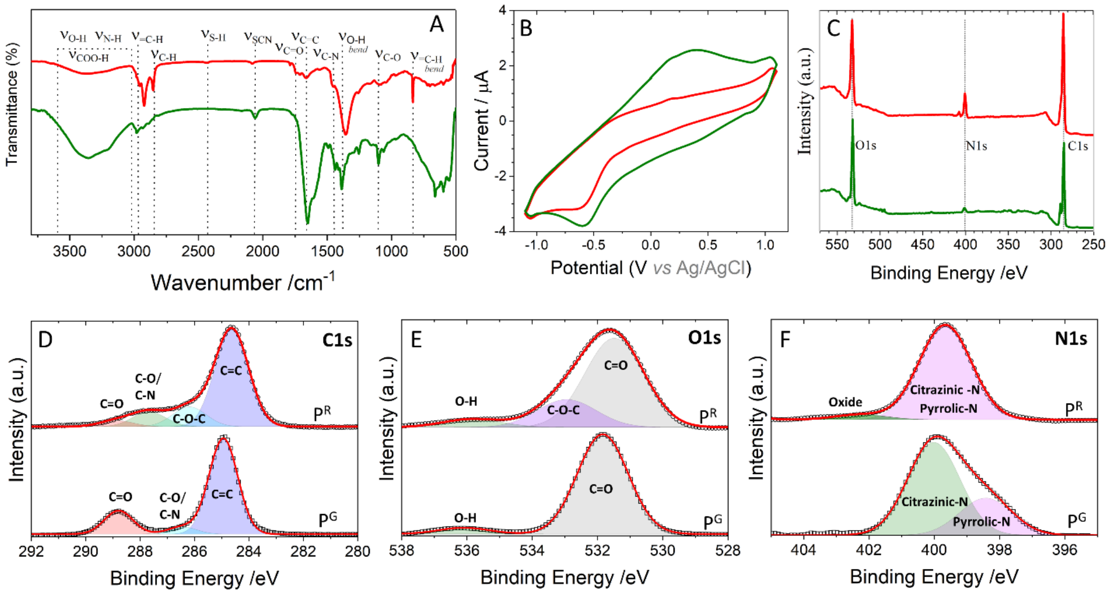

Figure 3.2. [A] FT-IR spectra, **[B]** Cyclic voltammetry, and **[C]** Full survey XPS spectra of red-emissive product, P^R (red line) and green-emissive product, P^G (green-line). High-resolution XPS of- **[D]** the C 1s core level, **[E]** the O 1s core level, and **[F]** N 1s core level of product, P^R (top panel) and P^G (bottom panel). Fitted lines are in solid red color, experimental data is in hollow circles, and individual components are presented in colored areas for clarity.

Thus, FT-IR spectroscopy is first employed for the identification of functional groups present in the synthesized products (Fig. 3.2A). Both the products exhibit a nearly equal number of vibrations, except, a visible difference for bands that appear at 2000 cm^{-1} and 2500 cm^{-1}. The stretching vibrations of C–H, N–H, O–H, and COO–H contribute to the broad IR band, 3700 to 2700 cm^{-1}. The stretching vibration at 2058 cm^{-1} is marked to C-S bonding.[180] Interestingly, a characteristic peak of the thiol group (S-H) has appeared for red-emissive product at 2430 cm^{-1}.[181] The strong FTIR bands at 1740 cm^{-1}, 1660 cm^{-1} belong to C=O, and C=C vibrations respectively. Peaks at 1380 cm^{-1} and 1100 cm^{-1} can be assigned to C–N and C–O bonding .[182]

Further, identification of the nature of hydroxyl groups has been done by recording cyclic voltammograms of synthesized products in 0.1 M KCl at a scan rate of 0.03 V/s

(Fig.3.2B). Cathodic signals are observed at - 0.59 V (vs. Ag/AgCl) for both products, whereas the anodic signals appear at 0.19 V and 0.38 V (vs. Ag/AgCl) for product P^R and P^G respectively. The formal potential of the redox couple was determined as the average of the reversible oxidation peak potential (1.27 versus Ag/AgCl) and the reversible reduction peak potential (−0.5 V versus Ag/AgCl). These peak potentials are most likely attributed to the reduction and oxidation of phenolic OH groups.[183] The red emissive product fails to display characteristic duck-shaped voltammograms indicating quasi-irreversibility, moreover, it is prone to get easily oxidized under oxidative stress due to low oxidation potential.

To counter an adhoc hypothesis of graphitic-N for tuning the emission characteristics of carbon dot and further deepen our understanding on elemental composition and their chemical state in synthesized products it has been performed X-ray photoelectron spectroscopy (XPS). A full scan of the XPS spectrum for each emissive product shows distinct peaks corresponding to O 1s (532.1 eV), N 1s (400.1 eV), and C 1s (285.1 eV), respectively (Fig.3.2C). The high-resolution scan of the C 1s region of red-emissive product shows carbon present in 4 different chemical environments C=C at 284.65 eV, C–O–C at 286.20 C-N, and C–O at 287.70 eV, and C=O at 288.50 eV (Table A3.1). However, a peak corresponding to C-O-C disappears for green-emissive product (Fig. 3.2D). This observation has been corroborated with O 1s spectra of products (Fig. 3.2E). Peaks appeared at 531.50, 533.00, and 535.82 eV in the O 1s spectrum can be assigned to C=O, C–O–C, and O–H components respectively.[184] One of the most contentious subjects in nanodot research is the assignment of the chemical nature of nitrogens present in the synthesized product. To draw a difference between often termed pyridinic-N with citrazinic-N, N 1s peak of commercially available citrazinic acid has been taken as a reference point. citrazinic acid, which is centered at 400.90 eV.

Interestingly, the XPS data of N 1s of synthesized products show the presence of predominantly two types of nitrogens- citrazinic-N (400.10 eV) and pyrrolic-N (398.40 eV). Expectedly, citrazinic-N is populated over pyrrole-N for red emissive product. Accounting of all the characterization results including mass spectrometric and 1H-NMR data of products (Figure A3.3-A3.6) It has been suggest here the involvement of a common reaction pathway in solvothermal conditions, the first step is the formation of citrazinic acid derivative from the reaction of citric acid and ammonium thiocyanate and followed by nucleophilic substitution of thiocyanate. Intramolecular amidation has resulted in formation of pyrrole-citrazinic chromophoric unit, green emissive product (Scheme3.2).

$$NH_4SCN \longrightarrow NH_4^+ + SCN^- \rightleftharpoons NH_3 + HSCN$$

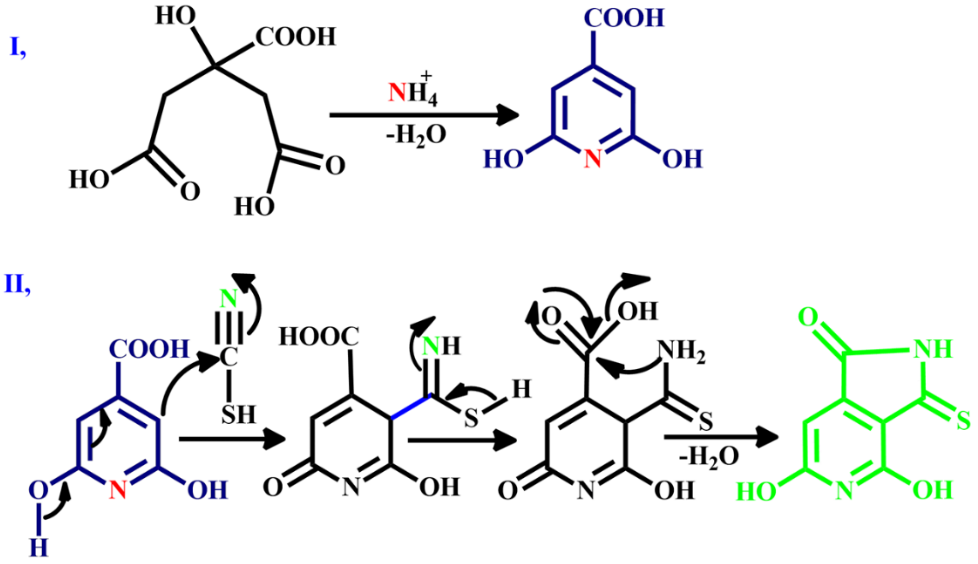

Scheme 3.2: Proposed reaction mechanism of the synthesized green emissive product, (P^G)

Dimethyl-formamide is serving as a formylating agent here, which is quite like the Vilsmeier-Haack reaction for formylation of aromatic rings. Condensation of citrazinic-pyrrole chromophoric unit with another citrazinic acid has yielded red-emissive fluorescent product, pyrrolo-pyrano-dicitrazinic unit (Scheme-3.3).

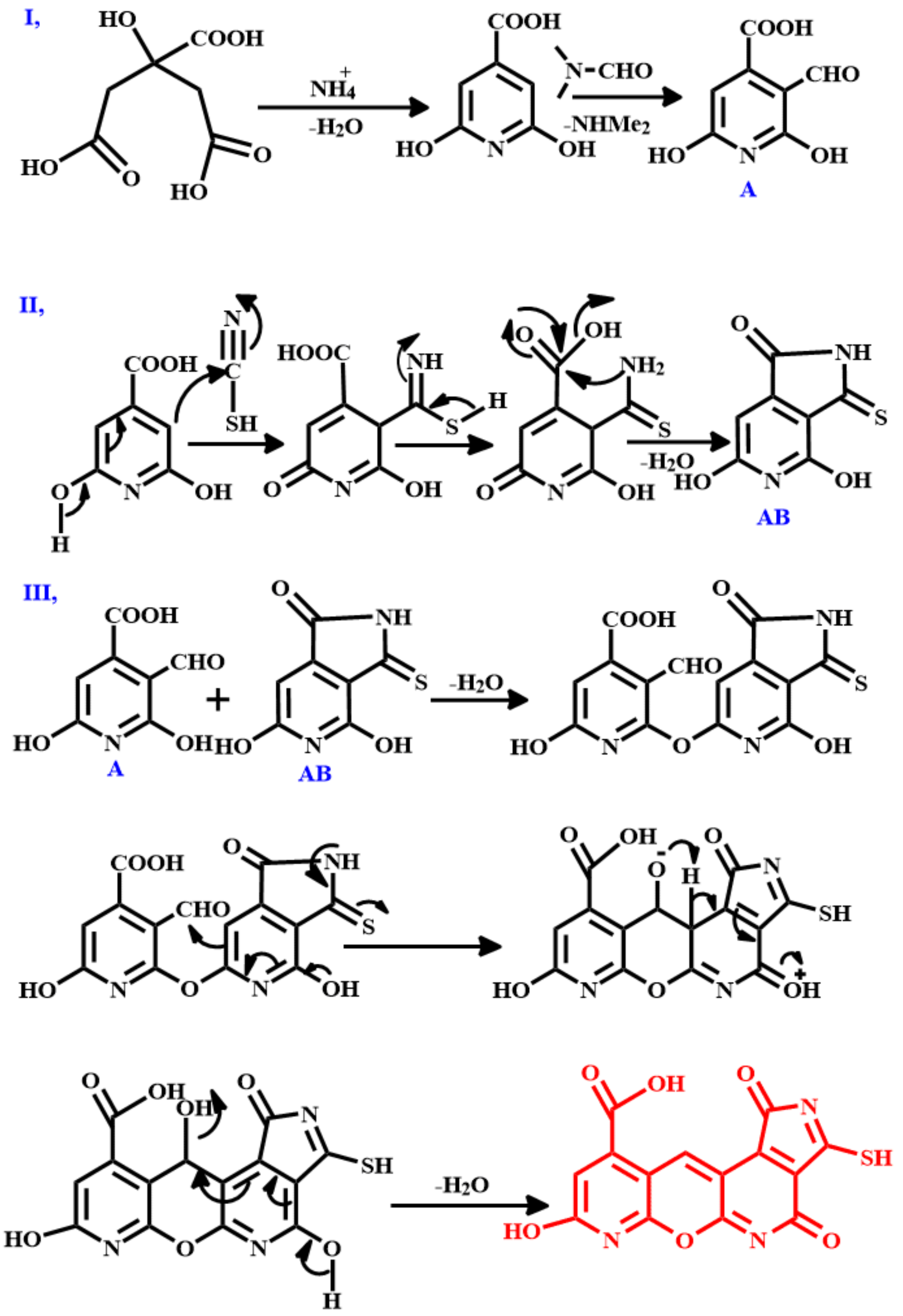

Scheme 3.3: Proposed reaction mechanism of the synthesized red emissive product, (P^R)

To validate the proposed molecular fluorophores, It has been optimized the molecular geometries of the products, using Density Functional Theory.[185] The Cartesian coordinates of the atoms in the products and computed stretching frequencies which are found in good agreement with the experimental values are presented. On the other hand, vertical excitations in the lowest energy region of proposed fluorophores have been calculated at a semiempirical, ZINDO and classical, time-dependent density functional theory (TD-DFT) level for the fluorophores are also in fairly good agreement with their respective experimental data (Table A3.2). Specifically, computed vertical excitation of green emissive product is 396.82 nm and the absorption peak maximum of that product in methanol is 411 nm. However, a slight deviation in band maxima of red emissive product might be due to the omission of specific interactions such as solvation, solute-solvent interactions, H-bonding.[28,186,187]

To probe the existence of such solvent-specific interactions, it has been studied solvatochromism of synthesized products. Emission maxima of red emissive product get significantly redshifted with solvent polarity. However, a clear bunching of the emission maxima of emissive products occurs for the solvents. A radar plot has thus been constructed for important photophysical properties of products against a micropolarity parameter, E_T (30) of solvents (Fig. 3.3C-D). As it can be evident that considerable Stokes' shifts for products are observed in all the solvents. However, it tends to obey the classic energy gap law that has been reflected for products in water-an increased Stokes' shifts with a concomitant decrease of fluorescence quantum yield. The fluorescence decays of the green-emissive product remain more-or-less independent of solvent polarity index, except water, whereas that of red-emissive product gradually decreases with micropolarity parameter solvent polarity (Figure A3.7). Such distinction in solvatochromism of products can also be bolstered from the computational results as the computed dipole moment of red emissive product is relatively high than that of green-emissive product.

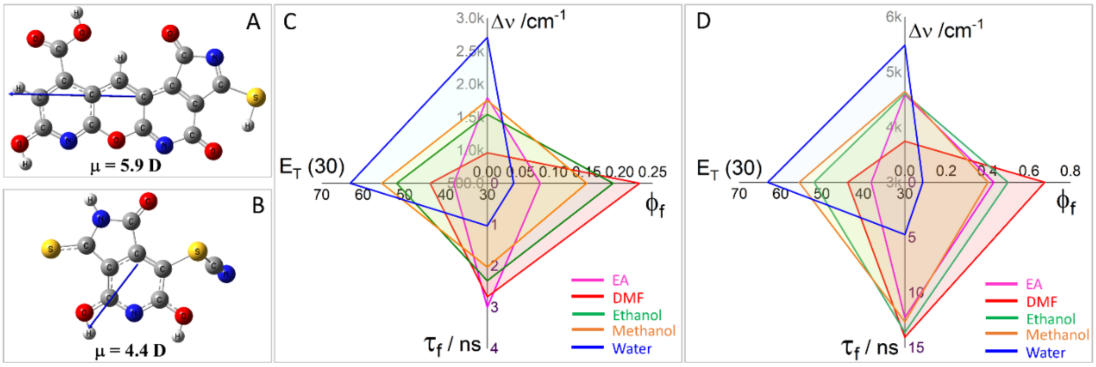

Figure 3.3. Optimized molecular structure of- **[A]** red emissive product, P^R and **[B]** green emissive product, P^G. The orientations of dipole moments are shown. The variation of the Stokes's Shift (Δν), quantum yield (ϕ_f) and (τ_f) of products with the empirical micropolarity, E_T (30) - **[C]** red emissive product, P^R and **[D]** green emissive product, P^G. The solvents used are Ethyl acetate (EA), Dimethyl formamide (DMF), ethanol, methanol, and water.

In an aqueous medium, average fluorescence lifetimes of emissive species get significantly decreased, which might be due to the opening up of another nonradiative process.[186,188] More importantly, products show considerably lower Stokes' shift, higher quantum yield, and fluorescence lifetime in dimethyl formamide. It suggests a more specific solute-solvent interaction, often termed as reverse solvatochromism that originates from the H-bonding mediated intermolecular charge transfer (ICT) operating at the microscopic level.

3.2.2. Electrostatic Sequestration by Cationic Surfactant:

The surface charge of carbon dots in aqueous solution has been poorly understood and thus ionic surfactants are chosen to drive the electrostatic interaction. The absorption spectrum of product, P^R has vibronic nature with peaks at 525 nm and 560 nm respectively, which supports further the molecular nature of product. However, the absorption at 560 nm gets intensified gradually on addition of CTAB till a concentration of 2 mM, after which the absorption spectrum remains unaltered. The emission spectra of red and green emissive products in aqueous medium (pH 6.5) in the presence and absence of CTAB are presented in (Fig.3.4A-B) respectively. Upon addition of 0.5 mM CTAB, the emission intensity of red emissive product gets quenched indicating surfactant-induced formation of fluorophore-surfactant aggregates, as generally observed for organic molecules in earlier reports.[174,189] Moreover, further addition of CTAB has resulted in a gradual increase in the emission intensities of products. Notably, the emission peak maxima of both the products get blue-shifted by nearly 10 nm, which means sequestration of fluorophores from bulk water.

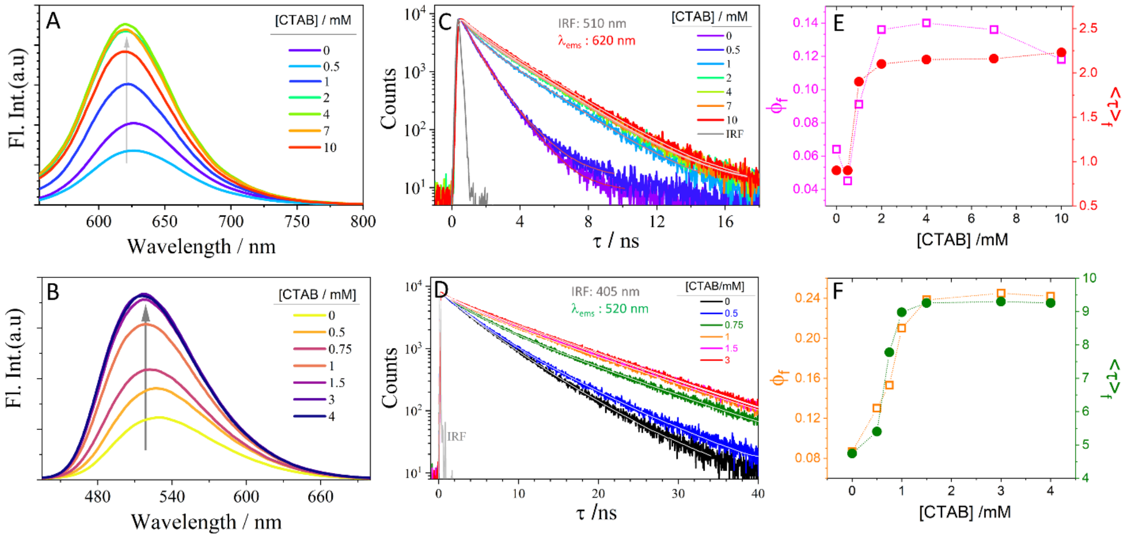

Figure 3.4. Emission spectra and Fluorescence decays of products in aqueous solutions at different concentration of CTAB- **[A, C]** red emissive product, P^R and **[B, D]** green emissive product, P^G respectively. Variation of fluorescence quantum yield and average emission lifetime of- **[E]** product, P^R and **[F]** product, P^G. Quantum yield and average emission lifetime are represented as hollow square and filled circle.

The time-resolved fluorescence studies of products in surfactant solutions are also performed to highlight the signature of dynamic quenching over simple static one (Figure 3.4C-D). Surfactant-caused aggregation at 0.5 mM CTAB is found to be a ground state phenomenon for product, P^R. The average lifetime of product, P^R in aqueous medium is estimated to be 0.98 ns (Table A3.3). Analysis of decay traces of red emissive product, P^R reveals the presence of two components in aqueous solution: a very short one with a lifetime (τ_1) of 0.54 ns (0.54), and long component (τ_2) of 1.10 ns (0.46). Upon addition of CTAB, the short-component (τ_1) has merely increased to 0.77 ns but with a decreased amplitude of 0.33, whereas the longer component (τ_2) has augmented to 2.37 ns with amplitude of 0.67. At 4 mM CTAB the average lifetime of product, P^R increased by nearly 1.2 ns from that of bulk water. Thus, it can be mentioned here that the red emissive product experiences micropolarity in CTAB close to the neat solvent, methanol. On the other hand, the fluorescence decay of product, P^G in aqueous medium is biexponential with average lifetime of 4.74 ns (Table A3.4). Deconvolution of decay traces of product, P^G shows a component with a lifetime (τ_1) of 2.85 ns (0.49), and longer component (τ_2) of 5.66 ns (0.51). Upon addition of CTAB, the τ_1 gradually decreases to 2.04 ns with amplitude of 0.20 only whereas the τ_2 has significantly increased to 9.64 ns with amplitude of 0.80. The average lifetime of product, P^R in 4 mM CTAB has jumped to 9.26 ns.

The observation of inflection point near the critical micellar concentration (CMC) of CTAB further confirms the molecular nature of the emitter. Emitter with larger in size and shape (such as nanoparticle) is expected to shift the inflection point at much higher concentrations of the surfactant. Variation of quantum yield and average emission lifetime of products with increased concentration of CTAB has been plotted and has been found to follow a trend of saturation. The reason for increased quantum yields along with blue-shift of peak maxima of products is generally attributed to the existence of aggregates of the fluorophore in water and their disruption upon micellization, because aggregates are generally nonfluorescent and the micellized monomers are highly fluorescent. However, studies carried out in an anionic surfactant, SDS rule out the hypothesis of micellization, as no considerable change in emission intensities is noticed. The augmentation of emission intensity can thus be attributed to the existence of electrostatic interaction between fluorophore and micellar surface. The emitting species are residing in the vicinity of stern layer of CTAB and thus experience a relatively hydrophobic environment in comparison to bulk water.[168,190,191] The steady state absorption and emission spectra of red emissive product measured at varied pH of the aqueous medium rule out typical shifting of acid-base equilibrium at the micellar surface.

3.2.3. Switchability of Red-Emissive Product (P^R):

The reported hypothesis on the presence of graphitic carbon core and involvement of surface states responsible for the emission of carbon dot is highly restrictive and thus transformability of carbon dot and thereafter its analysis challenges the foundation. Our research group has dissected the molecular fluorescence and nanocarbon by advocating the formation of H-bonded molecular crystals under solid state. To push the hypothesis further, the transformability of emitters has been tested for the very first time by applying a proven concept of retrosynthesis- solvent-directed molecular transformability. Noticing its pivotal role in yielding green-emissive product methanol-directed transformability of red-emissive product under solvothermal condition has been attempted. However, it has been commonly observed that organic fluorophores exhibit solvent-polarity driven aggregation. Surprisingly, red-emissive product, P^R gets switched to green emissive species ($P^{R\rightarrow G*}$) upon methanol treatment. To understand its molecular origin, it has been directly compared the steady-state emission properties of the switched product, $P^{R\rightarrow G*}$ with green emissive product, P^G (Table A3.5). The contour plot of emission spectra over excitation energies of switched product ($P^{R\rightarrow G*}$) shows an uncanny resemblance with that of product, P^G (Fig. 3.5A-B).

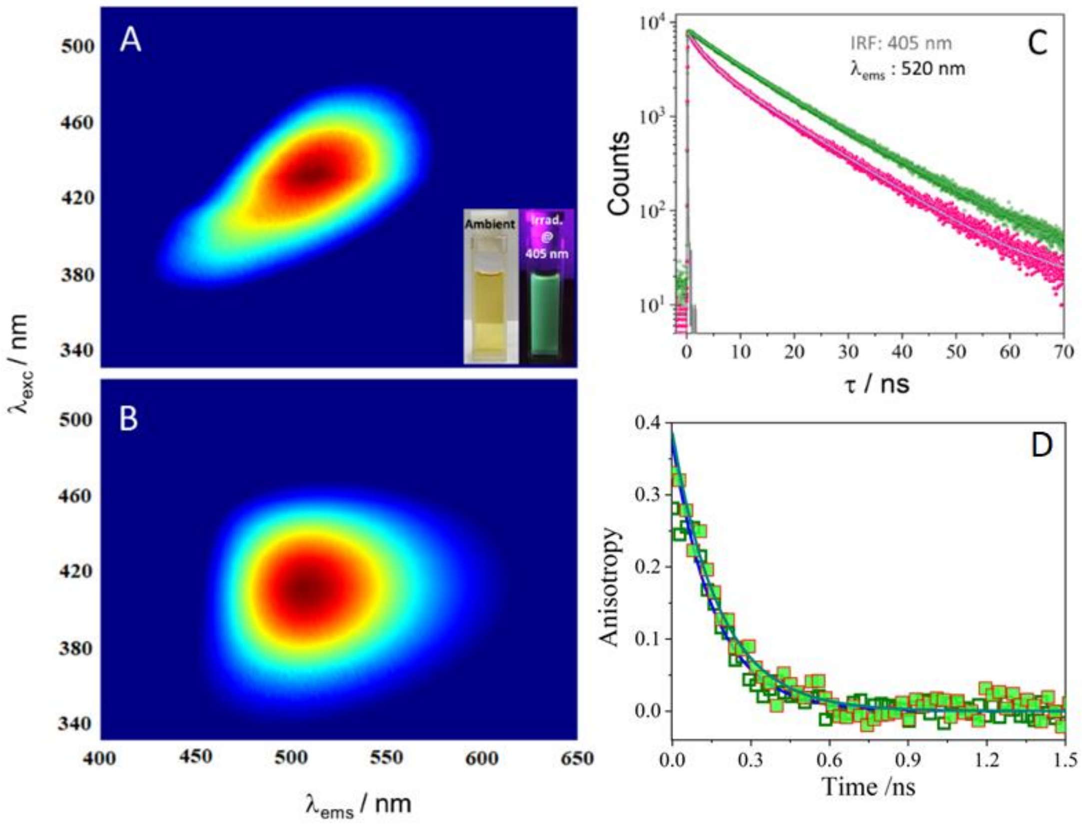

Figure 3.5. Contour plot of emission spectrum with corresponding excitation wavelengths- [**A**] switched green product, $P^{R\rightarrow G*}$ and **[B]** green emissive product, P^{G}. [C] Fluorescence decay of products, $P^{R\rightarrow G*}$ (pink dots) and P^{G} (green dots). Fitted lines are shown accordingly. [D] Time-dependent fluorescence anisotropy of products, $P^{R\rightarrow G*}$ (filled green square) and P^{G} (hollow square)

Moreover, respective fluorescence excitation spectrum of transformed product shows a greater degree of similarity with that of green emissive product. The average lifetime of product, $P^{R\rightarrow G*}$ is 10.9 ns in methanol whereas that of product, P^{G} is 12.64 ns (Fig. 3.5C, Tab.A3.5). Time-resolved fluorescence decay of product, $P^{R\rightarrow G*}$ show presence of three components- 0.92 (0.24), 4.55 ns (0.36) and 12.92 ns (0.40). The origin of a very short component can be attributed to the presence of any small, degraded product that evades silica-gel chromatographic methods and thus serves as a quencher of emission of switched product, $P^{R\rightarrow G*}$. To substantiate this claim, I performed time-dependent fluorescence anisotropy of transformed product (Fig 3.5D).

The switched product, $P^{R\rightarrow G*}$shows a time-dependent anisotropy of decay with 180 ps correlation time, whereas for green -emissive product, P^{G}, the correlation time is 160 ps. This close match of correlation time not only suggests structural similarities between green emitters but also points out that green emitter is the building block of the red-emissive product (Scheme-S3.4). The switched product is also highly photostable in nature.

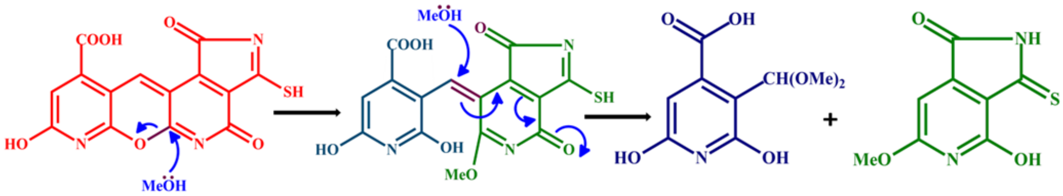

Scheme 3.4: Proposed reaction mechanism of the synthesize, $P^{R\rightarrow G*}$ product.

3.2.4. Fast Kinetics of Hill Reaction- Enhancing the Photosynthesis:

Chloroplast of plants are known to perform photosynthesis by absorbing Sunlight. However, chlorophylls present in Chloroplast uses a limited range of the solar radiation spectrum for this purpose. Thus, design of a hybrid photosynthetic system for better coverage and utilization of spectral range of solar radiation remains a thrust area of energy research.[192] Fluorescent molecules having biocompatibility and photocatalytic activity become the obvious choice for development of a hybrid photosynthetic system.[193,194] However, compatibility between fluorescent probe and chloroplast is governed by the strong electrostatic and hydrophobic interaction. Thus, red emissive product (P^{R}) has been chosen for – (i) better coverage of solar radiation spectrum, (ii) more electrostatic interaction with a surfactant, CTAB, and (iii) can easily bind with proteins and retain simple biophysical properties. In the Hill Reaction of

Photosynthesis, isolated chloroplasts can release oxygen by water splitting under a light source in the presence of an electron acceptor, Ferricyanide. Thus, in our investigation of the photocatalytic activity of the hybrid system, Chloroplast- red emissive product, P^R, a model redox reaction- ferricyanide to ferrocyanide has been chosen. The objective is to quantify the photocatalytic performance of our hybrid system over isolated Chloroplast by measuring the rate of reduction of ferricyanide. The chloroplast isolated from spinach was incubated with red emissive product and separated from unbound fluorophores. The absorption and emission spectra of the hybrid system are different from that of chloroplast alone (Figure 3.6A-B). The modified chloroplast absorbs more light in the visible spectra range from 450 nm – 650 nm without altering its native spectral features such as the soret band. Slight drop in emission intensity of probe in hybrid system is suggestive of difference in microenvironment between aqueous medium and chloroplast. Based on this evidence, and then measured the photosynthetic activity of the hybrid system by monitoring the absorbance of ferricyanide at 420 nm.

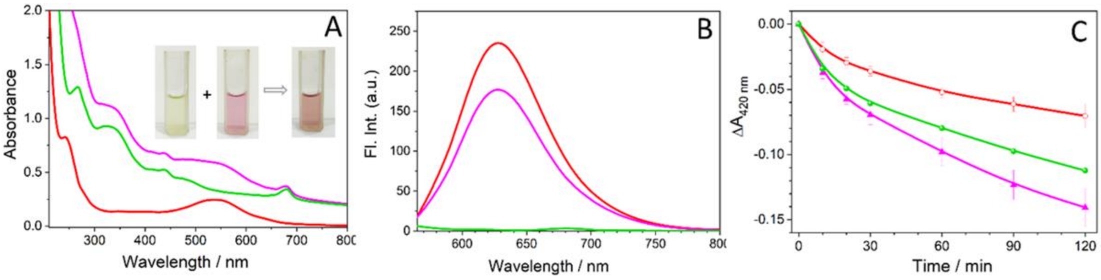

Figure 3.6. [A] Absorption spectra of red emissive product *(red line)*, isolated chloroplast *(green line)* and hybrid photosynthetic system i.e., chloroplast-red emissive product *(pink line)*. Inset shows the color of corresponding solutions in an ambient condition. **[B]** Fluorescence spectra recorded at 510 nm excitation wavelength of red emissive product *(red line)*, isolated chloroplast *(green line)* and hybrid photosynthetic system *(pink line)*. Light harvesting activity of hybrid photosynthetic system. **[C]** Ferricyanide reduction assay of red emissive product *(hollow circle)*, isolated chloroplast *(green filled circle)* and hybrid photosynthetic system *(pink triangle)*.

When hybrid chloroplast has been irradiated with a light source (100 W filament bulb), the absorbance at 420 nm gest gradually decreased over time, which confirms the photoreduction of ferricyanide to ferrocyanide (Fig.3 6C). The ratio of change in absorbance to reaction time can quantify and compare photosynthetic activity rates of different samples. The rate of reduction of ferricyanide by the hybrid chloroplast system (0.0011 min^{-1}) was markedly higher than that by the chloroplasts alone (0.0008 min^{-1}). Red emissive product and chloroplast independently show poor reducing ability toward ferricyanide. Thus, the higher rate of reduction of Ferricyanide for the hybrid system is due to the combination and synergy of chloroplast and red-emissive product.

3.2.5. Fluorescent-tagging of Protein:

In this work, emissive products, P^R, and P^G have been directly used to tag the bovine serum albumin, BSA. The protein solution has been incubated in a phosphate buffer solution (PBS) at pH 7.4 for 6 hours with products P^R, and P^G separately at 37°C. The unreacted fluorescent molecules were separated by dialyzing the reaction mixture. The steady-state and time-resolved properties of fluorescent-tagged BSA have been presented in (Figure 3.7A-G). As a control experiment, It has been performed the dialysis of products, P^R, and P^G only and found that products can easily permeate through the membrane as confirmed by the absorption and emission spectra of the respective retentate. The synthesized probes can covalently bind to the protein, BSA, and show characteristics absorption and enhancement of fluorescence intensity. The fluorescence lifetime of tagged protein, BSA-P^R has been enhanced to 2 ns, which is suggestive of a change in microenvironment of the probe. Whereas a shorter fluorescence lifetime of BSA-P^G can be attributed to either dynamic quenching by phosphate ions or complex macromolecular interaction. It has been also ran SDS PAGE of BSA and fluorescent tagged BSA and found that the molecular weights of probes are very low to highlight any visible differences (Fig.3.7D & H).

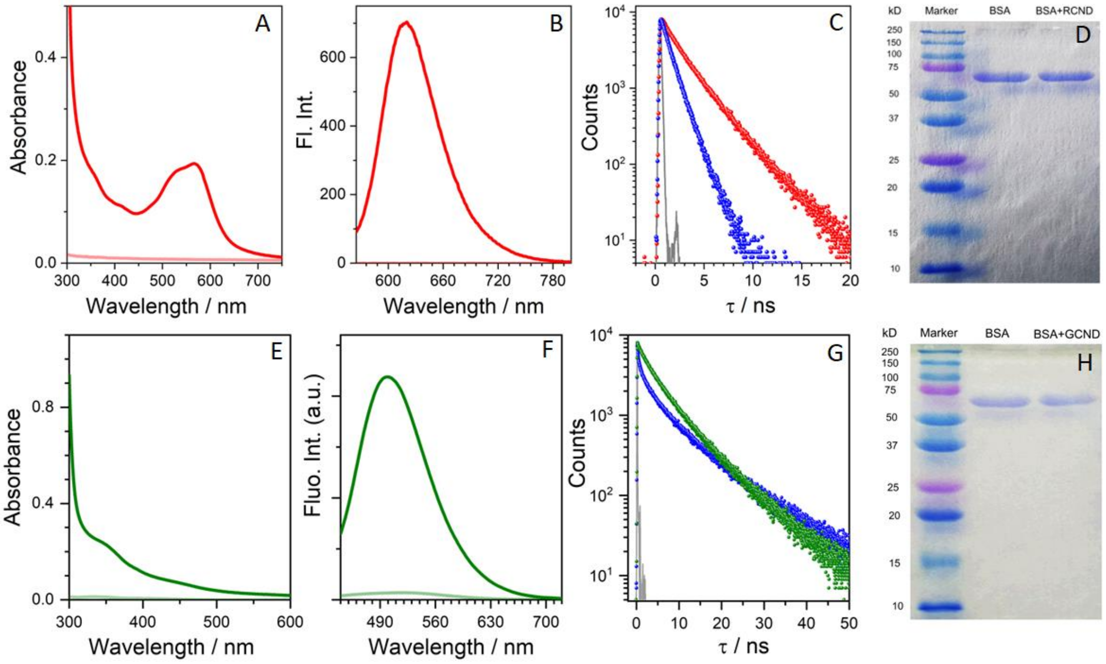

Figure 3.7: [A] Absorption spectra (red line), **[B]** Emission spectra (red line), **[C]** Fluorescence decay (red dots), and **[D]** SDS-gel electrophoresis of BSA-tagged red emissive product**. [E]** Absorption spectra (green line), **[F]** Emission spectra (green line) and **[G]** Fluorescence decays and **[H]** SDS-gel electrophoresis of BSA-tagged green emissive product. Fluorescence decay of unbound products are shown in grey dots for clarity and Corresponding data of control experiments are also included for comparison purpose.

3.3. Conclusion:

An effective separation method has enabled us to separate the emitters synthesized in solvothermal reaction of citric acid and ammonium thiocyanate. Addition of borax has augmented the photostability of synthesized products. The reactiveness of solvents is found to dictate the polyaromatic hydrocarbon. Accounting of emission characteristics and characterization results strongly suggest molecular nature of products. Aromatic pyrrolo-citrazinic ring is proposed to be the green-emitter whereas pyrrolo-pyrano-dicitrazinic ring is the red-emitter. The steady-state and time-resolved emission properties of products in neat solvents indicate do not follow common energy-gap law, rather display phenomenon of reverse solvatochromism. I observed surfactant-induced aggregation of red-emissive product in a cationic surfactant, cetyl-trimethyl ammonium bromide. Augmentation of emission properties (quantum yield and lifetime) of products at micellar surface is indicative of electrostatic sequestration from bulk water. Here, solvent-directed transformability of red-emissive product has been shown for the very first time. This switched product shares a great resemblance of property with the green emissive product synthesized in methanolic media. This piece of evidence not only validates the emerging hypothesis of molecular crystals, but also provides a rationale for molecular building up from green to red-emissive product. Synthesized products bind covalently to protein, bovine serum albumin, and thus can have potential applications in fluorescent-protein-tagging. A hybrid photosynthetic system has been conceived, that is made of chloroplast and red-emissive product. Red emissive product and chloroplast independently show poor reducing ability toward ferricyanide whereas a combination chloroplast and red-emissive product exhibits a higher rate of reduction of ferricyanide.

Chapter 4

Molecular Origin of Excitation-independent Emission of Carbon Nanodot

Easy one-pot method is being utilized for synthesis of carbon nanodot which has been investigated primarily from material perspectives. However, this preferred one-pot synthetic method suffers from the untrace ability of steps leading to the infusion of photoluminescence property in the nanodot. In order to resolve the steps involved, a single-precursor approach has been adopted here for the synthesis of the yellow-fluorescent probe by using a bio-resource, gallic acid. The synthesized probe exhibits excitation energy independent emission, a typical molecular behavior but shows emission wavelength-dependent lifetime, often attributed to Red-Edge Effect which is most commonly observed for nanodots. It has been proposed here that the observation of Red-Edge-Effect for synthesized probe in neat solvents is due to proton-transfer controlled solvation, a unique photoprocess. Characterization and computational results of synthesized product clearly suggest the formation of molecular fluorophore. Unprecedentedly, the synthesized probe shows proton-triggered red emission. Addition of proton has resulted in molecular aggregation due to a strong H-bonded interaction among product molecules. The presence of multiple-phenolic OH groups in the probe allows easy formation of molecular chains of crystals on transmission electron microscopic grids, causing observation of lattice spacing that remains unchanged at an aggregated state as well. It has also explored its possible applications in bio-imaging and trivalent metal ions sensing. It has better cell-membrane permeability, however, remains in the cytoplasm predominantly. Both green and red fluorescence are observed even inside the cell. The product molecule possesses sub-micromolar detection limit for aluminium ions as well, further confirming unaltered position of phenolic-OH groups present in product and substrate.

4.1. Introduction:

Affordability of stimuli-responsive fluorescent molecular probes is limited by the usage of expensive chemicals and inefficient methodology.[195] Hence, the development of such luminescent probes remains an attractive area of science. In general, a synthetic method for a fluorescent molecular probe is involved with a number of chemicals, reaction steps and thus its separations become highly cumbersome. Considerable efforts are underway to use one-pot synthetic method for preparation of luminescent probes owing to their profound applications in chemical and ion sensing,[196–199] light-emitting diodes[200,201], solar cell materials[202,203], and bio-imaging[204,205]. Nevertheless, a broader application of these probes is restricted by their non-emissive nature at an aggregated state.[174] Thus, a probe with high emissivity at both molecular and aggregated state is of greater importance.

In this direction, carbon nanodot is being developed and investigated for finding its wider applications. However, the reaction mechanism associated with the formation of nanodot is not known till date. Thus, such understanding is required to augment the its properties and also pinpoint the origin of its photoluminescence, which is an ongoing debate as well. Minimizing the reactants is undoubtedly a better method to predict the formation mechanism of nanodot. Hence, the single-precursor based synthetic method is an emerging method due to the minimization of usage and wastage of chemicals. Till date, costly chemicals such as phenylenediamines have been used as the single precursor for the synthesis of luminescent materials – carbon nanodots, but the molecular origin of their luminescence has not been understood clearly.[71,206,207] In literature, two kinds of carbon nanodots have been presented- most commonly excitation-dependent emission and another excitation-independent emission. Recently our group shown that the excitation-dependent emission is caused by the ground-state heterogeneity.[29,71] But the reason for observation of excitation-independent emission is not clearly known, which is suggestive of molecular behavior. Thus, it is highly intrigued us to identify the molecular entity.

On the other hand, the role of solvents in single-precursor-based synthetic method is not fully understood as well, often called solvent-engineering in carbon nanodot synthesis. In a reaction condition, solvents hardly participate, rather offer an inert media for reactants to facilitate the synthesis of desired products. In recent times, it has been hypothesized that the solvents can promote elemental doping, especially nitrogen and sulphur, but, the doping mechanisms remain an enigma till date.[21,165] Hence, it has immensely attracted us to resolve the role of solvent as a reactant.

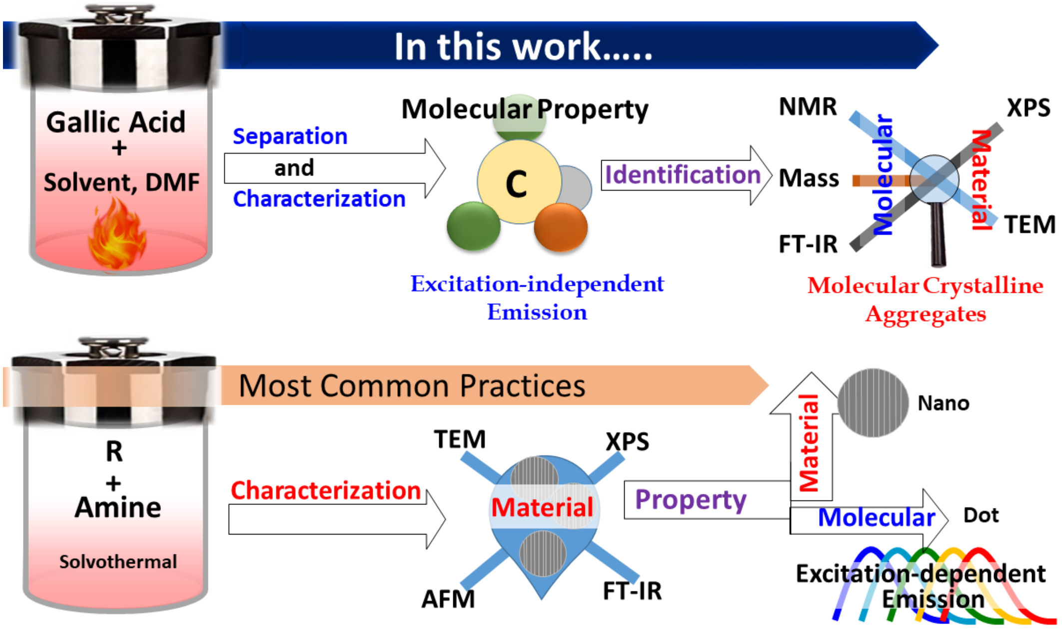

Scheme-4.1. Schematic representation of the single-precursor strategy adopted in this work and the most common practices in carbon nanodot research, R is a reagent of interest.

Accounting the issues associated with scaling up of a synthetic method, gallic acid is chosen here as a substrate, which is a naturally occurring triphenolic compound and commonly available among bioresources[208] and also found as an industrial waste[209,210] Nevertheless, gallic acid has been used primarily as an anti-oxidant and few cases as catalysts for organic transformations.[211,212] Apart from that, the gallic acid has only one identical reactive site, i.e. ortho-positions, and thus minimizes the statistical probability of by-products (Scheme-4.1). On the other hand, dimethyl formamide (DMF) is frequently used as a solvent for nanomaterials synthesis, polymerization, alkylation, decarboxylation, and also various types of organic reactions.[213–215] DMF is employed as a reagent in organic reactions, such as the Vilsmeier–Haack reaction, the Friedel–Crafts reaction, and Beckmann rearrangement.[216,217] Dimethyl formamide is hence chosen to serve the dual purpose-solvent and reactant for the one-pot solvothermal reaction with gallic acid. DMF can react as either an electrophile or a nucleophile, and thus, offer unique capabilities to mediate a series of organic transformations. It can take part in many organic reactions by providing building blocks of various kinds, such as CHO, CO, NMe_2, $CONMe_2$, Me, and others.[167]

In this chapter, first, attempted to rationalize the molecular origin of fluorescence of the product synthesized by one-pot method using gallic acid as precursor and DMF as solvent. Secondly, the anomalous excited-state emission dynamics has been understood by performing time-resolved studies and invoking area normalized time-resolved emission spectroscopy. It has been reported here an unprecedented proton-triggered aggregation-induced-emission (AIE) with a remarkable bathochromic shift in one stroke. The synthesized probe is found to buck the trend of the non-emissive nature of conventional dyes at an aggregated state. Both-product and its aggregated form have been tested for their applications in cell imaging as well. Also present here the colorimetric and spectrophotometric detection capabilities of the probe for metal ion sensing with sensitivity in sub-micromolar range for Aluminium (III) ion.

4.2. Results & Discussion:

4.2.1. Excitation-Independent Emission:

To identify the excitation-dependency of emission properties, the steady-state emission spectra of the product in ethyl acetate are recorded at different excitation wavelengths shown in Fig. 4.1A. Surprisingly, the product shows excitation – independent behavior that follows Kasha-Vavilov rule. The emission band maximum is centered at 526 nm. The absorption spectra of the product show a peak in the visible region at 424 nm in ethyl acetate solvent.

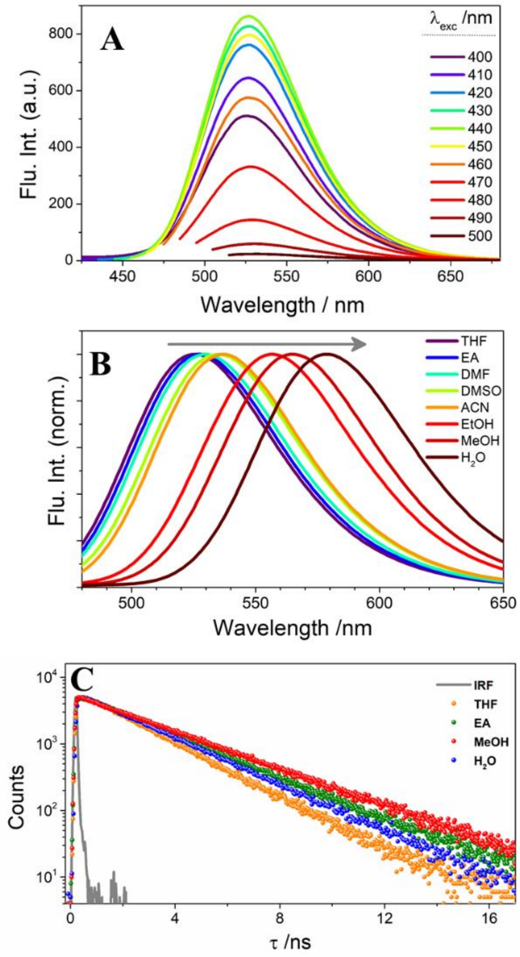

Figure 4.1. [A] Fluorescence spectra of product in ethyl acetate at different excitation wavelengths, **[B]** Emission spectra of products in various solvents**, [C]** Fluorescence decay traces at 580 nm emission wavelengths, λ_{exc}=405 nm. Water (blue dot), methanol (red dot), ethyl acetate (green color), tetrahydrofuran (THF). IRF is represented in grey scale.

The quantum yield of the synthesized probe is measured to be 0.53 in ethyl acetate and 0.32 in water at the excitation wavelength, 360 nm. Since organic fluorophores exhibit solvatochromism, hence the solvent-dependent emission properties of product have been investigated by recording its absorption and emission spectra in different solvents. As expected, the synthesized probe in solvents exhibits the classical solvent polarity dependence.[188] The emission maximum in solvents gradually red-shifted with increasing solvent polarity (Fig. 4.1B). However, a sharp solvent proticity dependence is clearly noticeable. A large Stokes-shift of more than 100 nm and good solubility in common organic and aqueous solvents make it a potentially good fluorescent probe for bio-imaging and solar cell applications.[218]

The temporal properties of product, P has been characterized by picosecond time-resolved measurements. The emission lifetimes of the product in different solvents are measured at 405 nm excitation with a fixed emission wavelength at 580 nm for the product. In THF, the decay trace is single exponential in nature with an average fluorescence lifetime, 2 ns confirmatory of molecular rigidity (Fig. 4.1C). With increasing solvent polarity, the emission lifetimes tend to increase by 1 ns (Table 4.1). Thus, the solvent polarity dependent emission properties of product, P is indicative of preferential solvation of synthesized probe in highly polar solvents, such as methanol (ε =32.7 at 20°C).

Table-4.1: Fluorescence decay parameters of synthesized fluorescent probe, P in various solvents. The excitation and emission wavelengths are- λ_{exc} = 405 nm, λ_{ems} = 580 nm

Solvents	τ_1 /ns	τ_2 /ns	τ_3 /ns	a_1	a_2	a_3	<τ> /ns	χ^2
Ethyl Acetate	2.21	3.68	0.26	0.73	0.05	-0.22	2.36	0.99
DMF	0.58	2.69	0	0.38	0.62	0	2.44	1.18
ACN	2.86	3.85	0.43	0.80	0.09	-0.11	2.99	1.04
MeOH	1.50	3.12	0	0.06	0.94	0	3.07	1.03
H_2O	0.54	2.49	0.11	0.17	0.21	0.62	2.20	1.17

Luminescence lifetimes, $<\tau> = \Sigma a_i \tau_i^2 / \Sigma a_i \tau_i$

Surprisingly, the decay trace in water does not follow the common polarity trend and becomes much faster with an average lifetime of 2.5 ns. The common apprehension on aggregation-caused quenching (ACQ) has been denounced by measuring the hydrodynamic diameters of the molecule in solvents by using dynamic light scattering.

The measured hydrodynamic diameters of synthesized molecules in solvents do not exhibit any aggregation behavior in water suggesting more-or-less similar type solute-solvent interactions. Hence, such a change in emission property of probe in water is perhaps due to the water-induced quenching. To bolster this hypothesis, a pyrogallols, has been used as a starting material as well. It has been observed that the obtained product (P_2) from pyrogallol is also fluorescent in nature and exhibits excitation-independent emission as well. However, the emission lifetime in an aqueous medium for product, P_2 remains the same, 2.5 ns.

4.2.2. Molecular Identification by Tracing the Steps of Solvent Engineering:

The complexity involved with the untraceability of steps leading to product formation in the one-pot method remains unresolved, hence, it has been attempted to address it here by unifying the characterization results. First, X-ray photoelectron spectroscopy (XPS) has been employed to determine the composition and chemical state of the elements present in the product. The full scan XPS spectrum of product, P, as shown in Fig.4.2A, presents three peaks at 532, 400, and 285 eV, which correspond to O 1s, N 1s and C 1s, respectively. No additional peaks are observed in the full survey, thus, confirming that carbon nitrogen and oxygen are the only three elements, apart from hydrogen. No additional peaks are observed in the full survey, thus, confirming that carbon nitrogen and oxygen are the only three elements, apart from hydrogen. The high-resolution scan of the C 1s region shows carbon presents in 3 different chemical environments (Fig. 4.2B), corresponding to C=C at 284.96 eV, C-N and C–O at 287.40 eV, and C=O at 288.45 eV from carbonyl and carboxylate. The XPS data of N 1s shows the presence of predominately amine (400.06 eV). Whereas three distinct peaks at

531.81, 533.32, and 535.87 eV in the O 1s spectrum (Fig. 4.2C) have been observed, that can be attributed to C=O, C–O-C, and O-H components respectively.[184]

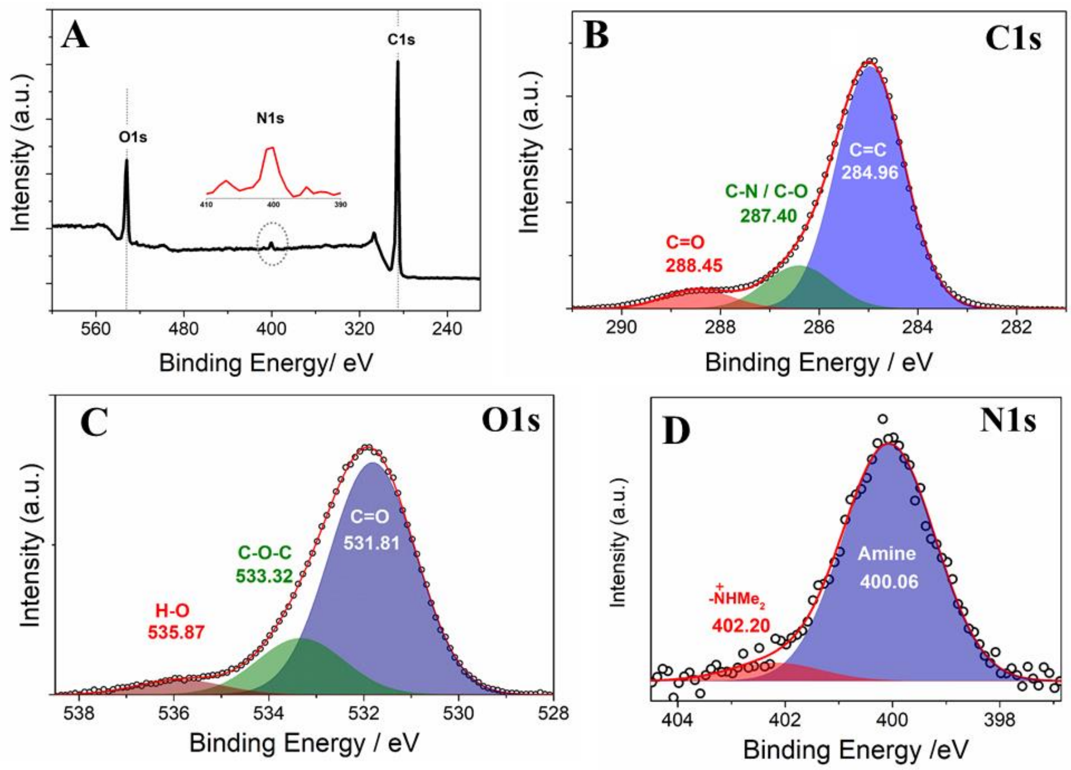

Figure 4.2. **[A]** Full survey XPS spectra of product. The high resolution XPS of- **[B]** C 1s core level and **[C]** O 1s core level of the product. **[D]** N 1s core level of the product.

In order to compare the elemental composition of product, P^Y obtained from starting material, pyrogallol, XPS results of both the products (P and P^Y) have been compared. It can be conclusively stated that both the products contained amine nitrogen (Fig. 4.2D). As expected, the XPS spectra of the element C 1s and O 1s of the product (P^Y) gets directly influenced by the high C/O ratio content of the starting material, pyrogallol, that in comparison with gallic acid. Thus, the study points toward the involvement of a common reaction pathway.

In order to gauge the presence of functional groups present in both the products, it has been used the FTIR spectroscopy. Also considering the direct role of starting material, the FTIR spectra of product, P and gallic acids are overlaid (Fig 4.3A). A visible difference can be noticed between the FTIR spectra of gallic acid and the synthesized product. From 3700 to 3000 cm^{-1}, the stretching vibrations of O–H, and COO–H contribute to the very broad IR band respectively. The involvement of a common reaction mechanism gets strengthened by the observation of uncanny similarity in the range, 3000 to 2750 cm^{-1} of the FTIR spectra of the products (P and P_2). The peaks at 2954 cm^{-1} and 2852 cm^{-1} are due to the stretching vibrations of aromatic (=C-H) and aliphatic C-H bonds.[219] The strong FTIR band at 1720 cm^{-1} belongs to C=O (carboxylic acid group) and relatively broadband, 1680-1510 cm^{-1} is indicative of C=O (carbonyl) and C=C vibrations respectively. FTIR peaks at 1387 cm-1 and 1090 cm^{-1} are assigned to the stretching frequencies of C-N and C-O-C bonds respectively.

Based on the observations, it has been proposed that in solvothermal condition, the first step is the formation of adduct by the condensation of two gallic acid molecules (Scheme-S4.2). Thereafter, formylation of adduct by solvent, DMF and followed by the xanthene formation. Dimethyl-formamide is serving as a formylating agent here, which is quite similar to the Vilsmeier-Haack reaction for formylation of electron-rich aromatic rings. Aromatic substitution of dimethylammonia has resulted in decarboxylation at electron-deficient benzene ring of Xanthene, yielding the fluorescent product, 1-(dimethylamino)-4,5,6-trihydroxy-3-oxo-3H-xanthene-8-carboxylic acid (**P**). For starting material pyrogallol, the reaction proceeds through a similar pathway, but the only difference is that there no decarboxylation for the formation of the product P^{Y}. The only difference of product, P with P^{Y} is the presence of one carboxylic acid which has a route from the precursor, gallic acid. Evidently, the presence of carboxylic acid group has resulted in better solubility of P in water over P^{Y}. Moreover, I have used pyrogallols, 3,4-hydroxy benzoic acid, benzoic acid as starting materials as well and found that the products obtained from the same reaction condition are non-fluorescent in nature. Hence, uniquely positioned triols in the gallic acid and pyrogallol are highly desired for infusing fluorescent property.

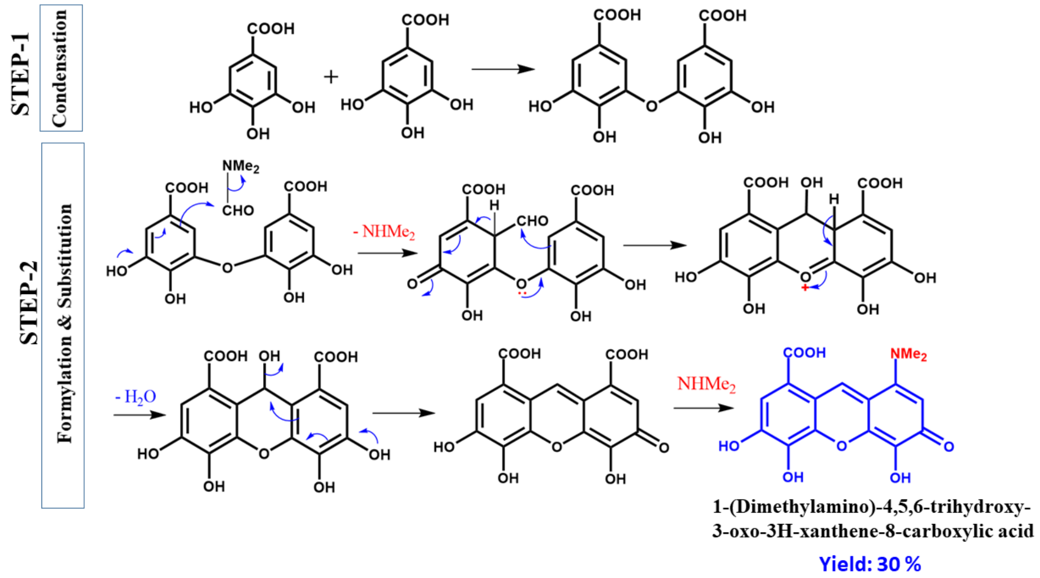

Scheme S4.2: Proposed reaction mechanism of formation product, Aminohydroxy-substituted Xantheone (P) from the reaction of gallic acid and solvent, dimethyl formamide.

4.2.3. Corroborative Evidences:

^{13}C NMR, ^{1}H NMR (Fig. A4.7) and mass spectrum of the product are suggesting the formation of fluorescent molecule, P. Moreover, it has been optimized the molecular geometry of the product, P using Density Functional Theory (Fig.4.3C). The optimized molecular geometry and Cartesian coordinates of the atoms in the product, P. The computed dipole moment (4.2 D) of the product molecule, P is relatively high, hence, satisfactorily explain the solvatochroism. The important stretching frequencies are computed and in good agreement with the experimental values. The computed vertical excitation (466 nm) with the lowest energy region at the ZINDO // B3LYP /6-311++G (d, p) level for the molecule is also in fair agreement with the excitation maximum at

440 nm (Table A4.1). And the transition in low energy region is found to be predominantly between the HOMO and LUMO. However, a difference of 26 nm in band maxima is due to the omission of specific interactions such as solvation, solute-solvent interactions, H-bonding. [28,186,187] Considering the presence of basic amino-group in the molecule, it has been also optimized the geometry of protonated form (mono-cationic) of the molecule (Fig. 4.3C). A significant change in dipole moments between the neutral (4.2 D) and protonated form (9.6 D) has been noticed, which may influence the time-resolved emission properties such as solvation of molecule.

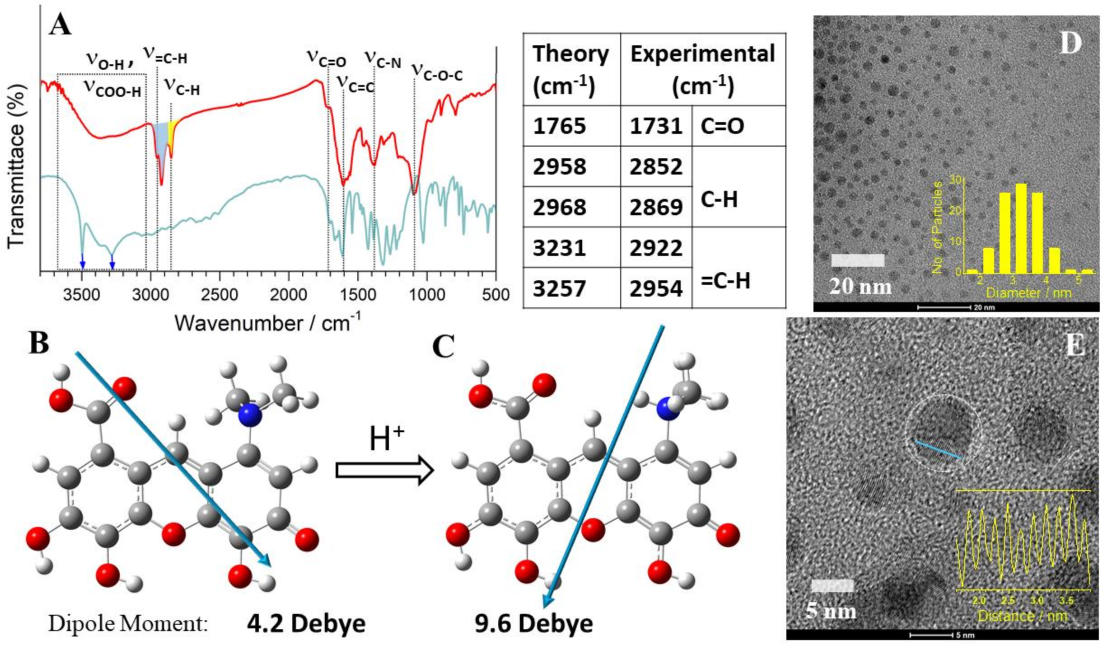

Theory (cm^{-1})	Experimental (cm^{-1})	
1765	1731	C=O
2958	2852	C-H
2968	2869	
3231	2922	=C-H
3257	2954	

Figure 4.3. [A] ATR FT-IR spectra of- (i) Product (red line); (ii) gallic acid (cyan line). Comparison of Relevant stretching frequencies with that of computed value. **[B]** Molecular structure of the Product, and **[C]** the Protonated form of the product. The orientations of dipole moments are shown. **[D]** TEM image of product; *Inset* - particle size distribution, **[E]** HRTEM image of product with lattice spacing of approx. 0.22 nm (*Inset*).

The high-resolution transmission electron microscopy (HRTEM) is employed to understand the morphology and size of the product, P. TEM images clearly show the typical particle formation (Fig. 4.3D), and the average diameter of the particles deposited is measured to be 3.3± 0.6 nm. Organic fluorophores generally form amorphous aggregates. Nevertheless, molecules having multiple hydroxyl groups such as pyrogallol, sucrose are known to form molecular chains at crystal states.[159,177] Expectedly, the high-resolution TEM images presented in (Fig. 4.3E) show two-dimensional nanosheets with the appearance of lattice fringes. The observed lattice spacing of 0.22 nm is generally referred to the facet [020] of graphitic carbon. Thus, the H-bonded molecular clusters (Fig. A4.2) of product molecules are perhaps the reason for the observation of lattice fringes in high resolution TEM images.

4.2.4. Excited State Emission Dynamics- Red-Edge Effect:

The presence of both acidic hydrogen (phenolic and carboxylic acid groups) and basic nitrogen (dimethyl amino group) in the product molecule may open additional an excited state process- proton transfers. Commonly observed solvation is generally manifested itself in the wavelength dependence of fluorescence decays and time-dependent Stokes shift (TDSS) of fluorescence spectra. Ethyl acetate as a solvent is chosen for this study due to its less polarity, $E_T(30) = 38.1$, and aprotic nature. Unexpectedly, the fluorophore in ethyl acetate exhibits a fast decay at the blue end and a rise at the red end of the emission spectrum (Fig. 4.4A). The rise time increases from 0.22 ns to 0.36 ns (Table A4.2). It is therefore pertinent to understand the dynamics and processes involved in the system. The conventional Time-Resolved-Emission-Spectra (TRES)[29,171] (Figure 4.4B) and Jacobian corrected TRES[220] are constructed for identifying the excited-state processes present in the synthesized probe. The time zero spectrum is relatively broader and has a maximum at 19230 cm^{-1} (520 nm), which is close to the value obtained in the steady-state spectrum of the fluorophore (19011 cm^{-1}, 526 nm). In the case of solvation, the time-dependent Stokes shift (TDSS) is expected to take place over a few nanoseconds to a saturation value. Surprisingly, no TDSS shift has been observed for the synthesized fluorophore in ethyl acetate, moreover, a second (shoulder) peak tends to appear at 17857 cm^{-1} (560 nm), with elapsing of time (Fig. 4.4B).

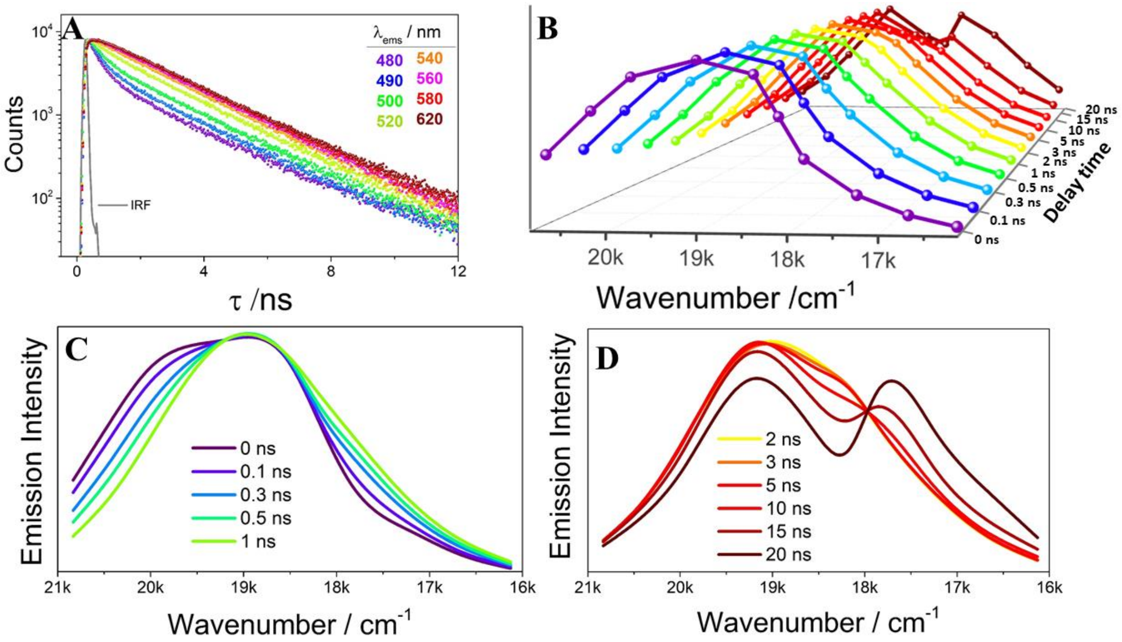

Figure 4.4. [A] The fluorescence decays of product in ethyl acetate recorded over emission wavelengths at λ_{exc}=405 nm. **[B]** The time-resolved emission spectra of product in ethyl acetate. With the increase in delay-time, a second peak starts to emerge. The time-resolved area-normalized emission spectra (TRANES) of product in ethyl acetate- **[C]** between time 0 and 1 ns and **[D]** between time 2 ns and 20 ns.

Periasamy and co-workers have developed the Time-Resolved Area Normalized Emission Spectra (TRANES) spectroscopic method and have established that an isoemissive point in TRANES indicates the presence of two distinct emissive species.[221] Two isoemissive points have been observed in TRANES, one at 19193 cm^{-1} (Fig. 4.4C) and another appears at 17973 cm^{-1} (Fig. 4.4D). It, therefore, suggests that there are predominantly two different processes are operative in the excited state of the molecule, one at a relatively faster time scale and another at a much slower time scale. The faster process may be attributed to intramolecular proton transfer and the slower one to solvation of that state.[222,223] It should be mentioned here that the dipole moment of the protonated form of product is relatively high, which might be a reason for the observation of slow-solvation.

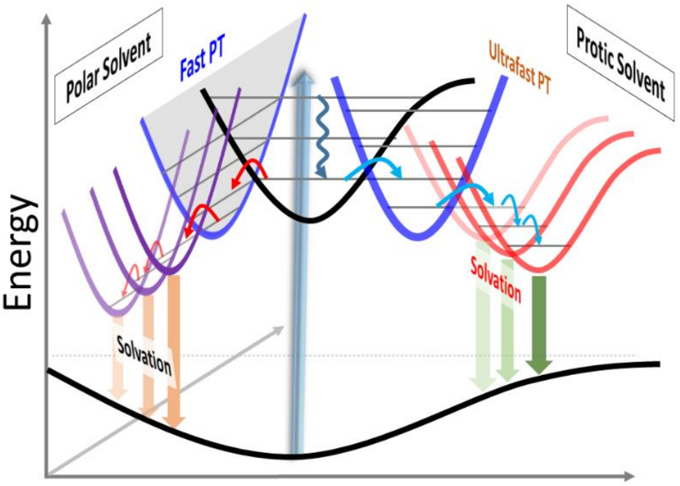

Scheme-4.3: Schematic representation of excited-state processes in the synthesized product in neat solvents.

A schematic potential energy diagram has been drawn to rationalize the excited state's processes associated with the synthesized fluorophore in two-type of solvents- polar aprotic and polar protic (Scheme 4.3).[224,225] For the construction of such a diagram, It has been considered three distinct observations- wavelength-dependent fluorescence lifetime with rise-time in ethyl acetate and without rise-time in methanol, two iso-emissive points in area-normalized emission spectra. The solvation in polar solvents is relatively slower than that in less polar media, thus rise-time is commonly observed at the red-end of the emission spectra. However, the emergence of rise time in less polar media suggests that the population in the solvation state is controlled by another process. Considering the presence of carboxylic acid and phenolic OH groups it is highly probable that the population in the solvated state is influenced by proton transfer. The proton transfer is expected to be much faster in methanol than that in ethyl acetate owing to the proticity of the former. Solvent such as water-mediated proton transfer is known to take place in ultrafast time scales. Water molecule forms water-bridge or water-wire for facilitating proton transfer in an excited state. Thus, I proposed that a similar kind of solvent-bridge for methanol is responsible for ultrafast proton-transfer.[226,227]

4.2.5. Proton-triggered Aggregation-Induced Emission:

Aggregation-induced emission is the result of restricted rotation of pivotal bonds (points) in an aggregated state or solid-state of non-fluorescent or weakly emissive organic dyes.[228,229] Naturally, a highly fluorescent organic dye exhibiting proton-triggered AIE is of immense importance, because the hydroxonium ion plays a decisive role in biological processes such as ATP synthesis, apoptosis, drug resistance, endocytosis, and muscle contraction. Thus, basic nitrogen is the preferred choice in the molecular design of AIE luminogens for infusing acid stimuli properties.[230,231] Upon protonation, the lone pairs of basic nitrogens present in the designed molecule are expected to lose conjugation, hence, the hypsochromic shift is an obvious outcome.[232]

The primary way to test whether a fluorophore is having stimuli-responsive AIE active or not is to make a comparison of the absorption and emission spectra between its aggregated and molecular states. Surprisingly. the product, P reacts with acetyl chloride fume and immediately changes color to pink from yellowish-green. Even, a drop of dilute HCl is good enough to observe such color change. Proton triggers the shifting of absorption peak maximum to 632 nm with a bathochromic shift of about 182 nm (Fig. 4.5A). The emission is found to be independent of excitation wavelengths and shows a band maximum at 648 nm (Fig. 4.5B). A small stokes' shift (390 cm^{-1}) thus suggests that the emission is originated from the aggregated state of fluorophores.[233] In order to understand the nature of aggregates, It has been carried out the time-resolved fluorescence study with excitation at 505 nm and emissions are measured at 640 nm and 680 nm respectively. The decay profiles of the aggregated states are single exponential in nature (Fig. 4.5C). The quantum yield of the aggregate is quite low and found to be 0.02 over an excitation wavelength region, 510-540 nm. Fluorescence lifetime is found to be independent of emission wavelengths and 1.0 ns (Table A4.3).

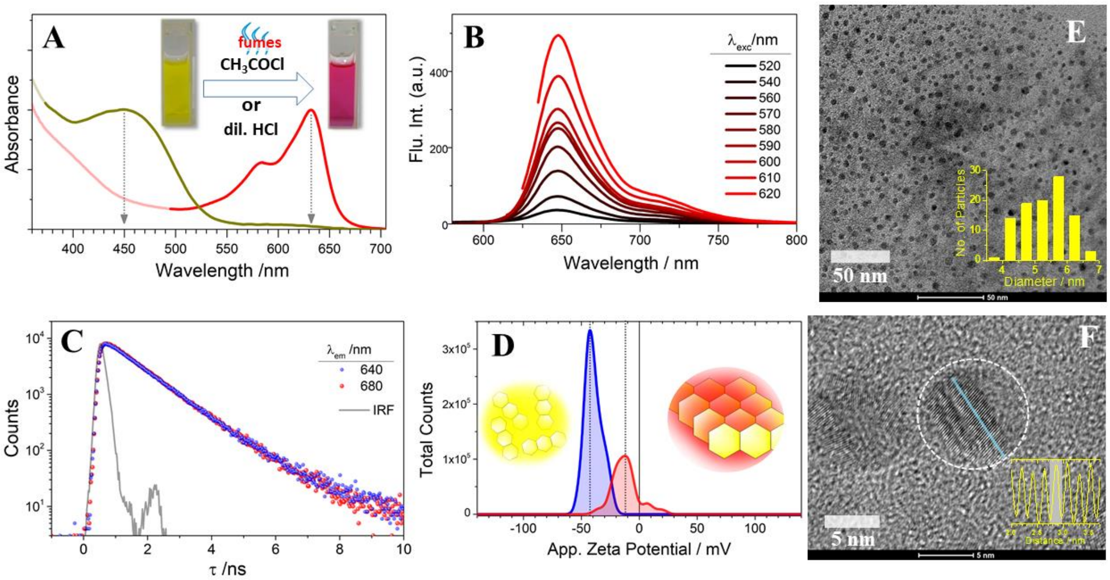

Figure 4.5. [A] Absorption spectra of product in aqueous solution- without addition of acid (dark green line) and with acid (magenta line). *Inset:* color change of solution under ambient light. **[B]** The emission spectra recorded at various excitation wavelengths. **[C]** The fluorescence decays of product in acidic environment recorded over emission wavelengths, λ_{exc}=510 nm**:** **[D]** Zeta potential of product in water- in absence of acid (blue line) and with addition of acid (red line). *Inset:* schematic representation of molecular arrangements contributing to respective emissions. **[E]** TEM image of product; *Inset* - particle size distribution, **[F]** HRTEM image of product with lattice spacing of approx. 0.22 nm (*Inset*).

The decreased lifetime upon addition of acid in comparison to that in THF further points out that the red-shifted emission is induced by aggregation. To further identify the state of emission upon addition of acid, it has been carried out Zeta potential studies of fluorophore in aqueous medium pre and post addition of acid. Acid addition has forced the Zeta potential to lie a range of agglomeration, -10 mV to -15 mV (Fig. 4.5D).[234] Hence, it suffices to ascertain that proton has elicited the fluorophore to organize in an aggregated state with strong emissivity. The origin of red emission may thus be attributed to the strong interactions of π-electrons present in aromatic rings of the fluorophore. [235]

The high-resolution transmission electron microscopy (HR-TEM) is employed to understand the morphology and size of the aggregated product. TEM images show the typical particle formation as well (Fig. 4.5E). The average diameter of the particle is 5.4± 0.7 nm, which is relatively larger than particles observed for product molecules at a non-aggregated state. Nevertheless, high-resolution TEM images presented in (Fig. 4.5F) show two-dimensional nanosheets with the appearance of lattice fringes. Nevertheless, the observed lattice spacing (0.22 nm) remains unaltered. This suggests that the molecular entity remains unchanged and secondly, protonation of molecule has promoted the formation of molecular chains at length (Fig. A41.2B).

4.2.6. Intracellular Co-localization of product:

Considering the high quantum yield and stimuli-responsive emission properties of the product, P is utilized for bio-imaging applications. Moreover, it is more intriguing to understand the subcellular localization of the product, hence co-localization study is performed. An aggressive colorectal cell line (HT-29) is chosen here primarily due to lower pH value (acidic environment) for cancer cells. The images were superimposed with blue emissions from Hoechst-33342, a DNA strainer, gets located inside the nucleus of the cell. Interestingly, a good superposition of fluorescence emission from products suggests that the synthesized product and its aggregated form can easily cross the cancer cell-membrane and enter inside of the cell (Fig. 4.6). Aggregated form of product, P shows both green and red fluorescence emissions, whereas the product shows predominantly red fluorescence emission. Notably, both- product and its aggregated form remain in cytoplasm, which is indicative of their identical molecular natures. Moreover, it should be stated here that the feeble green fluorescence emission and strong red emission for product, P are perhaps indicative of its relatively poor cell-membrane permeability over its protonated form. Thus, this study further provides a platform for its wider application in bio-imaging.

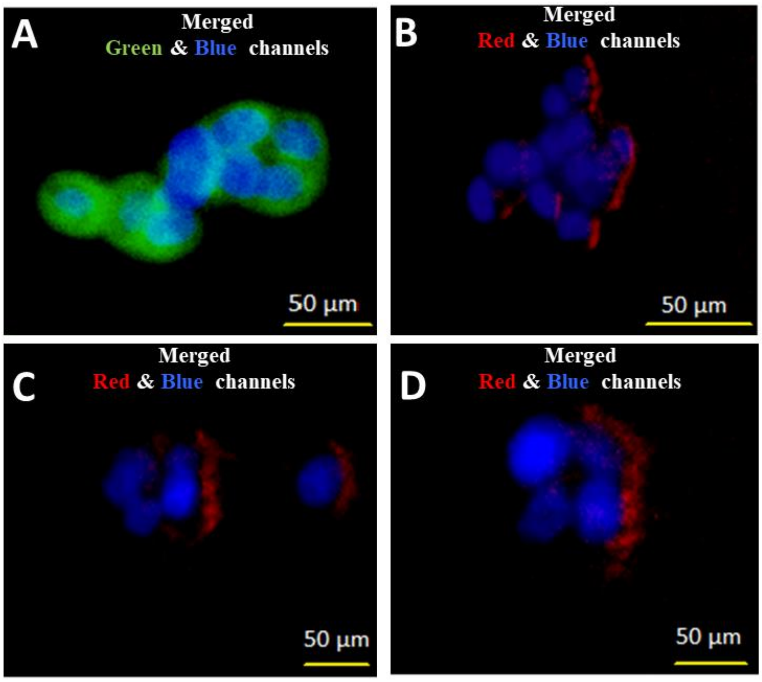

Figure 4.6. Co-localization study of the products in colon cancer cell line HT-29. **[A-B]** Aggregated product of P. **[C]** product, P **[D]** Aggregated product of Product, P_2.

4.2.7. Trivalent Metal Ion Sensing Ability:

The environmental pollution primarily caused by poor industrial waste management is the source of contamination of trivalent metal ions such as aluminium, iron, and cerium with water. Consumption of these metal ions beyond the physiological range leads to several diseases such as gastrointestinal disorder, neurotoxicity, Alzheimer's disease, and breast cancer.[236,237] Hence, their detections are of significant importance. Considering the affinity towards proton and the presence of phenolic groups in the molecular structure, it has been investigated the metal ion sensing abilities of the product derived from gallic acid.

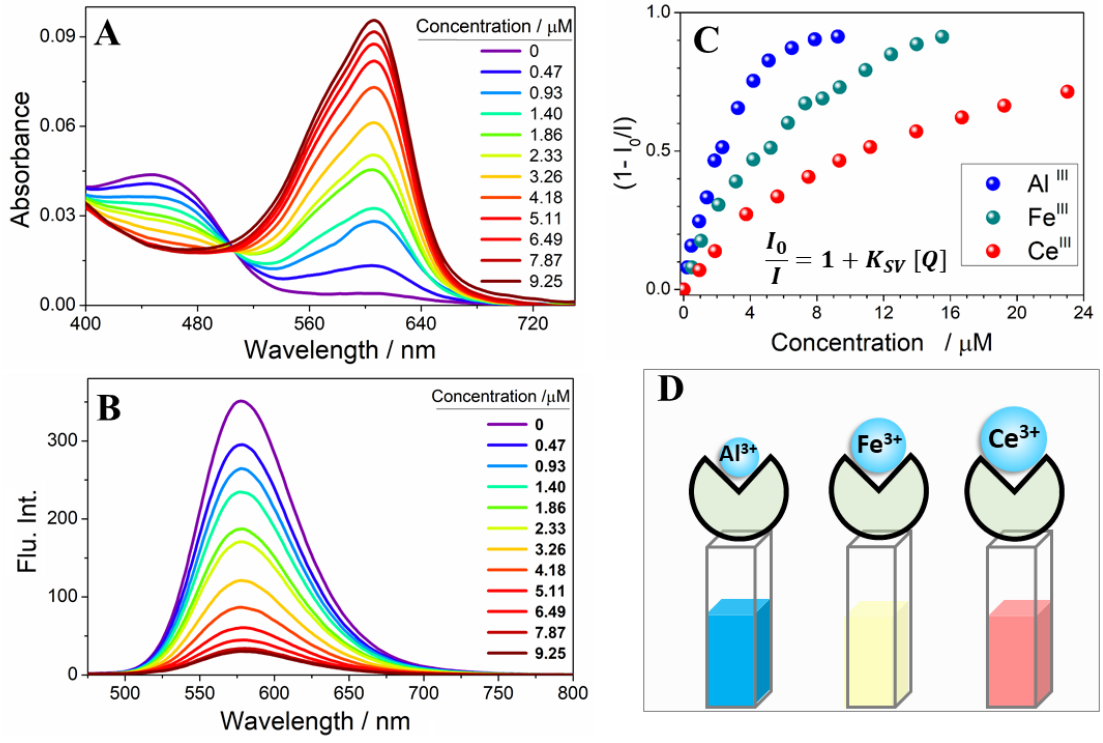

Figure 4.7: [A] The absorption, and **[B]** fluorescence titration spectra of product with gradual addition of trivalent, aluminum ion (AlIII). **[C]** The Stern-Volmer plots of product at different concentrations of trivalent ions-AlIII (blue circle), FeIII (green circle), CeIII (red circle) where I_0 and I are the fluorescence intensities of product without and with ions, respectively. K_{SV} is the Stern Volmer constant and Q represents quenchers (i.e., metal ions). **[D]** Schematic representation – effect of increased size of metal ions on their binding affinity with product, color change visible even under ambient light.

The electronic absorption spectra of the synthesized spectra in the presence of aluminium ion generate a new peak at a longer wavelength region i.e., at 607 nm (Fig. 4.7A). The broad red-shifted band gradually becomes prominent with the increase of metal ion concentrations. Two new peaks at 545 nm and 645 nm in UV-VIS spectra are observed for Fe (III), whereas, a gradual redshift of absorption peak maxima is noticed. Unprecedentedly, the fluorophore is having a sensitivity to 10^{-7} M level for aluminium metal ions (Fig. 4.7B).[238] The ionic radii of Al^{3+} is very small (0.053 nm) and can easily fit in the binding site of the product molecule. As expected, the emission of the fluorophore is getting quenched with the gradual addition of metal ions. The quenching is attributed to the static (association) quenching in nature. And the quenching constants (K_{SV}) are measured- 2.2×10^5 M^{-1} for Al (III), 1.1×10^5 M^{-1} for Fe (III), and 5.4×10^4 M^{-1} for Ce (III) (Fig. 4.7C). Interestingly, at the endpoint of the titration, the solution turns blue for Al (III), faded yellow for Fe (III), and reddish for Ce (III) offering easy naked-eye detection (Fig. 4.7D). It should be mentioned here that the probe is insensitive towards bivalent metal ions- such as Zn (II) and Mg (II) ions.

4.3. Conclusion:

In this chapter, presented here a cost-effective and one-pot preparation of yellow fluorescent probe from gallic acid. The underlying reaction mechanism- formylation followed by condensation and aromatization for the production of the molecular fluorescent probe is also being outlined. The ground and excited-state properties of the synthesized fluorescent probe in homogenous solvents are suggestive of molecular behavior and highlight the role of solvent polarity and proticity in dictating its emission dynamics. The observation of emission-wavelength dependent lifetimes is caused by the presence of carboxylic acid groups in the developed molecular probe. Construction of time-resolved emission spectra suggests the emergence of the population at a longer delayed time. Analysis of area normalized time-resolved emission spectra indicates the presence of at least three species at the excited state. This anomalous outcome has been explained by invoking an excited process- proton-transfer controlled solvation. Apart from this enrichment in fundamental understanding, it has been also offering the possible application of this synthesized fluorophore in- proton-triggered emission and trivalent metal ion sensing. The probe shows an unprecedented bathochromic shifts- 182 nm in absorption and 70 nm in emission. Such shift is attributed to aggregation-induced emission. Bio-imaging results suggest the product and its aggregated form easily enter inside of the cell and predominantly reside in the cytoplasm. The emission of the probe gets quenched (static quenching) the presence of trivalent- Al^{3+}, Fe^{3+}, and Ce^{3+} metal ions. The limit of detection for the Al^{3+} ion is 10^{-7} M. The probe also possesses colorimetric sensing capabilities for these metal ions.

Chapter 5

Scalable and Sustainable Photoluminescent Self-Assembly from Pyrogallol

---

Highly photoluminescent, single-component self-assembly being scalable and sustainable has a profound commercial significance. In this thesis, it has been address the existing challenges in development of self-assembly based on π-conjugated molecules– (i) feeble photoluminescence caused by poor molecular orientational ordering, (ii) costly fluorescent monomer owing to lack of atom/step/energy economical synthetic method. I have discovered that a bright yellow fluorescent Xanthene analog capable of instantly forming self-assembly can be synthesized by a home-build coil-in-spiral reactor using an inexpensive precursor, pyrogallol. Stimuli such as temperature (35^o C), acid fumes, and apolar solvent can trigger the formation of red-emissive self-assembly. In solution orientation of about 13 molecules yielding Hydrogen-bonded self-assembly has a direct resemblance with a Coulomb-coupled J-aggregate highlighted in the Kasha model. After photoexcitation, the excited state dynamics of the monomer progress via three pathways- (i) relaxation (2 ± 0.3 ps), (ii) solvation (19.5 ±3 ps), and (iii) decay (2.5 ns), whereas self-assembly exciton evolves via two pathways: (i) relaxation (81 ± 25 ps), and (ii) decay (~ 1 ns). In the solid state, the self-assembly retains the submicron-sized trigonal pyramidal structures by layer-by-layer stacking of triangular plates. This self-assembly doped in polymer even exhibits mechanofluorescence. Our study will pave way the use of this photoluminescent self-assembly for improved performance of organic/sustainable electronics and stretchable electronics.

5.1. Introduction:

The design of photoluminescent organic nanostructure by self-assembly of π-conjugated molecules is highly challenging.[239] Effective manipulation of inter-molecular noncovalent interactions is crucial to attain unique nanostructures.[240–242] The hydrophobic-hydrophilic balance thus dictates the nature of ordering of structures.[243–245] Striking a such balance is being done by ticking the functional groups of monomers. Among the hydrophilic interactions, Hydrogen bonding that is formed by the localized hydroxyl groups of monomers induced by temperature, pH of the medium offers a greater degree of control to tune morphology vis-a-vis photonic properties of self-assembly.[246–248] Hydrogen-bonded self-assembled nanostructures are omnipresent in living systems such as native protein, helical DNA, cellulosic fibers, and other derived structures.[249–251] Inspired by their monomer structures, it has been selected a natural product, pyrogallol as a precursor in synthesis of fluorescent monomer because it consists of localized hydroxyl groups that are capable of rapidly and robustly forming hydrogen bonds.[252–254]

Soft molecular assemblies are generating burgeoning interest for vivid applications in organic transistors, wearable technology, light-emitting diodes, and tandem solar cell.[255–257] Ordering of fluorophore assembly remains a bottleneck for facilitating fast and efficient charge transportation over a long range.[258] Long-range electron/hole transportation is advantageous for optoelectronic applications such as solar cells, organic transistors, and others.[259] The most common strategy adopted for designing a self-assembly is the introduction of hydrophilic chains into a hydrophobic π-moiety for tuning hydrophobic/hydrophilic balance.[243] However, photoluminescent molecular aggregate which was introduced by Kasha are formed by primarily cyanine-based dyes (pseudoisocyanine, merocyanine, and thiacarbocyanine, indotricarbocyanine).[258,260,261] Other chromophores are also reported to form emissive aggregates such as perylene di-imides, and porphyrins.[262–266] These molecular aggregates irrespective of their ordering (J or H) have inherent challenges- (i) very weak photoluminescence and (ii) highly expensive monomers. In this chapter, address the challenges of yielding highly photoluminescent single-component assembly (Scheme 5.1)

On the other hand, most of the synthetic methods used for commercially available fluorophores fail to address atom economy, step economy, and energy economy.[267,268] This has led to the increased production cost of cyanine-based dyes and other molecular fluorophores. Thus, developing an energy-efficient methodology for continuous production of fluorophores is of paramount importance.[269,270] Moreover, synthesized fluorophores having high emissivity at both molecular and self-assembled state are not only desired for organic electronics, but rather highly demanding in biotechnology and clinical research.

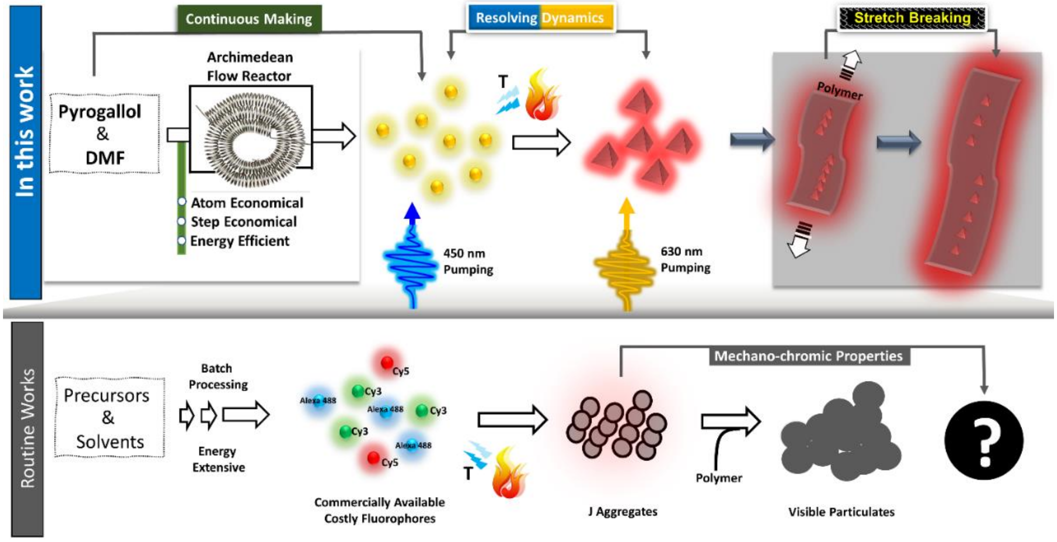

Scheme-5.1. Highlighting the research gap in photoluminescent organic nanostructure by self-assembly of fluorophores. Our 360° approach: scalable synthesis, sustainable precursor, and light-harvesting applications.

A continuous flow process is an efficient tool of reaction engineering over batch processes and thus has been preferred for its demonstration in this study. Large surface area to volume ratios of flow reactors leads to improve in heat and mass transfer rates, efficient mixing, and less waste generation.[271,272] Moreover, flow processes offer precise control of reaction parameters such as residence time control, and thermal control. Thus, the overall reactions become step economical and energy efficient as well. However, the over-dependence of flow chemistry on microreactor technologies poses significant challenges on scaling-up of processes owing to the blockage of microreactor channels by various solids. To address this challenge and it has been fabricated coil-in-spiral reactor (Archimedean type). Reaction of pyrogallol with dimethyl formamide, DMF (a reactive solvent) discovered for yielding fluorescent monomer is one of the simplest ones. No catalyst has been used for the synthesis. DMF has a unique ability to take part in reactions by providing building blocks of different types, such as CHO, CO, and others.[273] It is frequently used as a solvent for organic and nanomaterials synthesis and employed as a reagent in organic reactions, such as the Vilsmeier–Haack reaction, the Friedel–Crafts reaction, and Beckmann rearrangement.[29,167,213,274]

In this chapter, first, developed a scalable synthetic method for highly emissive molecular fluorophore from a sustainable precursor, pyrogallol. Secondly, photoluminescent self-assembled structure (Scheme 5.2) has been constructed by regulating temperature and concentration of the medium. Include, the complete excited state dynamics of molecular probe and exciton dynamics of self-assembled, one using time-resolved emission and femtosecond transient absorption studies. Unprecedentedly, the self-assembly of molecules attains trigonal pyramid (tetrahedral) structure. Electrostatic sequestration of these emitters in aqueous micellar media displays their surface charges. A polymer encapsulation strategy has been adopted to populate higher-order aggregates in our studies. Additionally investigated the role of axial stress in augmenting the emissive properties of ordered self-assembled structure in polymeric film.

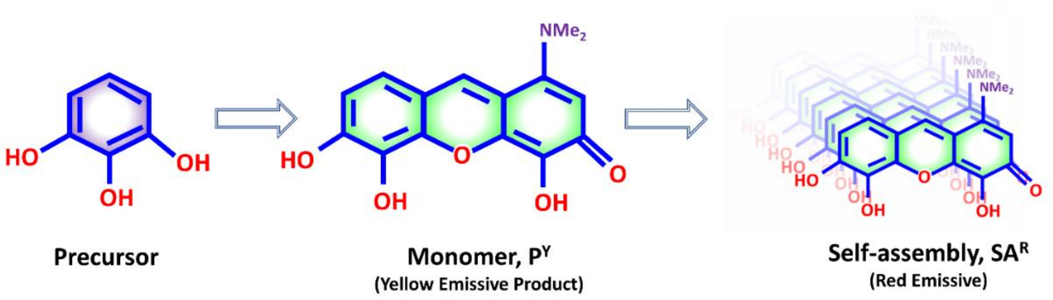

Scheme 5.2: Schematic diagram of steps involved in formation of self-assembly.

5.2. Results & Discussion:

5.2.1. Why is the Coil-in-Spiral Reactor (CSR) Advantageous?

Organic emitters are being routinely synthesized by energy-intensive batch processing methods. Thus, discovering a cost-effective synthetic method that addresses economic concerns is the first objective of investigation here. To do so, it has been selected mesoscale reactor over microreactor due to higher throughputs and lower pumping energy. The critical aspect of reactor design has been given due diligence to offer compactness, enhanced mixing, and transport processes including heat and mass transfer in continuous flow synthesis. Mostly used coiled tubes are becoming obsolete due to their lengthiness and the net flow rate-controlled mixing. It has been developed a Coil-in-Spiral reactor that is not only compact in design, rather its curvatures are expected to generate secondary flows normal to the direction of axial pressure-driven flows (Fig.5 1). Moreover, spiral geometries are known to enhance advective mixing and thus intensify other transport processes such as heat and mass transfer without any energy consumption (Fig. 2.1A).[272] It has been chosen a non-reactive, highly thermally conducting material- stainless steel pipe with internal diameter of 1 mm as a material for fabrication of desired Coil-in-spiral reactor (Fig. 2.1.B). To make our synthetic method an efficient one, DMF solution of gallic acid has been injected into Coil-in-spiral reactor at different flow rate by using a syringe pump. Owing to the complex relationship between centrifugal forces, and viscosity in a coil-in-spiral reactor, I have been calculated the Reynolds number instead of the Dean number. The net flow Reynolds number (Re_n) is defined as the $Re_n = \rho v D / \mu$ where ρ is the liquid density, v is the net flow velocity, D is the tube diameter, μ is the liquid viscosity.

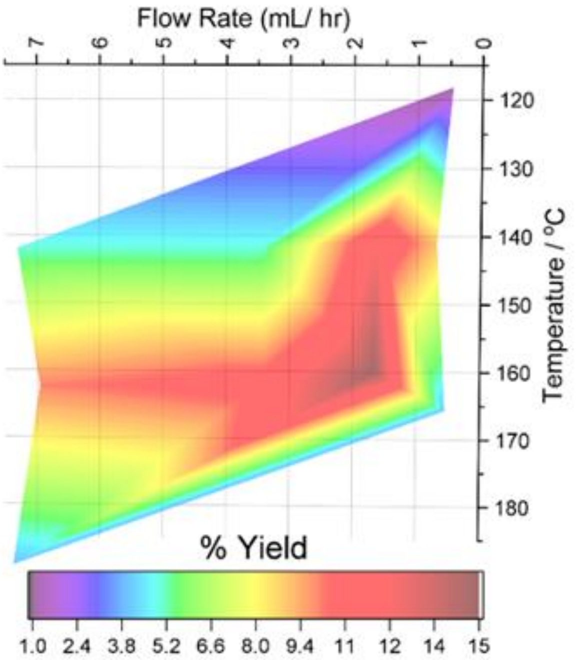

Figure 5.1. Dependence of operating conditions – flow rate and temperature on product formation (% Yield). 2D projection of data sets.

The Reynolds number, Re_n for the flow rate of 1.66 mL/hr is very low, 0.59 suggesting a laminar flow regime with a residence time of ~ 4.06 hr. The temperature of our highly compact reactor has been maintained by immersing it hot silicone oil bath and thereafter the solution coming from the reactor has been cooled down by passing it through a condenser dipped in cooled water bath. The yield of the obtained product has been optimized by varying flow rate and temperature (Fig. 5.1). It has been successfully synthesized product (P^Y) with a yield of 15% at 160°C without addition of any catalysts and found that 140-160°C temperature range and flow rate of 1.66 mL/hr to 3.32 mL/hr are the suitable reactions conditions.

To characterize the synthesized molecule, Fourier Transform Infra-Red (FT-IR) Spectroscopy has been employed first to identify the functional groups in the purified product.[150] Expectedly, appearance of a very broad IR band ranging from 3700 to 3000 cm^{-1} is due to stretching vibrations of O–H. However, a visible difference in spectra can be noticed between pyrogallol and the product obtained in the range, 3000 to 2750 cm^{-1}. The peaks at 2923 cm^{-1} and 2852 cm^{-1} are suggestive of stretching vibrations of aromatic (=C-H) and aliphatic C-H bonds.[219] The strong FTIR band at 1715 cm^{-1} is indicative of C=O (carbonyl) and C=C vibrations respectively. Further, it has been characterized the product by using X-ray photoelectron spectroscopy (XPS) to decipher the composition and chemical state of the elements present in the product. Peaks appearing at 533.1, 400.1, and 285.1 eV, are attributed to O 1s, N 1s, and C 1s, respectively (Fig. A5.1). Carbon (C 1s) exists in 3 different chemical environments such as C=C (284.8 eV), C-N/ C–O (286.40 eV), and C=O (288.0 eV). Nitrogen (N 1s) remains predominately in amine (399.9 eV) and quaternary ion (402.0 eV) forms, whereas three distinct peaks at 531.0, 532.2, and 533.6 eV in the O 1s spectrum are attributed to C=O, C–O–C, and O–H components respectively.[123] Nevertheless, the synthesized product has been characterized by elemental CHN(O) analysis, Mass spectrometry, and ^{1}H, ^{13}C NMR spectroscopy (Fig. A5.2). The characterization data are in good agreement with the proposed molecular structure of the product, 1-(dimethylamino)-4,5,6-trihydroxy-3H-xanthen-3-one (Scheme -5.3).

5.2.2. Building of Red-Emissive Self-Assembly in Solution:

Multiple phenolic-OH groups of pyrogallol-derived product, P^{Y} are positioned themselves to offer a directed H-bonding network.[275] Thus, the identification of stimuli to yield photoluminescent H-bonded self-assembly from yellow emissive product, P^{Y} is the most important aspect of investigation here.

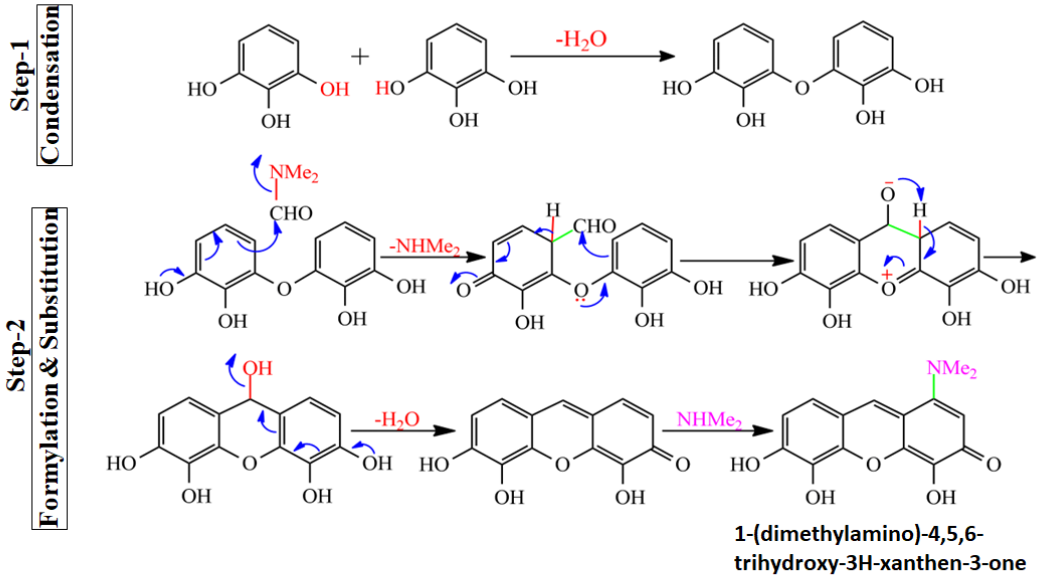

Scheme-5.3: Proposed reaction mechanism of synthesized product. This mechanism has been based on previous reports.

Synthesized product, P^Y exhibits a large stokes shift of about 105 nm with characteristics absorption and emission maxima centered at 460 nm and 565 nm respectively (Fig. 5.2.A-B). Unprecedently, yellow fluorescent monomer, P^Y instantaneously transforms into a bright red emissive state when it comes to contact with fume of either acetyl chloride or HCl. With a massive bathochromic shift of 162 nm absorption peak maximum of red-emissive state appears at 632 nm (Fig. 5.2C). Emergence of emission peak maximum at 642 nm signalling a very small stokes' shift of about 10 nm and low fluorescence quantum yield, ~0.08 point toward the H-bonded self-assembled state of P^Y fluorophores (Fig. 5.2D). Monomer and self-assembly exhibit excellent photostability Nevertheless, a dramatic drop of fluorescence lifetime by nearly 2 ns and slower decay of time-dependent anisotropy with 186 ps correlation time for red emissive state further confirm the H-bonded self-assembled state of P^Y fluorophores (Fig. 5.2E-F and Tab.5.1).

Table-5.1: Steady-state and Time-Resolved Fluorescence Properties of Product and its Self-Assembly in MeOH solvent.

Products	λ_{abs}^{max}	λ_{ems}^{max}	ϕf	τ1 (a1)	τ2 (a2)	<τ>	χ^2	Time-dependent anisotropy (ps)
	nm	nm		ns	ns	ns		
P^{Y}	451	565	0.46	2.98	-	**2.98***	0.99	123
SA^{R}	628	642	-	0.52 (0.28)	1.19 (0.72)	**1.09****	1.04	186

**Excitation: 405 nm for monomer,* $P^{Y,}$ *and 510 nm for self-assembly* (SA^{R})*.*
***Emission: 560 nm for monomer,* $P^{Y,}$ *and 640 nm for self-assembly* (SA^{R})*.*

The results are consistent with Kasha model that successfully accounts the photophysical properties of cyanine dyes.[260,276,277] According to this model, the head-tail ordering of molecules, often known as J-aggregates contributes to negative Coulomb coupling that causes the aggregation-caused red-shift and suppression of radiative lifetime.[258] Recently, it has been summarized that Coulomb-coupled J-aggregates must exhibit characteristic vibronic signatures in their absorption and emission spectra. The ratio of two vibronic peaks in absorption spectrum is 2.0 and that in emission spectrum stands at 7.5 in methanol. The increased photoluminescence ratio further confirms formation of J-aggregates and higher exciton coherence number.[278] A perfect superimposition of absorption and excitation spectra signals the presence of only one emitting species that is absorbing in the visible spectral range of light (Fig.5.2C). To determine the number of molecules (N) in H-bonded self-assembled state it has been assumed the self-assembled state as a quasiparticle in accordance with the exciton theory.[261]

$$N = \frac{3\Delta\nu_M^2}{2\Delta\nu_A^2} - 1$$

where $\Delta\nu_A$ and $\Delta\nu_M$ are the Full-width at Half Maxima (FWHM) of the steady-state absorption band of the H-bonded self-assembled state and monomer respectively. The number of molecules (N) is estimated to be 13 for H-bonded self-assembled structure.

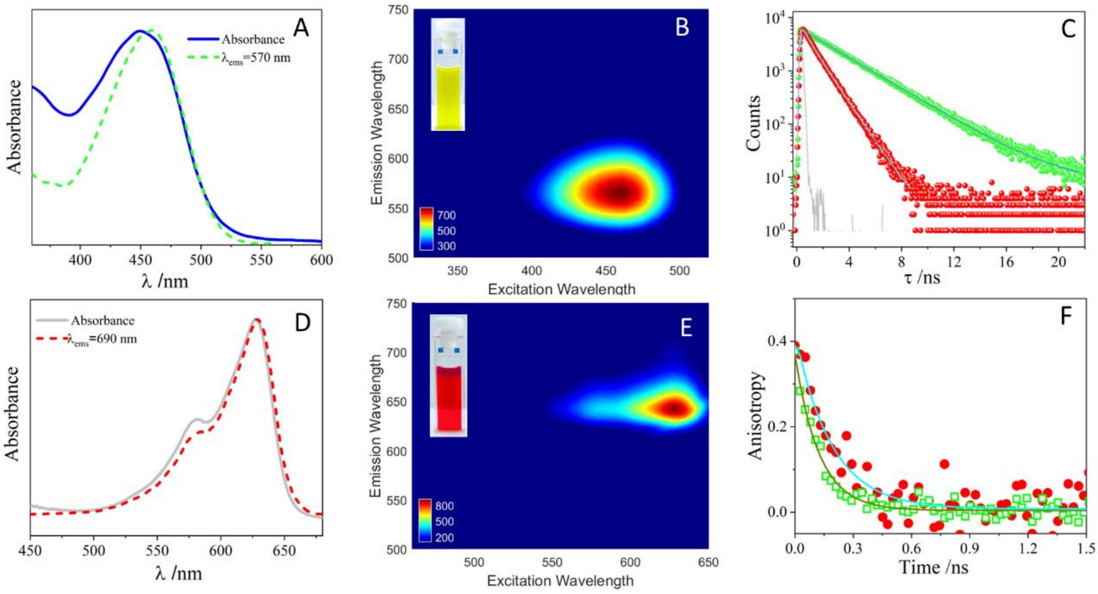

Figure 5.2. [A] Absorption spectrum (blue solid line) overlayed with excitation spectrum (green dashed line) of monomer, P^Y, **[B]** Contour plot of emission spectra with corresponding excitation wavelengths of monomer, P^Y in methanol. *Inset* –P^Y under ambient light. **[C]** Absorption spectrum (grey solid line) overlayed with excitation spectrum (red dashed line) of self-assembly (SA^R). **[D]** Contour plot of emission spectra with corresponding excitation wavelengths of self-assembly in methanol, SA^R. *Inset* – self-assembly under ambient light. **[E]** Time-resolved emission of products in methanol – P^Y at 560 nm, SA^R at 640 nm. Fitted line in blue color. Solid grey line shows the Instrument Response function. **[F]** Time-dependent fluorescence anisotropy of products – P^Y at 560 nm (red solid circles), SA^R (hollow green squares) at 640 nm in methanol. Fitted lines are represented accordingly.

At this juncture, it is essential to understand the driving force behind the instantaneous formation of H-bonded self-assembly. Organic fluorophores are known to form feeble fluorescent self-assembly subject to a large change in pH of the medium. It thus can be hypothesized that a subtle decrease in the pH of the medium caused by acid fume has caused a huge disturbance in hydrophobic/hydrophilic balance. To trace the point of inflection it has been used temperature as a probe to gently alter the ionic strength of the aqueous medium. The population of H-bonded self-assembly increases at the expense of the monomer, P^Y with increase in temperature (Fig. 5.3A-B) and emission intensity (Fig. 5.3C-D). A clear isosbestic point appears at 514 nm (Fig. 5.3A). It has been found that 35°C temperature at which pH= 6.84 in water is the point of inflexion for formation of H-bonded self-assembled structure. Concentration-dependent absorption and emission spectra (Fig. 5.3E-F) of product, P^Y further indicate that, unlike reported molecular aggregates, self-assembly of P^Y is caused by the salting-out. Thus, increased ionic strength of the medium and apolar solvents can yield H-bonded self-assembled structure of product, P^Y at ease.

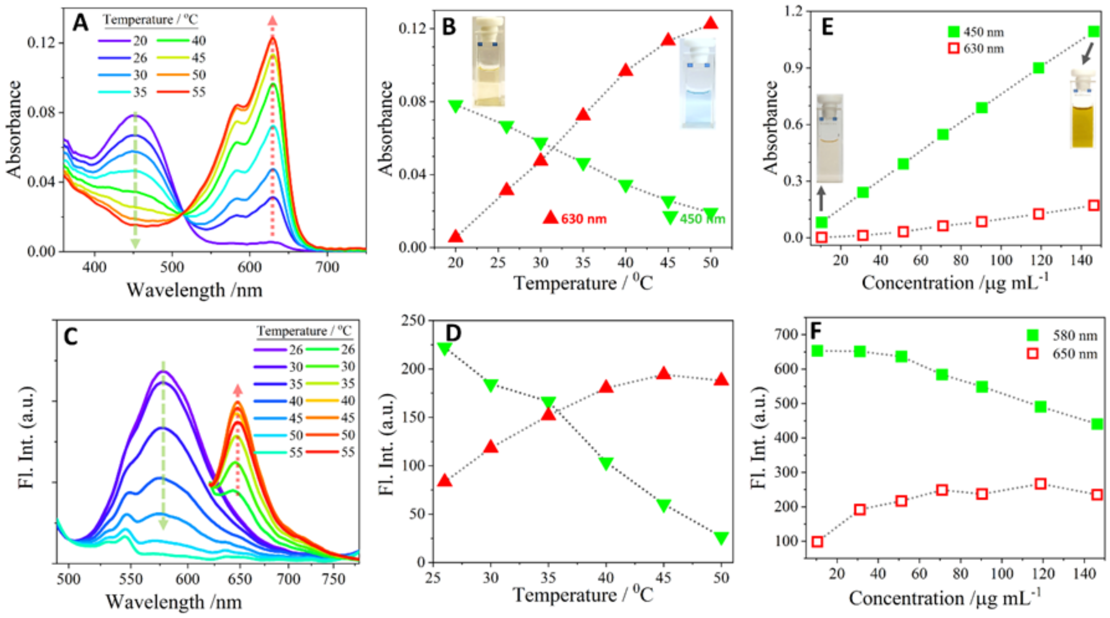

Figure 5.3: [A-B] Temperature-dependant absorbance spectra and absorbance maxima at 450 nm & 630 nm of product P^Y. **[C-D]** Temperature-dependent fluorescence emission spectra and emission maxima at 580 & 650 nm of product P^Y. **[E-F]** Concentration-dependent absorbance maxima at 450 & 630 nm and fluorescence emission maxima at 580 & 650 nm of product P^Y.

5.2.3. Electrostatic Sequestration by Anionic Surfactant:

Next, to confirm the positively charged surface of self-assembly in an aqueous solution and studied its interaction with ionic surfactants. Both product and self-assembled structure in an aqueous solution shows electrostatic sequestration with an anionic surfactant, Sodium dodecyl sulphate (SDS). A 10 nm hypsochromic shift in fluorescence spectra has been observed for product P^Y at 30 mM of SDS however, the self-assembled structure does not exhibit any peak-shift. the fluorescence gets intensified with gradual addition of SDS in an aqueous solution (Fig. 5.4). The quantum yield of product, P^Y exhibits a significant change from 0.28 to 0.40 and fluorescence lifetime from 2.3 ns to 3.2 ns (Tab. A5.1)). Self-assembly is expected to be larger in size and thus mostly resides on the stern layer of SDS micelle.

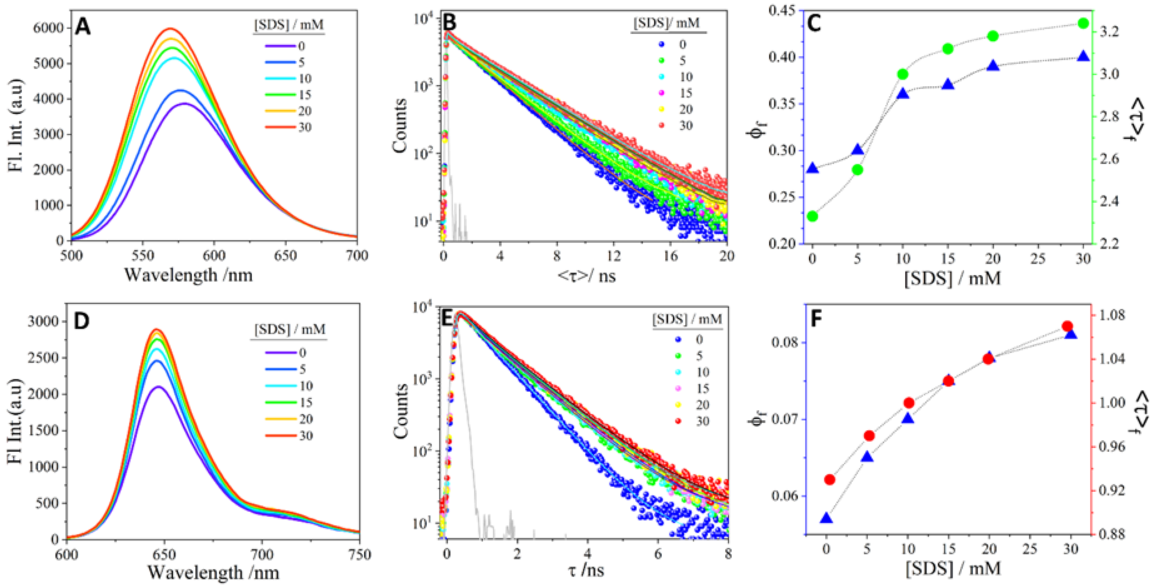

Figure 5.4: Fluorescence Emission spectra and decays of products in aqueous solutions at different concentrations of SDS- **[A, B]** yellow emissive product, P^Y and **[D, E]** Self-Assemble red emissive product, SA^R respectively. **[C, F]** Variation of fluorescence quantum yield, the concentrations of surfactant, SDS, and average emission lifetime of the products, P^Y and SA^R respectively. The quantum yield and average lifetime are represented as filled triangles and filled circles.

It has thus reflected in a marginal change in fluorescence quantum yield from 0.06 to 0.08 and fluorescence lifetime from 0.93 to 1.07 ns. Biexponential nature of fluorescence decay indicates the population of fluorophores in free state (bulk medium) and bound state (either on stern layer or complete micellization).[170,189,190] Both components (short, and long) get increased while their respective amplitudes remain more or less unchanged. Increased fluorescence quantum yield and lifetime can be attributed to electrostatic sequestration aided by the difference in micropolarity of SDS micellar surface and core with that of bulk water.

5.2.4. Exciton Dynamics of Self-Assembly in Solution:

Because highly emissive single-component self-assembly is hardly observed, excited state relaxation vis-à-vis light harvesting properties of this self-assembly are still unknown.[279] The ability of fluorescent product, P^Y to form emissive tetrahedron self-assembly allows us to do a comparative analysis of their excited-state dynamics.[280] Owing to the intense absorption bands in the 380−500 nm range for product, P^Y and 600-650 nm for self-assembly Transient absorption spectra (TAS) has been recorded under 400 nm and 630 nm pumping respectively. Two-dimensional (2D) contour plots of the TAS data matrix are presented in (Fig. 5.5A-B) and transient absorption spectra at different time delays in probing wavelength range, 340 – 760 nm are shown in Fig. (5.5C-D) for product, P^Y and self-assembly, respectively.

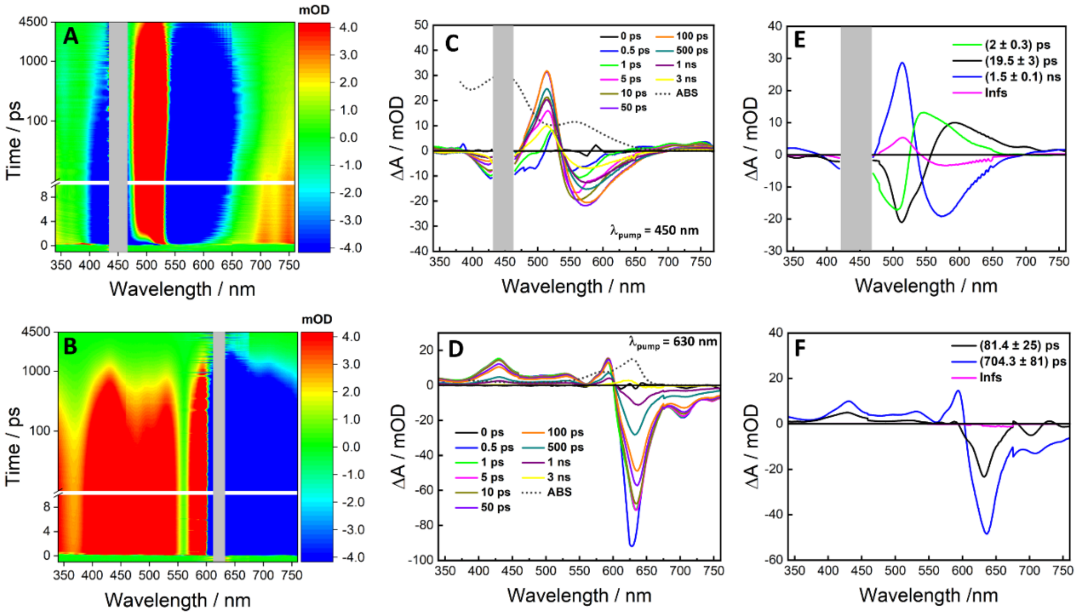

Figure 5.5. 2D contour plot of transient absorption spectra of- **[A]** product, P^Y and **[B]** its self-Assembly (SA^R) respectively. The time axes are linear up to 10 ps and logarithmic thereafter. Time evolution of transient absorption spectra for- **[C]** product, P^Y and **[D]** its self-Assembly (SA^R) respectively. Globally fitted lifetime spectra (EADS) of- **[E]** product, P^Y and its self-Assembly (SA^R) respectively. Grey rectangles only block the pump scatter.

Notably, an intense peak at 555 nm has been observed in steady-state absorption spectrum for a 300 μM solution of P^Y in ethanol. However, species contributing to 555 nm absorption is non-fluorescent one. Invoking the quasiparticle approach, it has been found that these aggregates are dimers of product, P^Y. Observation of non-fluorescent dimers for product, P^Y is quite consistent with organic dyes such as indotricarbocyanine and xanthene dyes.[260,261] Transient spectra of product, P^Y exhibited ground state bleach (430-460 nm), positive signals at 515 nm, 705 nm, and 751 nm and negative signals peaked at 575 nm (Fig. 5.5C). Moreover, an intense peak at 522 nm with a distinct shoulder peak at 488 nm have been clearly resolved for <5 ps time delay. The emergence of peaks at 488 nm and 522 nm can be attributed to the excited state and relaxed excited state. Broad excited state absorption (ESA) in the range 650-760 nm can be related with Stimulated Emission of concentration-guided self-assembly. On the other hand, transient spectra for self-assembly exhibited a broad excited state absorption in the range 430-593 nm, ground state bleach 620-650 nm and negative signals peaked at 560 nm, 705 and 747 nm (Fig. 5.5D). Excited state absorption in the range 430- 593 nm can be attributed to stimulated emission of the monomer, P^Y formed by the disintegration of self-assembly in excited state. Again, appearance of negative signals at 705 and 747 nm confirms the contribution of vibronic peaks. This strong emission is absent in the monomer. Rather a strong absorption is observed at the same wavelengths for the monomer. In the case of the aggregates, this signal appears as a stimulated emission that is significantly long-lived. The excited state absorption beyond 650 nm decays within 100 ps, while in aggregates the same emissions leave their signatures even beyond a nanosecond.

The Species associated decay spectra (SADS) obtained from the global analysis are shown in (Fig. 5.5E-F) for product, $P^{Y,}$ and self-assembly, respectively.[46,281] The global analysis of the transient absorption spectra of product, P^Y reveals three components with lifetimes- 2 ps, 19.5 ps, and 1.5 ns. Based on this it is proposed that excited state-1 of monomer P^Y relaxes rapidly to its state-2 in 1.9 ps and then state 2 further relaxes to its solvated state in 19.1 ps, respectively, and the lifetime of the solvated state is 1.5 ns (Fig. 5.5E) respectively. Whereas two decay time constants extracted from the kinetics of the transient absorption spectra of self-assembly are: 81.4 ps, and 0.7 ns (Fig. 5.5F). The 81.4 ps component corresponds to relaxation of excited self-assembly, which can be observed in the excited state absorption feature centred at 705 and 747 nm. Finally, the long-lived component of 0.7 ns is attributed to the lifetime of the relaxed self-assembly. It should be noted that the longer component retains all the spectral features as in the short component, however with an increased amplitude.

Thus, this state continues to evolve over this timescale. A Jablonski diagram has been presented for monomer and its self-assembly (Scheme 5.4) for better clarity.[259]

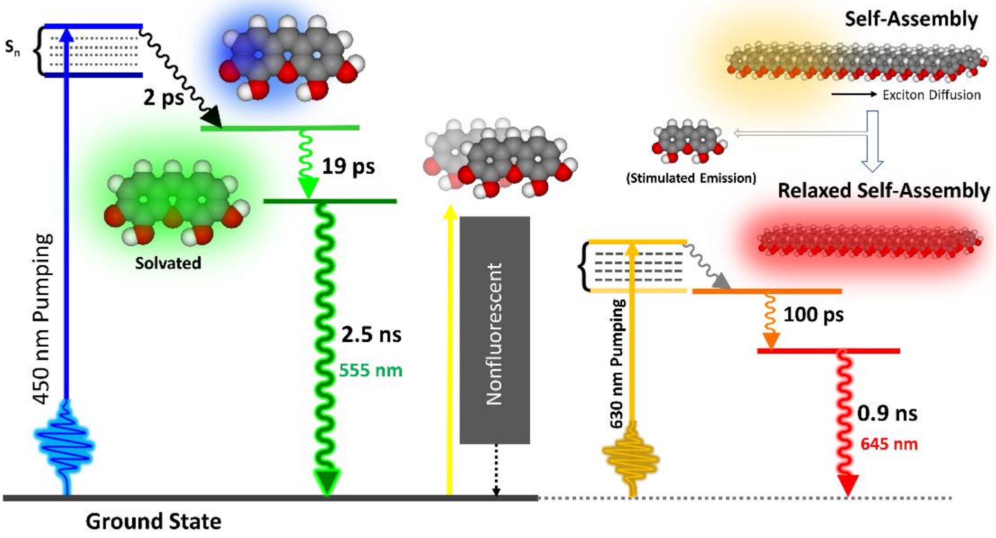

Scheme 5.4. Excited state dynamics of Product, P^Y and its self-Assembly under optical pumping at 450 and 630 nm respectively. Under the 450 nm pumping, product molecules, P^Y are promoted to the high-lying excited S_n state and relax to the top of the S_1 excited state (~ 2 ps component). Excited P^Y molecules can then get solvated (19 ps component). The 630 nm pumping promotes self-assembly to the top of the S1 exciton band. In this case, ~100 ps component is the relaxation time scale.

5.2.5. Structural Basis of Self-Assembly:

The advent of X-ray scattering enables us to identify the existence of molecular aggregates in solution. However, scattering intensity shares an exponential relationship with the size of molecular aggregates. To confirm the existence of self-assembly in solution and performed Small-angle X-ray scattering (SAXS) experiment.[282,283] (Figure 5.6A-B) show two-dimensional (2D) SAXS patterns of product, P^Y and self-assembly, SA^R in ethanolic solutions respectively at 300 µM concentration respectively. The scattering pattern of product, P^Y is almost isotropic reflecting the scattering from randomly distributed molecules. Whereas SAXS diffuse pattern is anisotropic for the self-assembly, SA^R. (Figure 5.4C) shows the plot of scattering intensity, *I(q)* versus scattering vector, *q* (nm^{-1}). Both profiles are quite similar except in the q range between ~0.03 and ~1.0 nm^1, however, no distinct diffraction peak has been detected for self-assembly. Emergence of nonlinear scattering and anisotropic diffraction patterns confirm that self-assembled state have a preferable orientation with face-to-face alignments in solution.

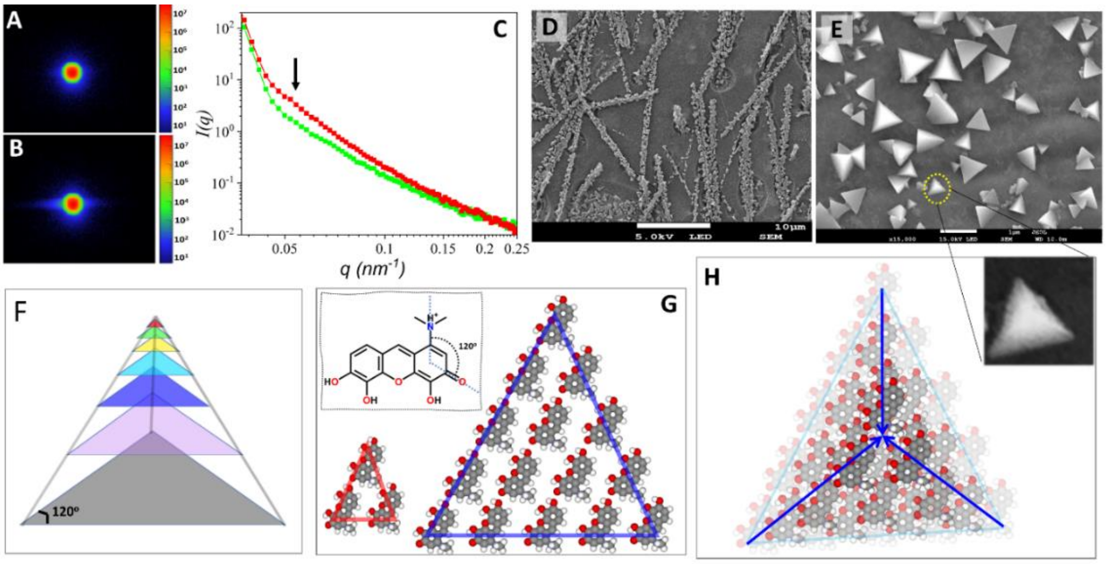

Figure 5.6: SAXS 2D scattering map of- **[A]** monomer, P^Y and **[B]** self-assembly, SA^R. **[C]** SAXS profiles of monomer (green squares) and self-assembly (red squares) in methanol. **[D]** SEM images of rod-like structure formed by trigonal pyramidal structures. **[E]** Isolated trigonal pyramidal structures of self-assembly. **[F]** Layer-by-layer stacking of triangular pyramid structure. **[G]** Molecular arrangements of different-sized triangular plates, *Inset:* Molecular structure of monomer highlighting origin of 120° angle. **[H]** Layer-by-layer stacking of triangular pyramid structure of Self-assembly.

Next, the role of H-bonding in the formation of self-assembly has been deciphered by high-resolution transmission electron microscopy (HRTEM). Drop-casting of a very dilute solution (20 μM) of SA^R on carbon-coated copper grid clearly resolves lattice spacing of 0.21 nm.[177] Such lattice spacings are also present in H-bonded molecular clusters. Thus, it can assert here that the functional groups (hydroxyl

& amine) of monomer contribute to form self-assembly in solid-state. Unprecedently, drop-casting of SA^R at a higher concentration (200 μM) on copper foil reveals the trigonal pyramidal structure of self-assembled state (Fig. 5.6D-E). The size of the tetrahedron structure of self-assembled state is 390 ± 97 nm. Notably, these tetrahedron structures assembled further in a linear direction to yield rod-like structures Observation of rod-like structure for J-aggregates is consistent with literature reports, however, assembly of triangular pyramidal structure resulting in rod-like structure is not known till date. Thus, to decipher the orientation of monomers in triangular pyramidal I have performed line-scanning on side of triangular pyramidal structure. It indicates a preferential orientation of hydroxyl groups at sides that perhaps causes the formation of rod-like structure. Such preferential orientation of hydroxyl groups is often found in crystal structure of pyrogallol and resorcinol. However, molecular orientation in self-assembly may be resolved in future by atom probe tomography.

On the other hand, the building up of tetrahedron structure can be rationalized by the layer-by-layer stacking of the triangular plates (Fig. 5.6F).[284] However, the formation of planar triangular plates requires a geometrical orientation of 120°. In product molecule, amine and carbonyl group share a desired angle of 120° (Inset, Fig 5.6G). Using the concept of triangular number, $n(n+1)/2$ it has been assert here that 15 molecules can yield a planar triangular plate (Fig. 5.6G). Interestingly this number is in good agreement with calculated no. of molecules (i.e., 13±2) forming self-assembled state in solution using exciton theory. Triangular pyramidal structure is thus produced by the layer-by-layer stacking of the different sized-triangular plates of molecules (Fig. 5.6H). To prove this hypothesis, it has been captured images of self-assembly at different timeframes. It resolves the layer-by-layer stacking of triangular plates (Fig. 5.7A-E) and the building up of triangular pyramidal structure from triangular plates (Fig. 5.7F-H).

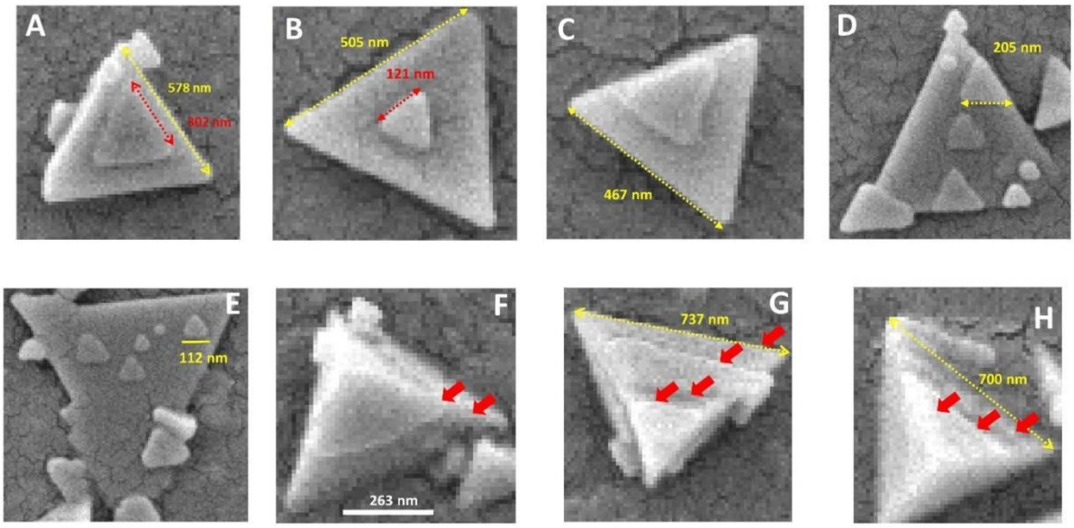

Figure 5.7: [A-E] Growth of smaller triangular plate on top of a large-sized triangular plate, **[F-H]** FESEM images of layer-by-layer stacking of self-assembly, SA^R

5.2.6. Mechanofluorescence by ordering aggregates in polymer:

Aggregation-caused quenching (ACQ) often accounts for the observation of the feeble emissive properties of aggregates caused by the random orientation of molecules.[285] It remains a challenge to augment the emission by ordering molecules in aggregates.[286] To do this experiment, it has been first doped the self-assembly (SA^R) in polymer films (Fig. A5.3). It has been selected two polymeric environments – hydrophobic PVDF and hydrophilic PVA/PVP. The emission peak of SA^R-doped PVA/PVP films is centered at 651 nm and registers a red-shift of 10 nm in comparison that of doped PVDF films (Fig. 5.8A), while it's blue-shifted by 10 nm in comparison to emission peak appeared for solid self-assembly. Notably, a vibronic peak distanced from prominent peak by approx. 60 nm (± 3 nm) is gradually intensified with concentration of self-assembly

(Fig. 5.8B). It is thus indicative of the presence of higher-order molecular aggregates in polymeric environment. Self-assembly (0.125 mg/mL)-doped PVA/PVP (2%) film has been chosen to study the mechanofluorescence over doped PVDF films due to its stretchability and elasticity.[150,287]

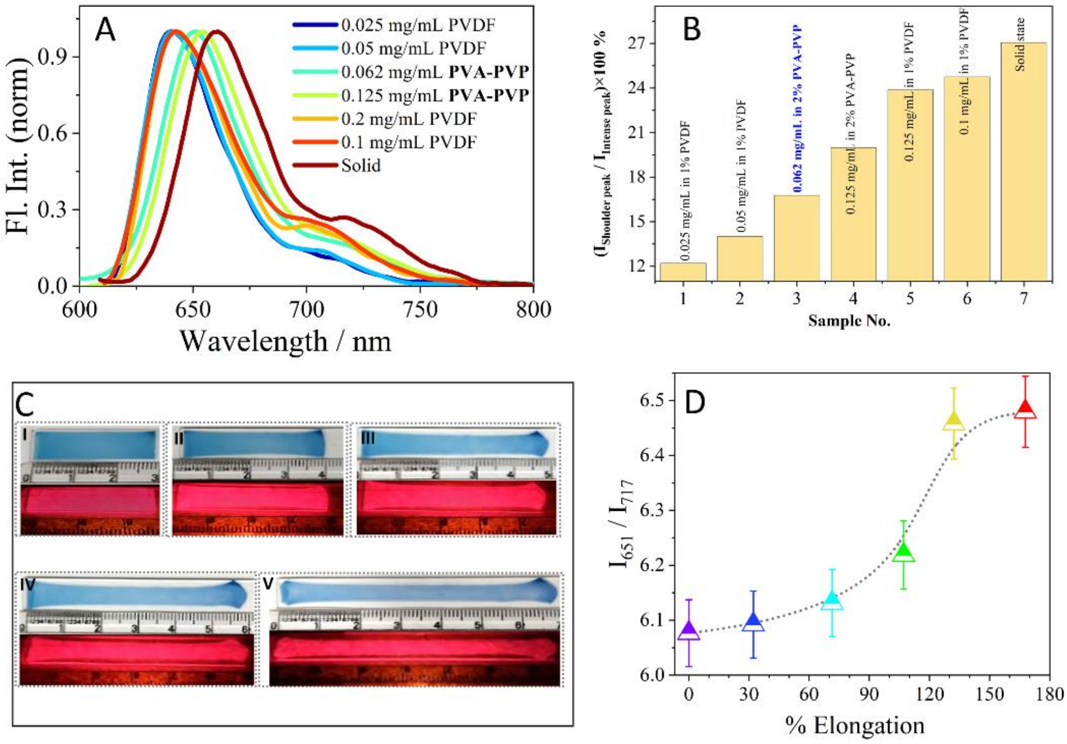

Figure 5.8. **[A]** Peak-Normalized Emission Spectra of Self-assembly doped polymer films. **[B]** Ratio of Intensities ($I_{intense\ peak}$ /$I_{shoulder\ peak}$) for Self-assembly doped polymer films. **[C]** Representative photographs Self-assembly doped PVA-PVP films under axial states (I→ 0%, II→ 33.3%, III→ 70.4 %, IV→ 103.7%, and V→ 140.7%). Images of polymer films under Ambient light (blue strips) and under 530 nm irradiation (red strips). **[D]** Ratio of Intensities ($I_{651\ nm}$ /$I_{717\ nm}$) at different stretching states of Self-assembly (0.062 mg/mL) doped (2%) PVA-PVP film (λ_{exc} = 630 nm).

Nonetheless, SA^R -doped PVA/PVP possesses not only a satisfactory stretchability of 140% and the recovery of emission over a period of time (Fig. 5.8C). In ambient light, the film is dark blue in color where under 530nm excitation, it exhibits red fluorescence. The absorption and fluorescent spectra of this self-assembly doped PVA/PVP film at different elongation has been recorded. The absorption peak is being gradually decreased with elongation, thus confirming the lowering of concentration in the area that resulted from stretching. To account for the augmentation of fluorescence intensity by polymer stretch it has been performed ratiometric analysis (Fig. 5.8D). The ratio of intensities (I_{651}/I_{717}) is gradually increased with increased tensile stress, demonstrating the ordering of aggregates. This is in also agreement with the Coulomb-coupled model of J-aggregates- the ratio of vibronic peaks should increase with increasing energetic order.[278,288]

5.3. Conclusion:

In summary, it has been developed a flow chemistry protocol for synthesis of yellow fluorescent monomer, xanthene analog from pyrogallol. The monomer instantaneously forms H-bonded photoluminescent self-assembly in solution at a mild temperature of 35°C or by subtle change in pH of the medium. Under photoexcitation, monomer follows the common trend of an excited state dynamics (locally excited state→ solvated state) in solution, whereas self-assembly exciton exhibits relatively slower relaxation and long decay which are advantageous for tuning electron/hole transportation in organic electronics. Unprecedently, unique H-bonding network plays a decisive role in evolving submicron-sized trigonal pyramidal structure in solid state. Further exploited these structural features to turn on mechanofluorescence properties of self-assembly. Such mechanofluorescence properties can exploited for stress detection, stretchable electronics.

Chapter 6

Summary and Future Scope

6.1. Summary:

This thesis extensively delves into the fundamental understanding of carbon nanodots, including critical aspects such as the origins of their photoluminescent properties, the influence of doped elements on luminescence, solvent selection in precursor materials, structure determination, the significance of single precursors, and the stimuli-responsive behavior of organic self-assembly J-aggregates. It meticulously explores the synthetic methodologies, covering both batch reactions and continuous modes. Moreover, the it deciphers the role of strain properties in higher-order aggregates within polymer films. This thesis concludes by examining the burgeoning applications of carbon nanodots in diverse fields, such cell imaging, metal ion sensing, white light generation, and photocatalysis.

In this thesis, a common solvothermal method has been used where reaction of citric acid as a carbon source and ammonium thiocyanate as a nitrogen source have been utilised to prepare two types of molecular fluorophores. One is a green emissive product in MeOH medium and the other is a red emissive product in DMF as well. The molecular weight of products was calculated by the HR-Mass spectroscopic technique. The possible reaction mechanism for the formation of products has been proposed. The surface charge of synthesized products has been determined by the interaction of surfactant. For the very first time, a switchable green emission from red emission has been obtained by solvothermal heating and comparatively studied the spectroscopy as well as molecular building block of red emission and the concept of graphitic-N versus molecular-N was discussed. The binding study was performed with bovine serum albumin and synthesized products. Hybrid photosynthesis system with different sets of chloroplast and fluorophore products was used to execute ferricyanide reductions.

The curiosity of molecular origin of excitation-independent emission spectra, yellow emissive product with excitation wavelength independent emission has been developed using a single precursor approach absence of nitrogen, low cost, less toxicity, and biocompatible organic material. In this, one-pot solvothermal reaction was used with gallic acid and DMF for 24h and 160°C temperature. The synthesized yellow emissive product can give stimuli-responsive red emission in the presence of acetyl chloride fume or a few drops of dil.HCl, where the red emissive form also exhibits excitation-independent wavelength emission spectra. The product has been utilized for bioimaging and selective trivalent metal ions sensing.

The latest work introduces a flow chemistry method for continuous and scalable synthesis of a bright yellow fluorescent product from an inexpensive pyrogallol unit. A simple home-build coil-in spiral reactor was constructed to achieve atom/ step/ energy cost-effective synthetic route and product formation. The existing challenges in organic π-conjugated self-assembly, J-type molecular aggregates, and calculation of the no. of molecules present in aggregates has been addressed by limited studies. The study accomplished the stimuli-responsive red emission property of yellow monomer on the treatment of temperature (35°C), acid fumes, higher concentrations, and apolar solvent. Further, the work includes solid-state self-assembly of phase pure unique structure of trigonal pyramid crystal formed by layer-by-layer stacking of triangular sub-micron sized plates and mechanofluorescence of red emissive aggregates in polymer film.

6.2. Future Scope:

It can be concluded that carbon nanodot is an aggregate of organic fluorophores. However, the molecular structure of carbon nanodots has not been determined. Hence the immediate scope would be-

(i) obtaining single crystals of all the synthesized organic fluorophore products.

(ii) metal-free photocatalysis to produce green hydrogen production effectively.

(iii) cascading energy and electron transfer in a doped polymeric network.

However, there also exists a long-term plan for versatile application of such heterogeneous mixture of emissive fluorophores.

(i) Emissive Zero-dimensional covalent organic framework,

(ii) Luminescent hydrogen-bonded framework for sensing of health hazards.

(iii) Photo(electro)catalytic reduction of CO_2 to methanol & methane.

Appendix:

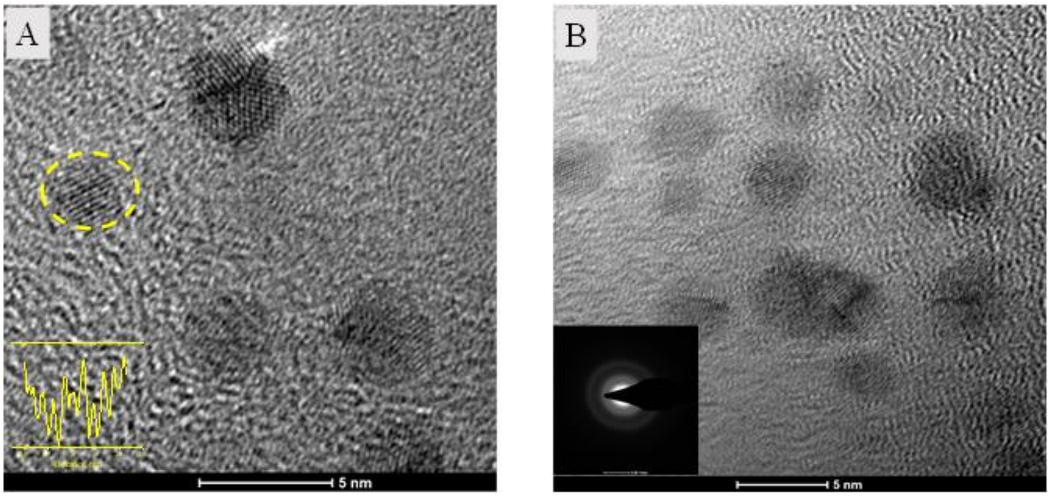

Figure A3.1: [A-B] HRTEM images of the product, P^R with lattice spacing. *Inset*-Diffraction pattern.

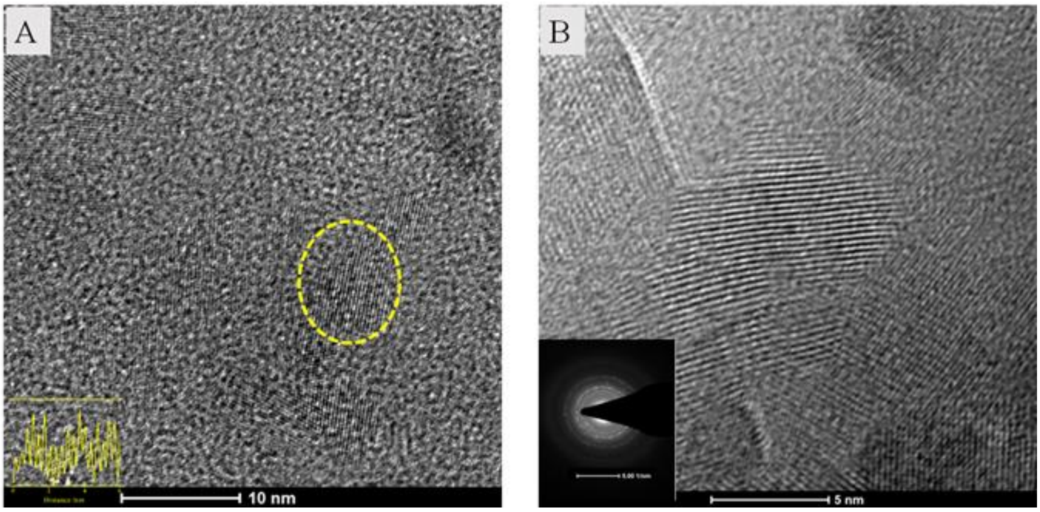

Figure A3.2: [A-B] HRTEM images of the product, P^G with lattice spacing. *Inset*-Diffraction pattern

Table A3.1: XPS binding energy data of products- PR and P^G products

Red-Emissive Product (P^R)	B.E /eV	Bond		Green-Emissive Product (P^G)	B.E /eV	Bond
C 1s	284.63	C=C		C 1s	284.94	C=C
	286.20	C-O-C				
	287.67	C-O/C-N			286.45	C-O/C-N
	288.87	C=O			288.79	C=O
O 1s	531.48	O=C		O 1s	531.84	O=C
	532.94	C-O-C				
	535.82	O-H			536.10	O-H
N 1s	399.66	Citrazinic-N		N 1s	398.42	Pyrollic-N
	402.25	Oxide-N			400.01	Citrazinic-N

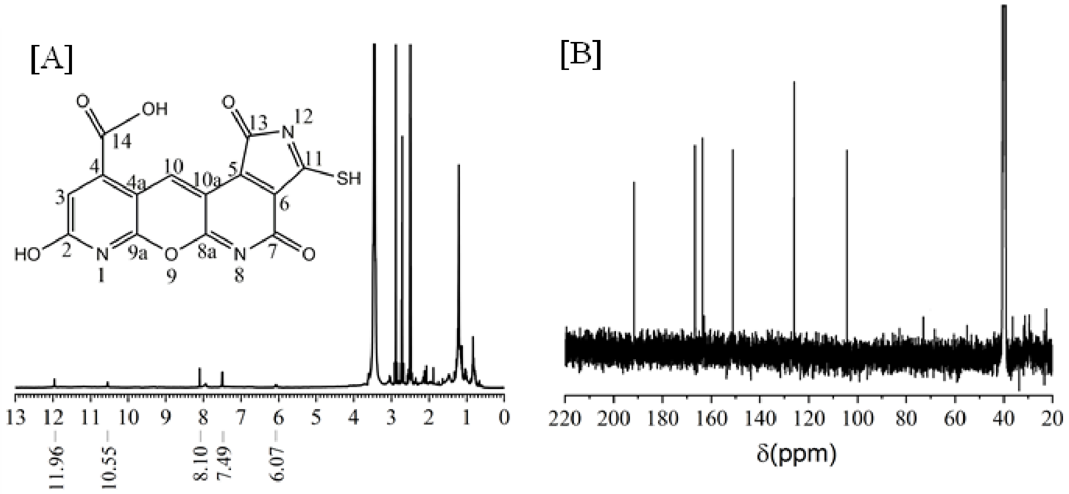

Figure A3.3: [A]^{1}H NMR spectrum and [B] ^{13}C NMR spectrum of the product, (P^R) in DMSO-d_6 solvent

^{13}C NMR (DMSO-d_6, 400MHz): δ 191.65 (C-11), 166.65 (C-7, C-13, C-14), 163.56 (C-5, C-8a), 151.07 (C-2, C-6, C-9a), 126.04 (C-4, C-10a), 104.36 (C-3, C-4, C-10a)

^{1}H NMR (DMSO-d_6, 400MHz): δ 11.96 (s, C2-O<u>H</u>), 10.55 (s, C14-COO<u>H</u>), 8.10 (N1-<u>H</u> / N12-<u>H</u>), 7.49 (s, C10-<u>H</u>), 6.07 (s, C3-<u>H</u>)

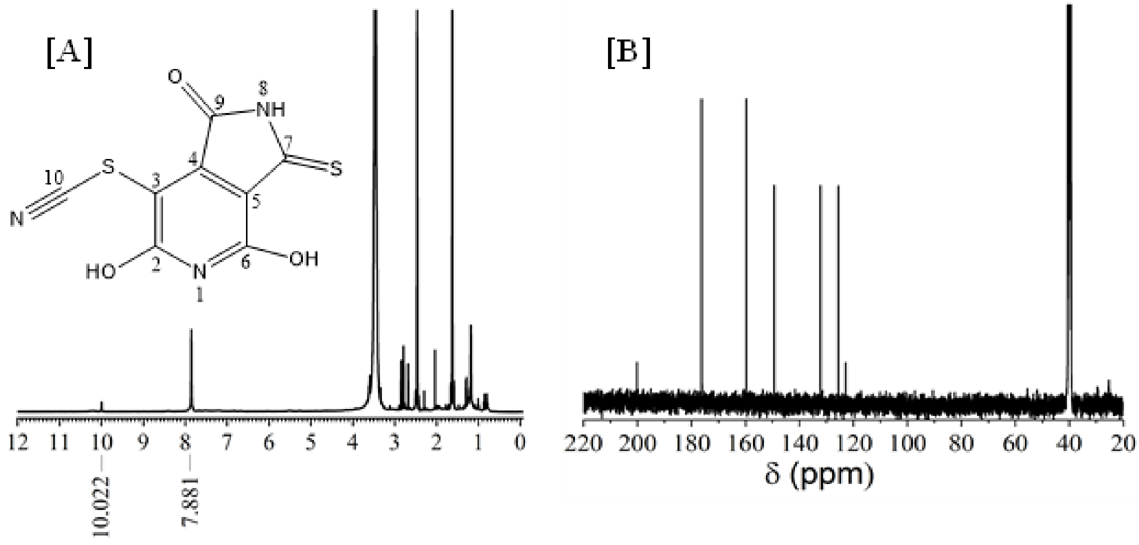

Figure A3.4: **[A]**^{1}H NMR spectrum and **[B]**^{13}C NMR spectrum of the green product, (P^{G}) in DMSO-d_6 solvent.

^{13}C NMR (DMSO-d_6, 400MHz): δ 200.12 (C-7), 176.21(C-9), 159.66 (C-6), 149.29 (C-2), 132.17 (C-3, C-4), 125.54 (C-10)

^{1}H NMR (DMSO-d_6, 400MHz): δ 10.02 (C2-O<u>H</u>, C6-O<u>H</u>), 7.88 (N-<u>H</u>)

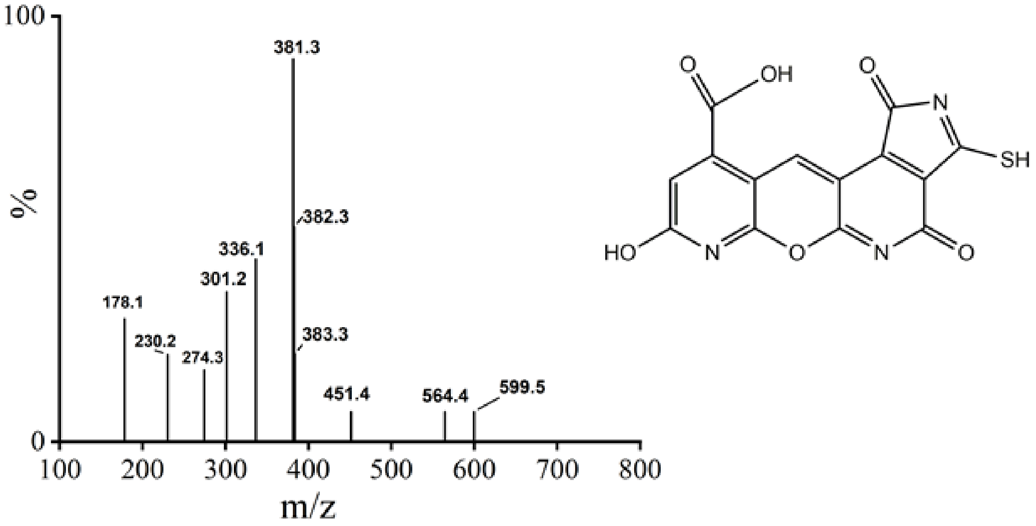

Figure A3.5: Mass spectrum of the synthesized product, (P^{R}). Predicted m/z ($C_{14}H_5N_3O_6S.K^+$) is 382.37 and found is 382.33

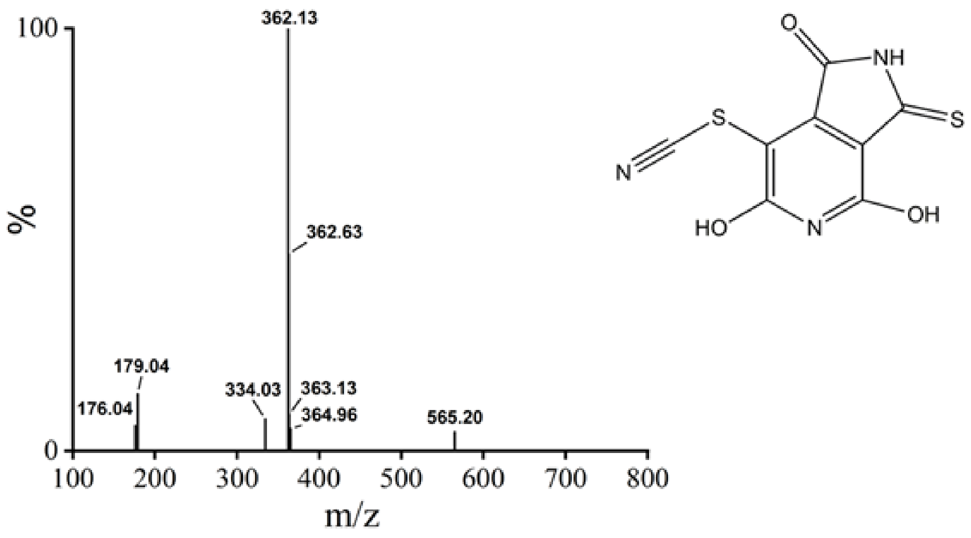

Figure A3.6: Mass spectrum of the synthesized product, (P^G). Predicted m/z ($C_8H_3N_3O_3S_2$. $4H_2O.K^+$) is 362.97 and found is 363.13

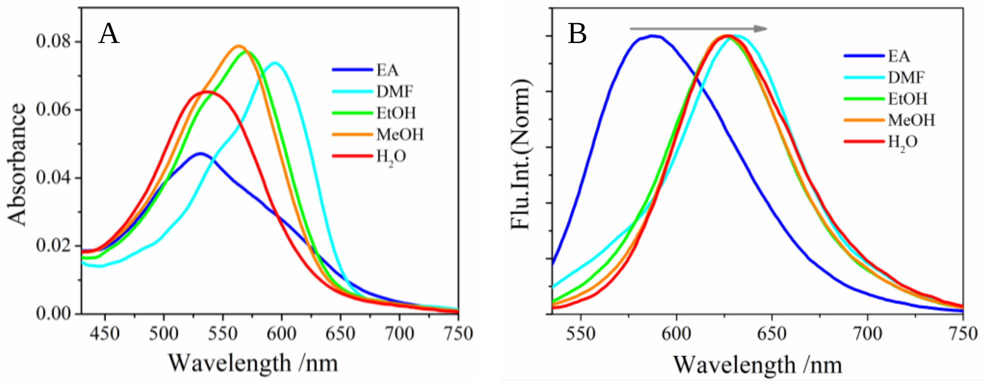

Figure A3.7: A). Absorbance spectra and B). Normalised emission spectra at 520 nm in different solvents of the P^R product.

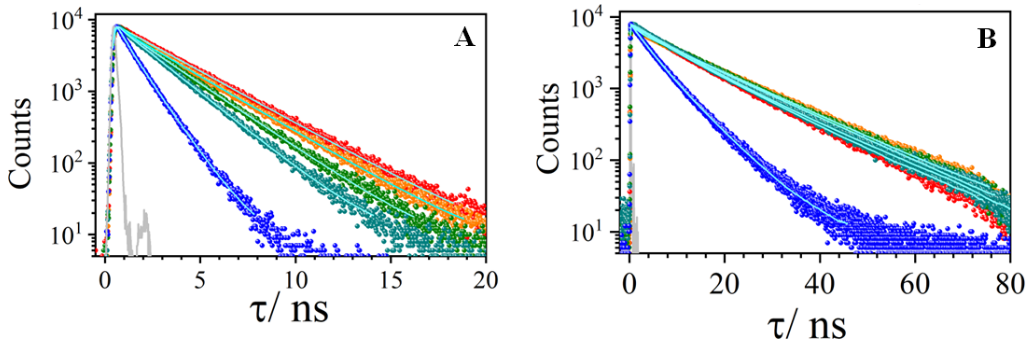

Figure A3.8: A). Fluorescence decay trace at a 620 nm emission wavelength, with λ_{exc}=510 nm of the P^R product. B). Fluorescence decay trace at a 520 nm emission wavelength, with λ_{exc}=405 nm of the P^G product in above same solvent.

Table A3.2: Lowest Vertical Excitations Computed at the ZINDO// B3LYP/ 6-311++G(d,p) scrf=(iefpcm, solvent=methanol) level and TD// B3LYP/ 6-311++G(d,p) scrf=(iefpcm, solvent=methanol) for the synthesized Red and Green CND in Methanol as Solvent.

Product	**Method**	**Energy**	**Oscillator Strength**	**ψ_o - ψ_v ^{a,b}**
Red (P^R)	TD	2.5877 eV (479.13 nm)	0.3685	HOMO -> LUMO (0.68175) HOMO-1 -> LUMO (0.10455)
	ZINDO	2.5686 eV (482.69 nm)	0.7457	HOMO -> LUMO (0.67173) HOMO-1 -> LUMO+1 (0.13165)
Green (P^G)	TD	3.1244 eV (396.82 nm)	0.2438	HOMO -> LUMO (0.66314) HOMO-1 -> LUMO (0.21392)
	ZINDO	3.2648 eV (379.76 nm)	0.477	HOMO -> LUMO (0.67108) HOMO-2 -> LUMO (0.11668)
Experimental Observation				
	Abs. Peak (max.)	**Solvent**		
Red (P^R)	564 nm	Methanol		
Green (P^G)	411 nm	Methanol		

Table A3.3: Fluorescence decay parameters of the synthesized fluorescent probe, Red (P^R) interaction with different conc. of CTAB surfactant. The excitation and emission wavelengths are- λ_{exc} = 510 nm, λ_{ems} = 620 nm.

[CTAB]/mM	τ_1 /ns	τ_2 /ns	a_1	a_2	$<\tau>$ /ns	χ^2	ϕ_f
0	0.58	1.20	0.54	0.46	0.98	1.12	0.06
0.5	0.62	1.46	0.75	0.25	0.99	1.01	0.04
1	0.65	2.26	0.51	0.49	1.90	1.19	0.09
2	0.70	2.35	0.37	0.63	2.10	1.19	0.13
4	0.77	2.37	0.33	0.67	2.15	1.19	0.14
7	0.77	2.36	0.31	0.69	2.15	1.07	0.13

Table A.3.4: Fluorescence decay parameters of synthesized fluorescent product P^G, interaction with various conc. of [CTAB] in aqueous medium. The excitation and emission wavelengths are- λ_{exc} = 405 nm, λ_{ems} = 520 nm.

[CTAB]/mM	τ_1 /ns	τ_2 /ns	a_1	a_2	$<\tau>$ /ns	χ^2	ϕ_f
0	2.85	5.66	0.49	0.51	4.74	1.17	0.09
0.5	3.19	6.99	0.61	0.39	5.40	1.06	0.13
0.75	3.43	9.43	0.51	0.49	7.78	1.13	0.15
1	3.12	9.85	0.32	0.68	8.98	1.12	0.21
1.5	2.51	9.78	0.23	0.77	9.26	1.18	0.24
3	2.21	9.70	0.20	0.80	9.30	1.10	0.24
4	2.04	9.64	0.20	0.80	9.26	1.14	0.24

Table A3.5: Fluorescence decay parameters of synthesized fluorescent probe, Red to Green Dots in various solvents. The excitation and emission wavelengths are- λ_{exc} = 405 nm, λ_{ems} = 520 nm.

Product	Solvents	τ_1 /ns (a_1)	τ_2 /ns (a_2)	τ_3 /ns (a_3)	$<\tau>$ /ns	χ^2	ϕ_f
Switched Green ($P^{R\rightarrow G^*}$)	MeOH	4.55 (0.36)	12.92 (0.40)	0.92 (0.24)	10.90	1.00	0.29
Green-emissive Product.(P^G)	MeOH	6.81 (0.26)	13.66 (0.74)	-	12.64	1.05	0.40

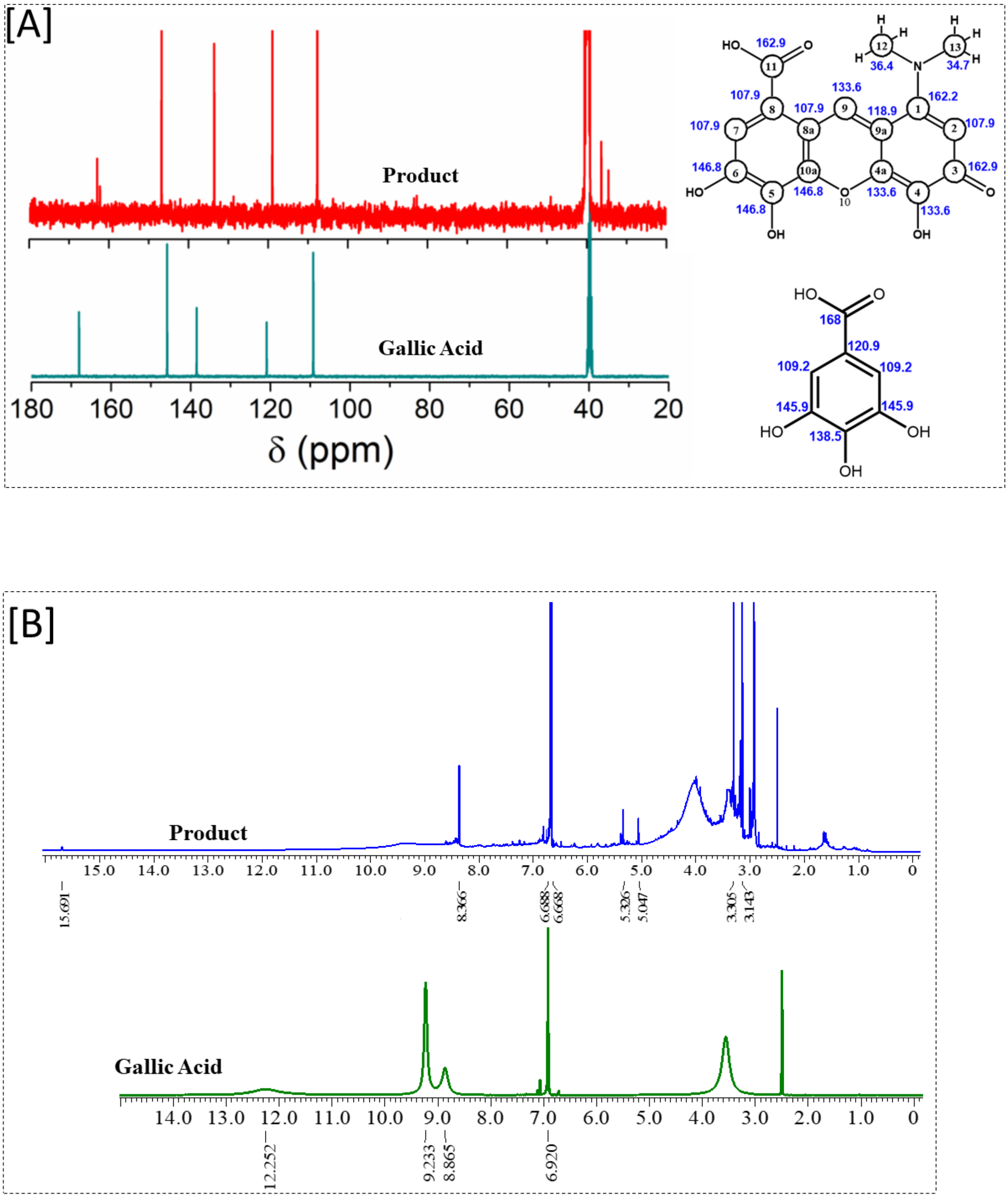

Figure-A4.1: [A] ^{13}C NMR spectrum, and **[B]** ^{1}H NMR spectrum of product (P) in DMSO-d_6 solvent

^{13}C NMR (DMSO-d_6, 400 MHz): δ 162.95 (C-11, C-3) 162.23 (C-1), 146.78 (C-6, C-5, C-10a), 133.54 (C-4, C-4a, C-9), 118.96 (C-9a), 107.86 (C-8a, C-8, C-7, C-2), 36.36 (C-12) 34.66 (C-13). ^{1}H NMR (DMSO-d_6, 400 MHz): δ 15.69 (s, C11-OH), 8.36 (s, C4-OH), 6.68 (d, J= 7.39 7.78, C6-OH, C5-OH), 5.32 (s, C9-H), 5.04 (s, C2-H, C7-H), 3.30 (s, 3H, C12-H), 3.14 (s, 3H, C13-H)

Table- A4.1: Lowest Vertical Excitations Computed at the ZINDO// B3LYP/ 6-311++G(d,p) level for the synthesized product (P)

Charge	**Energy**	**Oscillator Strength**	**ψo - ψ_v [a,b]**
Neutral	2.6605 eV (**466.02** nm)	0.5325	HOMO → LUMO (0.65) HOMO-1 → LUMO (0.20)
Protonated (Cationic)	2.3388 eV (**530.11** nm)	0.5992	HOMO → LUMO (0.68) HOMO-1 → LUMO (0.10)
Experimental Observation			
	Abs. Peak (max.)	**Solvent**	
Product, P	**440 nm**	Ethyl Acetate	
Product, P in acidic condition	**632 nm**	Acidic	

[a] Occupied and virtual orbitals. [b] Transition coefficient in parentheses.
The transitions with zero oscillator strength has been omitted.

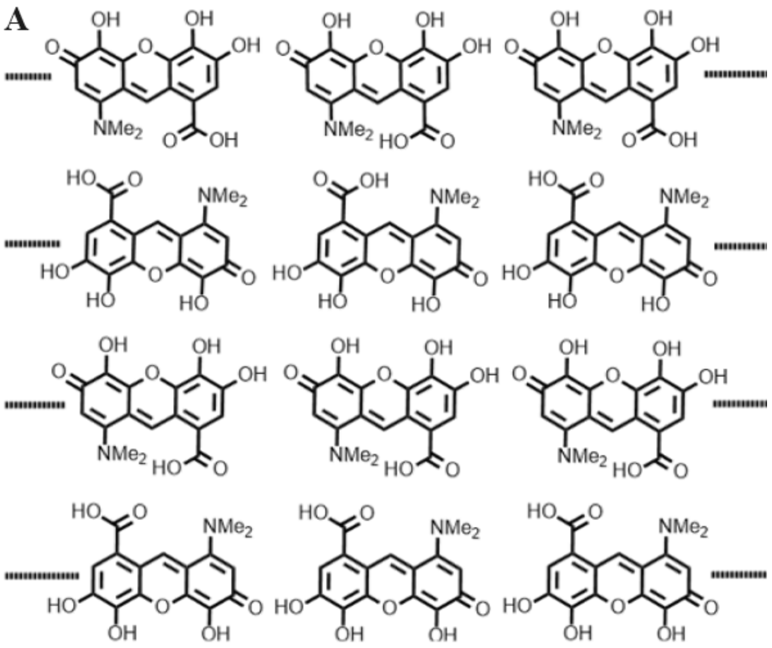

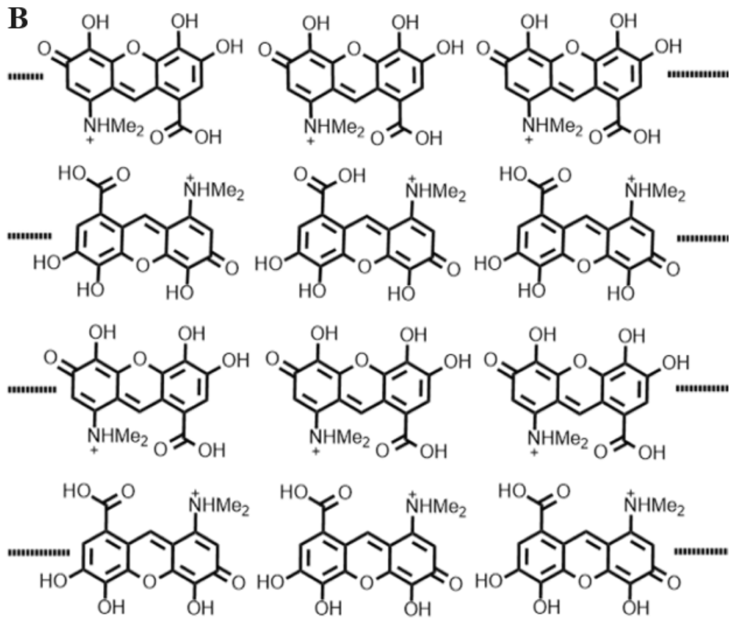

Figure- A4.2: Proposed schematic representation of H-bonded molecular arrangement of Product, P molecules in absence of solvent. **(A)** without an acidic environment, **(B)** In an acidic environment

Table A4.2: Fluorescence decay parameters of synthesized fluorescent probe, P measured at different emission wavelengths. The excitation wavelength is kept at λ_{exc} = 405 nm

	λ_{ems} (nm)	τ_1 /ns	τ_2 /ns	τ_3 /ns	a_1	a_2	a_3	<τ> /ns	χ^2
Ethyl acetate	460	1.14	3.96	0.25	0.20	0.06	0.74	2.58	1.14
	480	0.37	2.37	0	0.70	0.30	0	1.83	1.12
	490	0.39	2.34	0	0.62	0.38	0	1.92	1.00
	500	0.42	2.33	0	0.50	0.50	0	2.04	1.02
	520	0.67	2.36	0	0.25	0.75	0	2.21	0.99
	540	2.28	0	0	1.00	0	0	2.28	1.01
	550	2.27	1.15	0	0.97	-0.03		2.29	1.09
	560	2.11	2.89	0.22	0.64	0.18	-0.19	2.32	0.99
	580	2.21	3.68	0.25	0.73	0.05	-0.22	2.36	0.99
	600	2.25	4.23	0.29	0.76	0.03	-0.21	2.39	0.99
	620	2.06	3.22	0.36	0.62	0.17	-0.21	2.41	1.02

Luminescence lifetimes, = $\Sigma a_i \tau_i^2 / \Sigma a_i \tau_i$

Table A4.3: Time-resolved emission properties of proton-triggered AIE in water. The excitation wavelength, λ_{exc} = 510 nm

λ_{ems} (nm)	τ_1 /ns	τ_2 /ns	a_1	a_2	$<\tau>$ /ns	χ^2
640	1.041	-	1.00	-	1.041	1.13
650	1.031	-	1.00	-	1.031	1.12
660	1.029	-	1.00	-	1.029	1.06
680	1.022	-	1.00	-	1.022	1.07

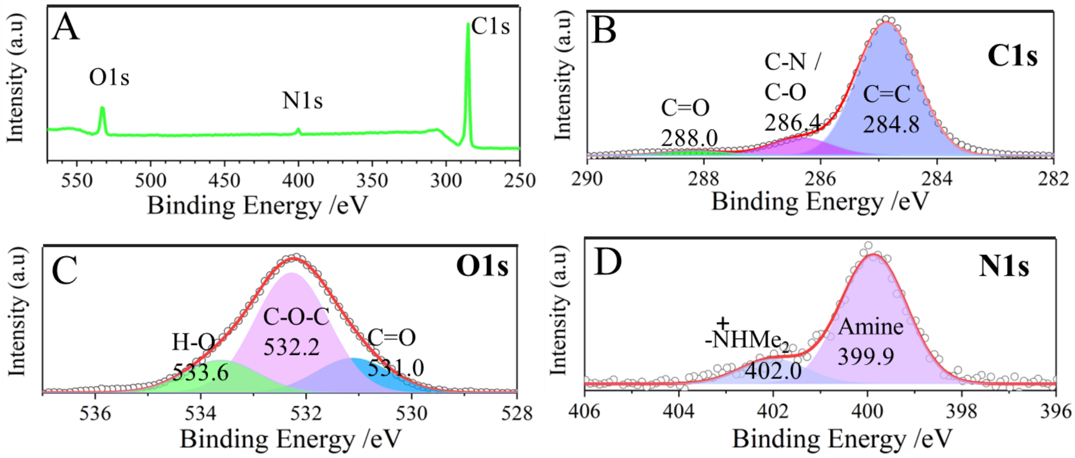

Figure A5.1: [A] Full survey XPS spectra of product (green line). High-resolution XPS of **[B]** the C 1s core level, **[C]** the O 1s core level, and **[D]** the N 1s core level of product. Fitted lines are in solid red color, experimental data are in hollow circles, and individual components are presented in colored areas for clarity.

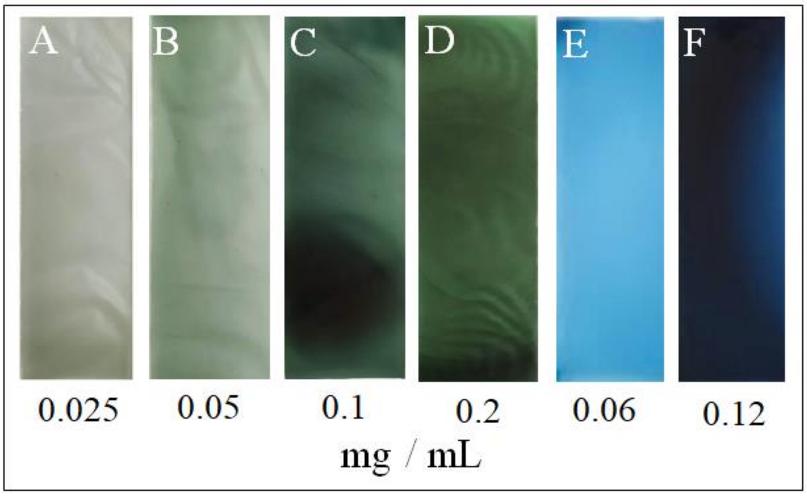

Figure A5.3: [A-D] 1% PVDF films and **[E, F]** 2% PVA-PVP films of product, SA^R with different concentrations of product, SA^R.

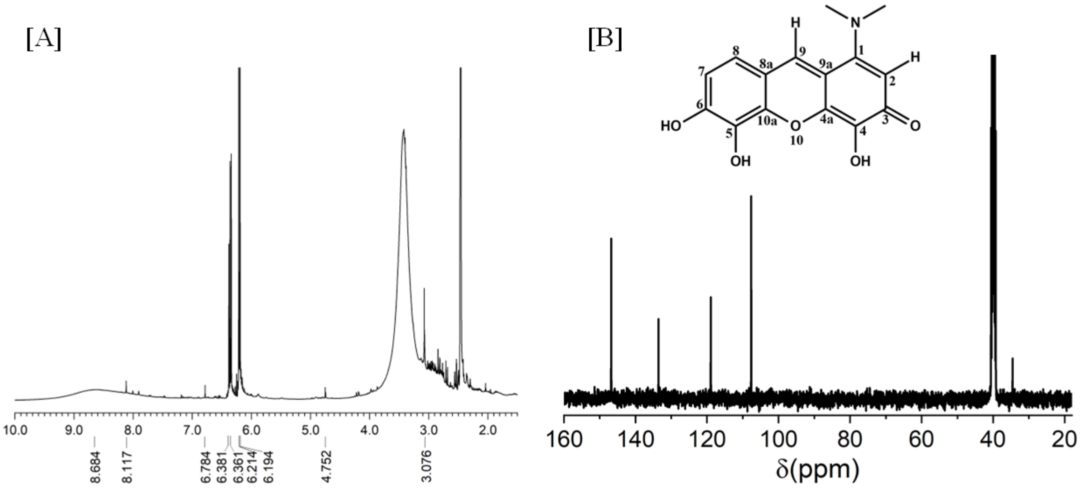

Figure A5.2: NMR spectra of the yellow emissive product, P^Y in DMSO-d_6 solvent.**[A]** ^{1}H-NMR (JEOL, 400 MHz): δ 8.684 (s, C4-O<u>H</u>), δ 8.117 (s, C6/C5-O<u>H</u>), δ 6.784 (s, C9-<u>H</u>), δ 6.381, 6.361, (d, J=8, C8-<u>H</u>), 6.214, 6.194 (d, J=8, C7-<u>H</u>), δ 4.752 (s, C2-<u>H</u>), δ 3.076 (s,-C<u>H</u>3)

[B] ^{13}C-NMR spectra (JEOL 400MHz) : δ 146.78 (C1, C3, C4, C6, C10a), δ 133.56 (C5, C4a, C9a), δ 118.93 (C8), δ 107.64 (C2, C7,C8a, C9), δ 34.48 (-<u>C</u>H3)

Table A5.1: Fluorescence decay parameters of the yellow emissive products, P^Y at different concentrations of the surfactant, SDS. The excitation and emission wavelength are λ_{exc}=405nm and λ_{ems}=440 nm

[SDS]/mM	τ_1 /ns	τ_2 /ns	a_1	a_2	<τ>/ns	χ^2	ϕ_f
0	0.27	2.37	0.14	0.86	2.33	1.06	0.28
5	0.64	2.66	0.19	0.81	2.55	1.06	0.30
10	0.67	3.11	0.18	0.82	3.00	1.02	0.36
15	0.53	3.20	0.16	0.84	3.12	1.02	0.37
20	0.47	3.27	0.17	0.83	3.18	1.01	0.39
30	0.45	3.32	0.16	0.84	3.24	0.99	0.40

References:

(1) Michalet, X.; Pinaud, F. F.; Bentolila, L. A.; Tsay, J. M.; Doose, S.; Li, J. J.; Sundaresan, G.; Wu, A. M.; Gambhir, S. S.; Weiss, S. Quantum Dots for Live Cells, in Vivo Imaging, and Diagnostics. *Science.* **2005**, *307*, 538–544.

(2) Derfus, A. M.; Chan, W. C. W.; Bhatia, S. N. Probing the Cytotoxicity of Semiconductor Quantum Dots. *Nano Lett.* **2004**, *4*, 11–18.

(3) Kirchner, C.; Liedl, T.; Kudera, S.; Pellegrino, T.; Javier, A. M.; Gaub, H. E.; Stölzle, S.; Fertig, N.; Parak, W. J. Cytotoxicity of Colloidal CdSe and CdSe/ZnS Nanoparticles. *Nano Lett.* **2005**, *5*, 331–338.

(4) Lovrić, J.; Cho, S. J.; Winnik, F. M.; Maysinger, D. Unmodified Cadmium Telluride Quantum Dots Induce Reactive Oxygen Species Formation Leading to Multiple Organelle Damage and Cell Death. *Chem. Biol.* **2005**, *12*, 1227–1234.

(5) Bharali, D. J.; Lucey, D. W.; Jayakumar, H.; Pudavar, H. E.; Prasad, P. N. Folate-Receptor-Mediated Delivery of InP Quantum Dots for Bioimaging Using Confocal and Two-Photon Microscopy. *J. Am. Chem. Soc.* **2005**, *127*, 11364–11371.

(6) Wilson, W. L.; Szajowski, P. F.; Brus, L. E. Quantum Confinement in Size-Selected, Surface-Oxidized Silicon Nanocrystals. *Science.* **1993**, *262*, 1242–1244.

(7) Sun, Y. P.; Zhou, B.; Lin, Y.; Wang, W.; Fernando, K. A. S.; Pathak, P.; Meziani, M. J.; Harruff, B. A.; Wang, X.; Wang, H.; Luo, P. G.; Yang, H.; Kose, M. E.; Chen, B.; Veca, L. M.; Xie, S. Y. Quantum-Sized Carbon Dots for Bright and Colorful Photoluminescence. *J. Am. Chem. Soc.* **2006**, *128*, 7756–7757.

(8) Xiaoyou Xu, †; Robert Ray, †; Yunlong Gu, †; Harry J. Ploehn, †; Latha Gearheart, ‡; Kyle Raker, † and; Walter A. Scrivens*, †. Electrophoretic Analysis and Purification of Fluorescent Single-Walled Carbon Nanotube Fragments. *J. Am. Chem. Soc.* **2004**, *126*, 12736–12737.

(9) Liu, J.; Li, R.; Yang, B. Carbon Dots: A New Type of Carbon-Based Nanomaterial with Wide Applications. *ACS Cent. Sci.* **2020**, *6*, 2179–2195.

(10) Yang, Z.; Xu, T.; Li, H.; She, M.; Chen, J.; Wang, Z.; Zhang, S.; Li, J. Zero-Dimensional Carbon Nanomaterials for Fluorescent Sensing and Imaging. *Chem. Rev.* **2023**, *123*, 11047–11136.

(11) Ding, H.; Zhou, X.; Wei, J.; Li, X.; Qin, B.; Chen, X.; Xiong, H. Carbon Dots with Red/near-Infrared Emissions and Their Intrinsic Merits for Biomedical Applications. *Carbon N. Y.* **2020**, 332-344

(12) Hong, G.; Diao, S.; Antaris, A. L.; Dai, H. Carbon Nanomaterials for Biological Imaging and Nanomedicinal Therapy. *Chem. Rev.* **2015**, *115*, 10816–10906.

(13) Mocci, F.; Engelbrecht, L. D. V.; Olla, C.; Cappai, A.; Casula, M. F.; Melis, C.; Stagi, L.; Laaksonen, A.; Carbonaro, C. M. Carbon Nanodots from an In Silico Perspective. *Chem. Rev.* **2022**, *122*, 13709–13799.

(14) Jeong, J.; Cho, M.; Lim, Y. T.; Song, N. W.; Chung, B. H. Synthesis and Characterization of a Photoluminescent Nanoparticle Based on Fullerene-Silica Hybridization. *Angew. Chemie - Int. Ed.* **2009**, *48*, 5296–5299.

(15) Baker, S. N.; Baker, G. A. Luminescent Carbon Nanodots: Emergent Nanolights. *Angew. Chemie - Int. Ed.* **2010**, *49*, 6726–6744.

(16) Zheng, H.; Wang, Q.; Long, Y.; Zhang, H.; Huang, X.; Zhu, R. Enhancing the Luminescence of Carbon Dots with a Reduction Pathway. *Chem. Commun.* **2011**, *47*, 10650–10652.

(17) Zhu, S.; Meng, Q.; Wang, L.; Zhang, J.; Song, Y.; Jin, H.; Zhang, K.; Sun, H.; Wang, H.; Yang, B. Highly Photoluminescent Carbon Dots for Multicolor Patterning, Sensors, and Bioimaging. *Angew. Chemie - Int. Ed.* **2013**, *52*, 3953–3957.

(18) Wang, L.; Zhu, S. J.; Wang, H. Y.; Qu, S. N.; Zhang, Y. L.; Zhang, J. H.; Chen, Q. D.; Xu, H. L.; Han, W.; Yang, B.; Sun, H. B. Common Origin of Green Luminescence in Carbon Nanodots and Graphene Quantum Dots. *ACS Nano* **2014**, *8*, 2541–2547.

(19) Fu, M.; Ehrat, F.; Wang, Y.; Milowska, K. Z.; Reckmeier, C.; Rogach, A. L.; Stolarczyk, J. K.; Urban, A. S.; Feldmann, J. Carbon Dots: A Unique Fluorescent Cocktail of Polycyclic Aromatic Hydrocarbons. *Nano Lett.* **2015**, *15*, 6030–6035.

(20) Holá, K.; Sudolská, M.; Kalytchuk, S.; Nachtigallová, D.; Rogach, A. L.; Otyepka, M.; Zbořil, R. Graphitic Nitrogen Triggers Red Fluorescence in Carbon Dots. *ACS Nano* **2017**, *11*, 12402–12410.

(21) Tian, Z.; Zhang, X.; Li, D.; Zhou, D.; Jing, P.; Shen, D.; Qu, S.; Zboril, R.; Rogach, A. L. Full-Color Inorganic Carbon Dot Phosphors for White-Light-Emitting Diodes. *Adv. Opt. Mater.* **2017**, *5*, 1–9.

(22) Wang, Z.; Yuan, F.; Li, X.; Li, Y.; Zhong, H.; Fan, L.; Yang, S. 53% Efficient Red Emissive Carbon Quantum Dots for High Color Rendering and Stable Warm White-Light-Emitting Diodes. *Adv. Mater.* **2017**, *29*, 1–7.

(23) Tepliakov, N. V.; Kundelev, E. V.; Khavlyuk, P. D.; Xiong, Y.; Leonov, M. Y.; Zhu, W.; Baranov, A. V.; Fedorov, A. V.; Rogach, A. L.; Rukhlenko, I. D. Sp2-Sp3-Hybridized Atomic Domains Determine Optical Features of Carbon Dots. *ACS Nano* **2019**, *13*, 10737–10744.

(24) Kundelev, E. V.; Tepliakov, N. V.; Leonov, M. Y.; Maslov, V. G.; Baranov, A. V.; Fedorov, A. V.; Rukhlenko, I. D.; Rogach, A. L. Toward Bright Red-Emissive Carbon Dots through Controlling Interaction among Surface Emission Centers. *J. Phys. Chem. Lett.* **2020**, *11*, 8121–8127.

(25) Soni, N.; Singh, S.; Sharma, S.; Batra, G.; Kaushik, K.; Rao, C.; Verma, N. C.; Mondal, B.; Yadav, A.; Nandi, C. K. Absorption and Emission of Light in Red Emissive Carbon Nanodots. *Chem. Sci.* **2021**, *12*, 3615–3626.

(26) Dong, Y.; Pang, H.; Yang, H. Bin; Guo, C.; Shao, J.; Chi, Y.; Li, C. M.; Yu, T. Carbon-Based Dots Co-Doped with Nitrogen and Sulfur for High Quantum Yield and Excitation-Independent Emission. *Angew. Chemie - Int. Ed.* **2013**, *52*, 7800–7804.

(27) Wang, H.; Sun, C.; Chen, X.; Zhang, Y.; Colvin, V. L.; Rice, Q.; Seo, J.; Feng, S.; Wang, S.; Yu, W. W. Excitation Wavelength Independent Visible Color Emission of Carbon Dots. *Nanoscale* **2017**, *9*, 1909–1915.

(28) Nema, A.; Pareek, R.; Rai, T.; Panda, D. The Role of Glutathione and Ethanol in Dictating the Emission Dynamics of Natural Resources-Derived Highly Luminescent Carbon Nanodots. *ChemistrySelect* **2017**, *2*, 11255–11264.

(29) Nandy, A.; Kumar, A.; Dwivedi, S.; Pal, S. K.; Panda, D. Connecting the Dots of Carbon Nanodots: Excitation (In)Dependency and White-Light Emission in One-Step. *J. Phys. Chem. C* **2019**, *123*, 20502–20511.

(30) Otyepka, M.; Zbor, R. Graphitic Nitrogen Triggers Red Fluorescence in Carbon Dots. *ACS Nano* **2017**, *11, 12402-12410.*

(31) Arcudi, F.; Ďorďević, L.; Prato, M. Design, Synthesis, and Functionalization Strategies of Tailored Carbon Nanodots. *Acc. Chem. Res.* **2019**, *52*, 2070–2079.

(32) Panwar, N.; Soehartono, A. M.; Chan, K. K.; Zeng, S.; Xu, G.; Qu, J.; Coquet, P.; Yong, K. T.; Chen, X. Nanocarbons for Biology and Medicine: Sensing, Imaging, and Drug Delivery. *Chem. Rev.* **2019**, *119*, 9559–9656.

(33) Wang, Y.; Hu, A. Carbon Quantum Dots: Synthesis, Properties and Applications. *J. Mater. Chem. C* **2014**, *2*, 6921–6939.

(34) Biazar, N.; Poursalehi, R.; Delavari, H. Optical and Structural Properties of Carbon Dots/TiO2 Nanostructures Prepared via DC Arc Discharge in Liquid. *AIP Conf. Proc.* **2018**, 1–5.

(35) Ozyurt, D.; Kobaisi, M. Al; Hocking, R. K.; Fox, B. Properties, Synthesis, and Applications of Carbon Dots: A Review. *Carbon Trends* **2023**, 100276.

(36) Dey, S.; Govindaraj, A.; Biswas, K.; Rao, C. N. R. Luminescence Properties of Boron and Nitrogen Doped Graphene Quantum Dots Prepared from Arc-Discharge-Generated Doped Graphene Samples. *Chem. Phys. Lett.* **2014**, *595–596*, 203–208.

(37) Hu, S.; Liu, J.; Yang, J. Laser Synthesis and Size Tailor of Carbon Quantum Dots. **2011**, 7247–7252.

(38) Sun, Y.; Wang, X.; Lu, F.; Cao, L.; Meziani, M. J.; Luo, P. G.; Gu, L.; Veca, L. M. Doped Carbon Nanoparticles as a New Platform for Highly Photoluminescent Dots. **2008**, 18295–18298.

(39) Hu, S.; Niu, K.; Sun, J.; Yang, J.; Zhao, N.; Du, X. One-Step Synthesis of Fluorescent Carbon Nanoparticles by Laser Irradiation †. **2009**, 484–488.

(40) Liu, H.; Ye, T.; Mao, C. Fluorescent Carbon Nanoparticles Derived from Candle Soot. *Angew. Chemie - Int. Ed.* **2007**, *46*, 6473–6475.

(41) Zhou, J.; Booker, C.; Li, R.; Zhou, X.; Sham, T. K.; Sun, X.; Ding, Z. An Electrochemical Avenue to Blue Luminescent Nanocrystals from Multiwalled Carbon Nanotubes (MWCNTs). *J. Am. Chem. Soc.* **2007**, *129*, 744–745.

(42) Lu, J.; Yang, J. X.; Wang, J.; Lim, A.; Wang, S.; Loh, K. P. One-Pot Synthesis of Fluorescent Carbon Nanoribbons, Nanoparticles, and Graphene by the Exfoliation of Graphite in Ionic Liquids. *ACS Nano* **2009**, *3*, 2367–2375.

(43) Li, H.; He, X.; Kang, Z.; Huang, H.; Liu, Y.; Liu, J.; Lian, S.; Tsang, C. H. A.; Yang, X.; Lee, S. T. Water-Soluble Fluorescent Carbon Quantum Dots and Photocatalyst Design. *Angew. Chemie - Int. Ed.* **2010**, *49*, 4430–4434.

(44) Qi, B. P.; Bao, L.; Zhang, Z. L.; Pang, D. W. Electrochemical Methods to Study Photoluminescent Carbon Nanodots: Preparation, Photoluminescence Mechanism and Sensing. *ACS Appl. Mater. Interfaces* **2016**, *8*, 28372–28382.

(45) Online, V. A.; Song, Y.; Zhu, S.; Zhang, S.; Fu, Y.; Wang, L.; Zhao, X.; Yang, B. Investigation from Chemical Structure to Photoluminescent Mechanism : A Type of Carbon Dots from the Pyrolysis of Citric Acid and Amine. *J. Mater. Chem. C*, **2015**,3, 5976-5984.

(46) Ghosh, S.; Ghosh, A.; Ghosh, G.; Marjit, K.; Patra, A. Deciphering the Relaxation Mechanism of Red-Emitting Carbon Dots Using Ultrafast Spectroscopy and Global Target Analysis. *J. Phys. Chem. Lett.* **2021**, *12*, 8080–8087.

(47) Tang, L.; Ji, R.; Cao, X.; Lin, J.; Jiang, H.; Li, X.; Teng, K. S. Deep Ultraviolet Photoluminescence of Water-Soluble Self-Passivated Graphene Quantum Dots.

2012, No. 6, 5102–5110.

(48) Zhu, H.; Wang, X.; Li, Y.; Wang, Z.; Yang, F.; Yang, X. Microwave Synthesis of Fluorescent Carbon Nanoparticles with Electrochemiluminescence Properties. *Chem. Commun.* **2009**, 5118–5120.

(49) Zhai, X.; Zhang, P.; Liu, C.; Bai, T.; Li, W.; Dai, L. Electronic Supplementary Information Highly Luminescent Carbon Nanodots by Microwave-Assisted Pyrolysis. *Chem. Commun.* **2012**, 1–15.

(50) Zhang, Y.; Liu, X.; Fan, Y.; Guo, X.; Zhou, L.; Lv, Y.; Lin, J. One-Step Microwave Synthesis of N-Doped Hydroxyl-Functionalized Carbon Dots with Ultra-High Fluorescence Quantum Yields. *Nanoscale*. 2016, 15281–15287.

(51) Zhang, D.; Chao, D.; Yu, C.; Zhu, Q.; Zhou, S.; Tian, L.; Zhou, L. One-Step Green Solvothermal Synthesis of Full-Color Carbon Quantum Dots Based on a Doping Strategy. *J. Phys. Chem. Lett.* **2021**, *12*, 8939–8946.

(52) Hsu, P. C.; Chang, H. T. Synthesis of High-Quality Carbon Nanodots from Hydrophilic Compounds: Role of Functional Groups. *Chem. Commun.* **2012**, *48*, 3984–3986.

(53) Yang, Y.; Cui, J.; Zheng, M.; Hu, C.; Tan, S.; Xiao, Y.; Yang, Q.; Liu, Y. One-Step Synthesis of Amino-Functionalized Fluorescent Carbon Nanoparticles by Hydrothermal Carbonization of Chitosan. *Chem. Commun.* **2012**, *48*, 380–382.

(54) Sahu, S.; Behera, B.; Maiti, T. K.; Mohapatra, S. Simple One-Step Synthesis of Highly Luminescent Carbon Dots from Orange Juice: Application as Excellent Bio-Imaging Agents. *Chem. Commun.* **2012**, *48*, 8835–8837.

(55) Bhunia, S. K.; Saha, A.; Maity, A. R.; Ray, S. C.; Jana, N. R. Carbon Nanoparticle-Based Fluorescent Bioimaging Probes. *Sci. Rep.* **2013**, *3*.

(56) Yang, Z. C.; Wang, M.; Yong, A. M.; Wong, S. Y.; Zhang, X. H.; Tan, H.; Chang, A. Y.; Li, X.; Wang, J. Intrinsically Fluorescent Carbon Dots with Tunable Emission Derived from Hydrothermal Treatment of Glucose in the Presence of Monopotassium Phosphate. *Chem. Commun.* **2011**, *47*, 11615–11617.

(57) Bourlinos, A. B.; Stassinopoulos, A.; Anglos, D.; Zboril, R.; Karakassides, M.; Giannelis, E. P. Surface Functionalized Carbogenic Quantum Dots. *Small* **2008**, *4*, 455–458.

(58) Krysmann, M. J.; Kelarakis, A.; Dallas, P.; Giannelis, E. P. Formation Mechanism of Carbogenic Nanoparticles with Dual Photoluminescence Emission. **2012**, *1*, 1–4.

(59) Chem, J. M. Facile Synthesis of Highly Emissive Carbon Dots from Pyrolysis of Glycerol ; Gram Scale Production of Carbon Dots / MSiO$_2$ for Cell Imaging and Drug. **2012**, 14403–14409..

(60) Kumar, V. B.; Tang, J.; Lee, K. J.; Pol, V. G.; Gedanken, A. In Situ Sonochemical Synthesis of Luminescent Sn@C-Dots and a Hybrid Sn@C-Dots@Sn Anode for Lithium-Ion Batteries. *RSC Adv.* **2016**, *6*, 66256–66265.

(61) Li, H.; He, X.; Liu, Y.; Kang, Z. One-Step Ultrasonic Synthesis of Water-Soluble Carbon Nanoparticles with Excellent Photoluminescent Properties. *Carbon N. Y.* **2010**, *49*, 605–609.

(62) Li, H.; Liu, R.; Liu, Y.; Huang, H.; Yu, H.; Ming, H.; Lian, S.; Lee, S. T.; Kang, Z. Carbon Quantum Dots/Cu$_2$O Composites with Protruding Nanostructures and Their Highly Efficient (near) Infrared Photocatalytic Behavior. *J. Mater. Chem.* **2012**, *22*, 17470–17475.

(63) Amali, A. J.; Hoshino, H.; Wu, C.; Ando, M.; Xu, Q. From Metal – Organic Framework to Intrinsically Fluorescent Carbon Nanodots. Chem. Eur. J**. 2014,**

20, 1–5.

(64) Xu, H.; Zhou, S.; Xiao, L.; Wang, H.; Li, S.; Yuan, Q. Fabrication of a Nitrogen-Doped Graphene Quantum Dot from MOF-Derived Porous Carbon and Its Application for Highly Selective Fluorescence Detection of Fe^{3+}. *J. Mater. Chem. C Mater. Opt. Electron. devices* **2014**, *00*, 1–7.

(65) Online, V. A. Bottom-up Fabrication of Photoluminescent Carbon Dots with Uniform Morphology via a Soft–Hard Template Approach. **2013**, 4920–4922.

(66) Gu, Z. G.; Li, D. J.; Zheng, C.; Kang, Y.; Wöll, C.; Zhang, J. MOF-Templated Synthesis of Ultrasmall Photoluminescent Carbon-Nanodot Arrays for Optical Applications. *Angew. Chemie - Int. Ed.* **2017**, *56*, 6853–6858.

(67) Xiao, Y.; Yang, X.; Li, D.; Gu, Z.; Zhang, J. Inducing Circularly Polarized Luminescence by Confined Synthesis of Ultrasmall Chiral Carbon Nanodot Arrays in Pyrene-Based MOF Thin Film. *ACS Nano* **2023**, 17, 19136–19143.

(68) Ding, H.; Yu, S. B.; Wei, J. S.; Xiong, H. M. Full-Color Light-Emitting Carbon Dots with a Surface-State-Controlled Luminescence Mechanism. *ACS Nano* **2016**, *10*, 484–491.

(69) Gong, X.; Li, Z.; Hu, Q.; Zhou, R.; Shuang, S.; Dong, C. N,S,P Co-Doped Carbon Nanodot Fabricated from Waste Microorganism and Its Application for Label-Free Recognition of Manganese(VII) and l -Ascorbic Acid and AND Logic Gate Operation. *ACS Appl. Mater. Interfaces* **2017**, *9* (44), 38761–38772.

(70) Chen, C.; Xu, Z.; Qiu, J.; Ye, W.; Xu, X.; Wang, R.; Hu, C.; Zhuang, J.; Lei, B.; Li, W.; Zhang, X.; Hu, G.; Liu, Y. Synthesis of Carbon Dots with Carbogenic π-Conjugated Domains for Full-Band UV Shielding. *ACS Appl. Nano Mater.* **2022**, *5*, 9140–9149.

(71) Kaleem, W.; Kumar, A.; Panda, D. Luminescent N, S-Doped Carbon Nanodot: An Effective Two-Fluorophore System of Pyridone and Thiazolopyridone. *J. Phys. Chem. C* **2018**, *122*, 26722–26732.

(72) Qu, S.; Zhou, D.; Li, D.; Ji, W.; Jing, P.; Han, D.; Liu, L. Toward Effi Cient Orange Emissive Carbon Nanodots through Conjugated sp^2 -Domain Controlling and Surface Charges Engineering. Adv. Mater. **2016**, 28, 3516–3521.

(73) Deng, Y.; Zhao, D.; Chen, X.; Wang, F.; Song, H.; Shen, D. Long Lifetime Pure Organic Phosphorescence Based on Water Soluble Carbon Dots. *Chem. Commun.* **2013**, *49*, 5751–5753.

(74) Wang, B.; Mu, Y.; Zhang, H.; Shi, H.; Chen, G.; Yu, Y.; Yang, Z.; Li, J.; Yu, J. Red Room-Temperature Phosphorescence of CDs@Zeolite Composites Triggered by Heteroatoms in Zeolite Frameworks. *ACS Cent. Sci.* **2019**, *5*, 349–356.

(75) Liang, Y. C.; Cao, Q.; Liu, K. K.; Peng, X. Y.; Sui, L. Z.; Wang, S. P.; Song, S. Y.; Wu, X. Y.; Zhao, W. B.; Deng, Y.; Lou, Q.; Dong, L.; Shan, C. X. Phosphorescent Carbon-Nanodots-Assisted Förster Resonant Energy Transfer for Achieving Red Afterglow in an Aqueous Solution. *ACS Nano* **2021**, *15*, 16242–16254.

(76) Cao, Q.; Liu, K. K.; Liang, Y. C.; Song, S. Y.; Deng, Y.; Mao, X.; Wang, Y.; Zhao, W. B.; Lou, Q.; Shan, C. X. Brighten Triplet Excitons of Carbon Nanodots for Multicolor Phosphorescence Films. *Nano Lett.* **2022**, *22*, 4097–4105.

(77) Mao, X.; Liu, K. K.; Cao, Q.; *et. al.* Paper-Fiber-Activated Triplet Excitons of Carbon Nanodots for Time-Resolved Anti-Counterfeiting Signature with

Artificial Intelligence Authentication. *ACS Appl. Mater. Interfaces* **2023**, *15*, 20302–20309.

(78) Göppert-Mayer, M. Über Elementarakte Mit Zwei Quantensprüngen. *Ann. Phys.* **1931**, *401* (3), 273–294.

(79) Diaspro, A.; Chirico, G. Two-Photon Excitation Microscopy. *Adv. Imaging Electron Phys.* **2003**, *126*, 399–429.

(80) Denk, W.; Strickler, J. H.; Webb, W. W. Two-Photon Laser Scanning Fluorescence Microscopy. **1990**, *248*, 73–76.

(81) Lesani, P.; Mohamad Hadi, A. H.; Lu, Z.; Palomba, S.; New, E. J.; Zreiqat, H. Design Principles and Biological Applications of Red-Emissive Two-Photon Carbon Dots. *Commun. Mater.* **2021**, *2* (1).

(82) Lili Wang, Jing Zheng, Sheng Yang‡, Cuichen Wu†, Changhui Liu†, Yue Xiao†, Yinhui Li†, Zhihe Qing‡, and R. Y. Two-Photon Sensing and Imaging of Endogenous Biological Cyanide in Plant Tissues Using Graphene Quantum Dot/Gold Nanoparticle Conjugate. **2015**, *7*, 19509–19515.

(83) Cao, L.; Wang, X.; Meziani, M. J.; Lu, F.; Wang, H.; Luo, P. G.; Lin, Y.; Harruff, B. A.; Veca, L. M.; Murray, D.; Xie, S. Y.; Sun, Y. P. Carbon Dots for Multiphoton Bioimaging. *J. Am. Chem. Soc.* **2007**, *129*, 11318–11319.

(84) Alam, A. M.; Park, B. Y.; Ghouri, Z. K.; Park, M.; Kim, H. Y. Synthesis of Carbon Quantum Dots from Cabbage with Down- and up-Conversion Photoluminescence Properties: Excellent Imaging Agent for Biomedical Applications. *Green Chem.* **2015**, *17*, 3791–3797.

(85) Ye, Z.; Lin, X.; Wang, N.; Zhou, J.; Zhu, M.; Qin, H.; Peng, X. Phonon-Assisted up-Conversion Photoluminescence of Quantum Dots. *Nat. Commun.* **2021**, *12* (1).

(86) Jia, X.; Li, J.; Wang, E. One-Pot Green Synthesis of Optically PH-Sensitive Carbon Dots with Upconversion Luminescence. *Nanoscale* **2012**, *4*, 5572–5575.

(87) Jiang, K.; Zhang, L.; Lu, J.; Xu, C.; Cai, C.; Lin, H. Triple-Mode Emission of Carbon Dots: Applications for Advanced Anti-Counterfeiting. *Angew. Chemie* **2016**, *128*, 7347–7351.

(88) Yan, F.; Sun, Z.; Zhang, H.; Sun, X.; Jiang, Y.; Bai, Z. The Fluorescence Mechanism of Carbon Dots, and Methods for Tuning Their Emission Color: A Review. *Microchim. Acta* **2019**, *186*.

(89) Reckmeier, C. J.; Schneider, J.; Susha, A. S.; Rogach, A. L. Luminescent Colloidal Carbon Dots: Optical Properties and Effects of Doping. *Opt. Express* **2016**, *24*, A312.

(90) Mehta, A.; Mishra, A.; Basu, S.; Shetti, N. P.; Reddy, K. R.; Saleh, T. A.; Aminabhavi, T. M. Band Gap Tuning and Surface Modification of Carbon Dots for Sustainable Environmental Remediation and Photocatalytic Hydrogen Production – A Review. *J. Environ. Manage.* **2019**, *250*.

(91) Zhu, S.; Song, Y.; Wang, J.; Wan, H.; Zhang, Y.; Ning, Y.; Yang, B. Photoluminescence Mechanism in Graphene Quantum Dots: Quantum Confinement Effect and Surface/Edge State. *Nano Today* **2017**, *13*, 10–14.

(92) Zhou, W.; Zhuang, J.; Li, W.; Hu, C.; Lei, B.; Liu, Y. Correction: Towards Efficient Dual-Emissive Carbon Dots through Sulfur and Nitrogen Co-Doped. *J. Mater. Chem. C* **2018**, *6*, 3104–3104.

(93) Gan, Z.; Xu, H.; Hao, Y. Mechanism for Excitation-Dependent Photoluminescence from Graphene Quantum Dots and Other Graphene Oxide Derivates: Consensus, Debates and Challenges. *Nanoscale* **2016**, *8* (15), 7794–

7807.

(94) Li, X.; Yan, L.; Ding, C.; Song, H.; Yang, Y.; Ma, C. Q. Carbon Dots in Perovskite Solar Cells: Properties, Applications, and Perspectives. *Energy and Fuels* **2023**, *37*, 876–901.

(95) Shan, F.; Fu, L.; Chen, X.; Xie, X.; Liao, C.; Zhu, Y.; Xia, H.; Zhang, J.; Yan, L.; Wang, Z.; Yu, X. Waste-to-Wealth: Functional Biomass Carbon Dots Based on Bee Pollen Waste and Application. *Chinese Chem. Lett.* **2022**, *33*, 2942–2948.

(96) Wang, Y.; Li, X.; Zhao, S.; Wang, B.; Song, X.; Xiao, J.; Lan, M. Synthesis Strategies, Luminescence Mechanisms, and Biomedical Applications of near-Infrared Fluorescent Carbon Dots. *Coord. Chem. Rev.* **2022**, *470*.

(97) Li, X.; Fu, Y.; Zhao, S.; Xiao, J. F.; Lan, M.; Wang, B.; Zhang, K.; Song, X.; Zeng, L. Metal Ions-Doped Carbon Dots: Synthesis, Properties, and Applications. *Chem. Eng. J.* **2022**, *430*.

(98) LeCroy, G. E.; Yang, S. T.; Yang, F.; Liu, Y.; Fernando, K. A. S.; Bunker, C. E.; Hu, Y.; Luo, P. G.; Sun, Y. P. Functionalized Carbon Nanoparticles: Syntheses and Applications in Optical Bioimaging and Energy Conversion. *Coord. Chem. Rev.* **2016**, *320–321*, 66–81.

(99) Zhong, J.; Chen, X.; Zhang, M.; Xiao, C.; Cai, L.; Khan, W. A.; Yu, K.; Cui, J.; He, L. Blood Compatible Heteratom-Doped Carbon Dots for Bio-Imaging of Human Umbilical Vein Endothelial Cells. *Chinese Chem. Lett.* **2020**, *31*, 769–773.

(100) Xu, Q.; Kuang, T.; Liu, Y.; Cai, L.; Peng, X.; Sreenivasan Sreeprasad, T.; Zhao, P.; Yu, Z.; Li, N. Heteroatom-Doped Carbon Dots: Synthesis, Characterization, Properties, Photoluminescence Mechanism and Biological Applications. *J. Mater. Chem. B* **2016**, *4*, 7204–7219.

(101) Mochalin, V. N.; Shenderova, O.; Ho, D.; Gogotsi, Y. The Properties and Applications of Nanodiamonds. *Nat. Nanotechnol.* **2012**, *7*, 11–23.

(102) Sh., A. Doped Carbon Dots for Sensing and Bioimaging Applications: A Minireview. *Nanomaterials* **2018**, 342.

(103) Zheng, X. T.; Ananthanarayanan, A.; Luo, K. Q.; Chen, P. Glowing Graphene Quantum Dots and Carbon Dots: Properties, Syntheses, and Biological Applications. *Small* **2015**, *11*, 1620–1636.

(104) Kar, S.; Bramhaiah, K.; John, N. S.; Bhattacharyya, S. Insight into the Multistate Emissive N, P-Doped Carbon Nano-Onions: Emerging Visible-Light Absorption for Photocatalysis. *Chem. - An Asian J.* **2021**, *16*, 1138–1149.

(105) Wang, S.; Zhou, Z.; Wang, Z.; Liu, Y.; Jacobson, O.; Shen, Z.; Fu, X.; Chen, Z. Y.; Chen, X. Gadolinium Metallofullerene-Based Activatable Contrast Agent for Tumor Signal Amplification and Monitoring of Drug Release. *Small* **2019**, *15* (16).

(106) Miao, S.; Liang, K.; Zhu, J.; Yang, B.; Zhao, D.; Kong, B. Hetero-Atom-Doped Carbon Dots: Doping Strategies, Properties and Applications. *Nano Today* **2020**, *33*.

(107) Yang, X. C.; Li, Q.; Tang, M.; Yang, Y. L.; Yang, W.; Hu, J. F.; Pu, X. L.; Liu, J.; Zhao, J. T.; Zhang, Z. J. One Stone, Two Birds: PH- and Temperature-Sensitive Nitrogen-Doped Carbon Dots for Multiple Anticounterfeiting and Multiple Cell Imaging. *ACS Appl. Mater. Interfaces* **2020**, *12*, 20849–20858.

(108) She, C.; Wang, Z.; Zeng, J.; Wu, F. G. Orange/Red Dual-Emissive Boron- and Nitrogen-Codoped Carbon Dots for Wash-Free and Selective Staining of Lipid Droplets in Live Cells. *Carbon N. Y.* **2022**, *191*, 636–645.

(109) Li, F.; Yang, D.; Xu, H. Non-Metal-Heteroatom-Doped Carbon Dots: Synthesis and Properties. *Chem. - A Eur. J.* **2019**, *25*, 1165–1176.

(110) Munusamy, S.; Mandlimath, T. R.; Swetha, P.; Al-Sehemi, A. G.; Pannipara, M.; Koppala, S.; Shanmugam, P.; Boonyuen, S.; Pothu, R.; Boddula, R. Nitrogen-Doped Carbon Dots: Recent Developments in Its Fluorescent Sensor Applications. *Environ. Res.* **2023**, *231*.

(111) Sarkar, S.; Sudolská, M.; Dubecký, M.; Reckmeier, C. J.; Rogach, A. L.; Zbořil, R.; Otyepka, M. Graphitic Nitrogen Doping in Carbon Dots Causes Red-Shifted Absorption. *J. Phys. Chem. C* **2016**, *120*, 1303–1308.

(112) Sudolská, M.; Dubecký, M.; Sarkar, S.; Reckmeier, C. J.; Zbořil, R.; Rogach, A. L.; Otyepka, M. Nature of Absorption Bands in Oxygen-Functionalized Graphitic Carbon Dots. *J. Phys. Chem. C* **2015**, *119*, 13369–13373.

(113) Hola, K.; Bourlinos, A. B.; Kozak, O.; Berka, K.; Siskova, K. M.; Havrdova, M.; Tucek, J.; Safarova, K.; Otyepka, M.; Giannelis, E. P.; Zboril, R. Photoluminescence Effects of Graphitic Core Size and Surface Functional Groups in Carbon Dots: COO- Induced Red-Shift Emission. *Carbon N. Y.* **2014**, *70*, 279–286.

(114) Sharma, A.; Gadly, T.; Neogy, S.; Ghosh, S. K.; Kumbhakar, M. Molecular Origin and Self-Assembly of Fluorescent Carbon Nanodots in Polar Solvents. **2017**. https://doi.org/10.1021/acs.jpclett.7b00170.

(115) Qu, D.; Zheng, M.; Du, P.; Zhou, Y.; Zhang, L.; Li, D.; Tan, H.; Zhao, Z.; Xie, Z.; Sun, Z. Highly Luminescent S, N Co-Doped Graphene Quantum Dots with Broad Visible Absorption Bands for Visible Light Photocatalysts. *Nanoscale* **2013**, *5* (24), 12272–12277. https://doi.org/10.1039/c3nr04402e.

(116) Das, A.; Gude, V.; Roy, D.; Chatterjee, T.; De, C. K.; Mandal, P. K. On the Molecular Origin of Photoluminescence of Nonblinking Carbon Dot. *J. Phys. Chem. Lett.* **2017**, 8, 5, 1044–1052.

(117) Wang, L.; Zhu, S.; Wang, H.; Qu, S.; Zhang, Y.; Zhang, J.; Chen, Q.; Al, W. E.T. Common Origin of Green Luminescence in Carbon Nanodots and Graphene Quantum Dots. **2014**, No. 3, 2541–2547.

(118) Q. Xu, P. Pu, J. Zhao, Y. Liu, C. Dong, C. Gao, Y. Chen, J. C. and H. Z. Materials Chemistry. *Underst. Chem. through Cars* **2020**, 144–163.

(119) Do, S.; Kwon, W.; Kim, Y. H.; Kang, S. R.; Lee, T.; Lee, T. W.; Rhee, S. W. N,S-Induced Electronic States of Carbon Nanodots Toward White Electroluminescence. *Adv. Opt. Mater.* **2016**, *4*, 276–284.

(120) Zhang, Y.; He, J. Facile Synthesis of S, N Co-Doped Carbon Dots and Investigation of Their Photoluminescence Properties. *Phys. Chem. Chem. Phys.* **2015**, *17*, 20154–20159.

(121) Wang, J.; Zheng, J.; Yang, Y.; Liu, X.; Qiu, J.; Tian, Y. Tunable Full-Color Solid-State Fluorescent Carbon Dots for Light Emitting Diodes. *SSRN Electron. J.* **2021**.

(122) Hosseini, S. M.; Mohammadnejad, J.; Najafi-Taher, R.; Zadeh, Z. B.; Tanhaei, M.; Ramakrishna, S. Multifunctional Carbon-Based Nanoparticles: Theranostic Applications in Cancer Therapy and Diagnosis. *ACS Appl. Bio Mater.* **2023**, *6* (4), 1323–1338.

(123) Pal, S. K.; Parashar, M.; Kanrar, B. B.; Panda, S.; Roy, N.; Paira, P.; Panda, D. N-Doped Yellow-Emissive Carbon Nanodots from Gallic Acid: Reaction Engineering, Stimuli-Responsive Red Emission, and Intracellular Localization. *J. Phys. Chem. C* **2021**, *125* (10), 5748–5759.

(124) Gao, W.; Song, H.; Wang, X.; Liu, X.; Pang, X.; Zhou, Y.; Gao, B.; Peng, X.

Carbon Dots with Red Emission for Sensing of Pt^{2+}, Au^{3+}, and Pd^{2+} and Their Bioapplications in Vitro and in Vivo. *ACS Appl. Mater. Interfaces* **2018**, *10*, 1147–1154.

(125) Zhang, M.; Wang, W.; Yuan, P.; Chi, C.; Zhang, J.; Zhou, N. Synthesis of Lanthanum Doped Carbon Dots for Detection of Mercury Ion, Multi-Color Imaging of Cells and Tissue, and Bacteriostasis. *Chem. Eng. J.* **2017**, *330*, 1137–1147.

(126) Yang, M.; Tang, Q.; Meng, Y.; Liu, J.; Feng, T.; Zhao, X.; Zhu, S.; Yu, W.; Yang, B. Reversible "off-On" Fluorescence of Zn^{2+}-Passivated Carbon Dots: Mechanism and Potential for the Detection of EDTA and Zn^{2+}. *Langmuir* **2018**, *34* (26), 7767–7775.

(127) Lesani, P.; Singh, G.; Viray, C. M.; Ramaswamy, Y.; Zhu, D. M.; Kingshott, P.; Lu, Z.; Zreiqat, H. Two-Photon Dual-Emissive Carbon Dot-Based Probe: Deep-Tissue Imaging and Ultrasensitive Sensing of Intracellular Ferric Ions. *ACS Appl. Mater. Interfaces* **2020**, *12*, 18395–18406.

(128) Liu, J.; Dong, Y.; Ma, Y.; Han, Y.; Ma, S.; Chen, H.; Chen, X. One-Step Synthesis of Red/Green Dual-Emissive Carbon Dots for Ratiometric Sensitive ONOO- Probing and Cell Imaging. *Nanoscale* **2018**, *10*, 13589–13598.

(129) Wei, Z.; Li, H.; Liu, S.; Wang, W.; Chen, H.; Xiao, L.; Ren, C.; Chen, X. Carbon Dots as Fluorescent/Colorimetric Probes for Real-Time Detection of Hypochlorite and Ascorbic Acid in Cells and Body Fluid. *Anal. Chem.* **2019**, *91*, 15477–15483.

(130) Pal, S. K.; Parashar, M.; Kanrar, B. B.; Panda, S.; Roy, N.; Paira, P.; Panda, D. N-Doped Yellow-Emissive Carbon Nanodots from Gallic Acid: Reaction Engineering, Stimuli-Responsive Red Emission, and Intracellular Localization. *J. Phys. Chem. C* **2021**,125, 5748-5759.

(131) Cailotto, S.; Negrato, M.; Daniele, S.; Luque, R.; Selva, M.; Amadio, E.; Perosa, A. Carbon Dots as Photocatalysts for Organic Synthesis: Metal-Free Methylene-Oxygen-Bond Photocleavage. *Green Chem.* **2020**, *22*, 1145–1149.

(132) Han, M.; Lu, S.; Qi, F.; Zhu, S.; Sun, H.; Yang, B. Carbon Dots–Implanted Graphitic Carbon Nitride Nanosheets for Photocatalysis: Simultaneously Manipulating Carrier Transport in Inter- and Intralayers. *Sol. RRL* **2020**, *4*.

(133) Xu, L.; Bai, X.; Guo, L.; Yang, S.; Jin, P.; Yang, L. Facial Fabrication of Carbon Quantum Dots (CDs)-Modified N-TiO_{2-x} Nanocomposite for the Efficient Photoreduction of Cr(VI) under Visible Light. *Chem. Eng. J.* **2019**, *357*, 473–486.

(134) Wang, S.; Li, L.; Zhu, Z.; Zhao, M.; Zhang, L.; Zhang, N.; Wu, Q.; Wang, X.; Li, G. Remarkable Improvement in Photocatalytic Performance for Tannery Wastewater Processing via SnS_2 Modified with N-Doped Carbon Quantum Dots: Synthesis, Characterization, and 4-Nitrophenol-Aided Cr(VI) Photoreduction. *Small* **2019**, *15*,1804515.

(135) Huang, S.; Jiang, S.; Pang, H.; Wen, T.; Asiri, A. M.; Alamry, K. A.; Alsaedi, A.; Wang, X.; Wang, S. Dual Functional Nanocomposites of Magnetic MnFe2O4 and Fluorescent Carbon Dots for Efficient U(VI) Removal. *Chem. Eng. J.* **2019**, *368*, 941–950.

(136) Xu, X.; Tang, W.; Zhou, Y.; Bao, Z.; Su, Y.; Hu, J.; Zeng, H. Steering Photoelectrons Excited in Carbon Dots into Platinum Cluster Catalyst for Solar-Driven Hydrogen Production. *Adv. Sci.* **2017**, *4*,1700273.

(137) Luo, H.; Liu, Y.; Dimitrov, S. D.; Steier, L.; Guo, S.; Li, X.; Feng, J.; Xie, F.; Fang, Y.; Sapelkin, A.; Wang, X.; Titirici, M. M. Pt Single-Atoms Supported

on Nitrogen-Doped Carbon Dots for Highly Efficient Photocatalytic Hydrogen Generation. *J. Mater. Chem. A* **2020**, *8* (29), 14690–14696.

(138) Yan, Y.; Chen, J.; Li, N.; Tian, J.; Li, K.; Jiang, J.; Liu, J.; Tian, Q.; Chen, P. Systematic Bandgap Engineering of Graphene Quantum Dots and Applications for Photocatalytic Water Splitting and CO2 Reduction. *ACS Nano* **2018**, *12*, 3523–3532.

(139) Liu, Z.; Hou, W.; Guo, H.; Wang, Z.; Wang, L.; Wu, M. Functional Group Modulation in Carbon Quantum Dots for Accelerating Photocatalytic CO2 Reduction. *ACS Appl. Mater. Interfaces* **2023**, *15* (28), 33868–33877.

(140) Sarma, D.; Majumdar, B.; Sarma, T. K. Visible-Light Induced Enhancement in the Multi-Catalytic Activity of Sulfated Carbon Dots for Aerobic Carbon-Carbon Bond Formation. *Green Chem.* **2019**, *21* (24), 6717–6726.

(141) Bhattacharyya, S.; Ehrat, F.; Urban, P.; Teves, R.; Wyrwich, R.; Döblinger, M.; Feldmann, J.; Urban, A. S.; Stolarczyk, J. K. Effect of Nitrogen Atom Positioning on the Trade-off between Emissive and Photocatalytic Properties of Carbon Dots. *Nat. Commun.* **2017**, *8*.

(142) Jana, B.; Reva, Y.; Scharl, T.; Strauss, V.; Cadranel, A.; Guldi, D. M. Carbon Nanodots for All-in-One Photocatalytic Hydrogen Generation. *J. Am. Chem. Soc.* **2021**, *143*, 20122–20132.

(143) Liu, C.; Fu, Y.; Xia, Y.; Zhu, C.; Hu, L.; Zhang, K.; Wu, H.; Huang, H.; Liu, Y.; Xie, T.; Zhong, J.; Kang, Z. Cascaded Photo-Potential in a Carbon Dot-Hematite System Driving Overall Water Splitting under Visible Light. *Nanoscale* **2018**, *10*, 2454–2460.

(144) Xu, X.; Ray, R.; Gu, Y.; Ploehn, H. J.; Gearheart, L.; Raker, K.; Scrivens, W. A. Electrophoretic Analysis and Purification of Fluorescent Single-Walled Carbon Nanotube Fragments. **2004**, 12736–12737.

(145) Kozák, O.; Sudolská, M.; Pramanik, G.; Cígler, P.; Otyepka, M.; Zbořil, R. Photoluminescent Carbon Nanostructures. *Chem. Mater.* **2016**, *28* (12), 4085–4128.

(146) Righetto, M.; Privitera, A.; Fortunati, I.; Mosconi, D.; Zerbetto, M.; Curri, M. L.; Corricelli, M.; Moretto, A.; Agnoli, S.; Franco, L.; Bozio, R.; Ferrante, C. Spectroscopic Insights into Carbon Dot Systems. *J. Phys. Chem. Lett.* **2017**, *8* (10), 2236–2242.

(147) Hu, C.; Li, M.; Qiu, J.; Sun, Y. P. Design and Fabrication of Carbon Dots for Energy Conversion and Storage. *Chem. Soc. Rev.* **2019**, *48* (8), 2315–2337.

(148) Jana, B.; Reva, Y.; Scharl, T.; Strauss, V.; Cadranel, A.; Guldi, D. M. Carbon Nanodots for All-in-One Photocatalytic Hydrogen Generation. *J. Am. Chem. Soc.* **2021**, 143, 20122–20132.

(149) Xiao, D.; Jiang, M.; Luo, X.; Liu, S.; Li, J.; Chen, Z.; Li, S. Sustainable Carbon Dot-Based AIEgens: Promising Light-Harvesting Materials for Enhancing Photosynthesis. *ACS Sustain. Chem. Eng.* **2021**, *9* (11), 4139–4145.

(150) Abbas, F.; Kumar, S.; Pal, S. K.; Panda, D. Carbon Nanodot Doped in Polymer Film: Plasmophore Enhancement, Catalytic Amination and White-Light Generation. *J. Mol. Liq.* **2022**, *347*, 118001.

(151) Kumar Barman, B.; Nagao, T.; Nanda, K. K. Dual Roles of a Transparent Polymer Film Containing Dispersed N-Doped Carbon Dots: A High-Efficiency Blue Light Converter and UV Screen. *Appl. Surf. Sci.* **2020**, *510*.

(152) Zhang, P.; Wei, J.-S.; Ding, H.; Xiong, H.-M.; Zhou, Z.-Y.; Gao, Q.-Y. Solvent-Controlled Synthesis of Highly Luminescent Carbon Dots with a Wide Color Gamut and Narrowed Emission Peak Widths. *Small* **2018**, *14*, 1800612.

(153) Reckmeier, C. J.; Schneider, J.; Xiong, Y.; Häusler, J.; Kasák, P.; Schnick, W.; Rogach, A. L. Aggregated Molecular Fluorophores in the Ammonothermal Synthesis of Carbon Dots. *Chem. Mater.* **2017**, *29*, 10352–10361.

(154) Sharma, A.; Gadly, T.; Gupta, A.; Ballal, A.; Ghosh, S. K.; Kumbhakar, M. Origin of Excitation Dependent Fluorescence in Carbon Nanodots. *J. Phys. Chem. Lett.* **2016**, *7*, 3695–3702.

(155) Sciortino, A.; Marino, E.; Dam, B. Van; Schall, P.; Cannas, M.; Messina, F. Solvatochromism Unravels the Emission Mechanism of Carbon Nanodots. *J. Phys. Chem. Lett.* **2016**, *7*, 3419–3423.

(156) Das, A.; Roy, D.; De, C. K.; Mandal, P. K. Where Does the Fluorescing Moiety Reside in a Carbon Dot? - Investigations Based on Fluorescence Anisotropy Decay and Resonance Energy Transfer Dynamics. *Phys. Chem. Chem. Phys.* **2017**, *20*, 2251–2259.

(157) Fu, M.; Ehrat, F.; Wang, Y.; Milowska, K. Z.; Reckmeier, C.; Rogach, A. L.; Stolarczyk, J. K.; Urban, A. S.; Feldmann, J. Carbon Dots: A Unique Fluorescent Cocktail of Polycyclic Aromatic Hydrocarbons. *Nano Lett.* **2015**, *15*, 6030–6035.

(158) Dutta Choudhury, S.; Chethodil, J. M.; Gharat, P. M.; Praseetha, P. K.; Pal, H. PH-Elicited Luminescence Functionalities of Carbon Dots: Mechanistic Insights. *J. Phys. Chem. Lett.* **2017**, *8*, 1389–1395.

(159) Khan, S.; Sharma, A.; Ghoshal, S.; Jain, S.; Hazra, M. K.; Nandi, C. K. Small Molecular Organic Nanocrystals Resemble Carbon Nanodots in Terms of Their Properties. *Chem. Sci.* **2018**, *9*, 175–180.

(160) Gude, V.; Das, A.; Chatterjee, T.; Mandal, P. K. Molecular Origin of Photoluminescence of Carbon Dots: Aggregation-Induced Orange-Red Emission. **2016**, 28274–28280.

(161) Schneider, J.; Reckmeier, C. J.; Xiong, Y.; Von Seckendorff, M.; Susha, A. S.; Kasak, P.; Rogach, A. L. Molecular Fluorescence in Citric Acid-Based Carbon Dots. *J. Phys. Chem. C* **2017**, *121*, 2014–2022.

(162) Shi, L.; Yang, J. H.; Zeng, H. B.; Chen, Y. M.; Yang, S. C.; Wu, C.; Zeng, H.; Yoshihito, O.; Zhang, Q. Carbon Dots with High Fluorescence Quantum Yield: The Fluorescence Originates from Organic Fluorophores. *Nanoscale* **2016**, *8* (30), 14374–14378. https://doi.org/10.1039/c6nr00451b.

(163) Dong, Y.; Pang, H.; Yang, H. Bin; Guo, C.; Shao, J.; Chi, Y.; Li, C. M.; Yu, T. Carbon-Based Dots Co-Doped with Nitrogen and Sulfur for High Quantum Yield and Excitation-Independent Emission. *Angew. Chem. Int. Ed.* **2013**, *52*, 7800–7804.

(164) Qu, D.; Zheng, M.; Du, P.; Zhou, Y.; Zhang, L.; Li, D.; Tan, H.; Zhao, Z.; Xie, Z.; Sun, Z. Highly Luminescent S, N Co-Doped Graphene Quantum Dots with Broad Visible Absorption Bands for Visible Light Photocatalysts. *Nanoscale* **2013**, *5*, 12272.

(165) Zhan, J.; Geng, B.; Wu, K.; Xu, G.; Wang, L.; Guo, R.; Lei, B.; Zheng, F.; Pan, D.; Wu, M. A Solvent-Engineered Molecule Fusion Strategy for Rational Synthesis of Carbon Quantum Dots with Multicolor Bandgap Fluorescence. *Carbon N. Y.* **2018**, *130*, 153–163.

(166) Sun, Z.; Yan, F.; Xu, J.; Zhang, H.; Chen, L. Solvent-Controlled Synthesis Strategy of Multicolor Emission Carbon Dots and Its Applications in Sensing and Light-Emitting Devices. *Nano Res.* **2022**, *15*, 414–422.

(167) Heravi, M. M.; Ghavidel, M.; Mohammadkhani, L. Beyond a Solvent: Triple Roles of Dimethylformamide in Organic Chemistry. *RSC Adv.* **2018**, *8*, 27832–

27862.

(168) Panda, D.; Khatua, S.; Datta, A. Enhanced Fluorescence of Epicocconone in Surfactant Assemblies as a Consequence of Depth-Dependent Microviscosity. *J. Phys. Chem. B* **2007**, *111*, 1648–1656.

(169) Rakshit, S.; Das, S.; Poonia, P.; Maini, R.; Kumar, A.; Datta, A. White Light Generation from a Self-Assembled Fluorogen-Surfactant Composite Light Harvesting Platform. *J. Phys. Chem. B* **2020**, *124*, 7484–7493.

(170) Panda, D.; Ghosh, D.; Datta, A. Acid-Base Behavior of 3-Aminoquinoline in Its Ground and Excited States. *J. Photochem. Photobiol. A Chem.* **2009**, *207*, 254–259.

(171) Das, S.; Singh, A. K.; Biswas, D. S.; Datta, A. Dynamics of Preferential Solvation of 5-Aminoquinoline in Hexane-Alcohol Solvent Mixtures. *J. Phys. Chem. B* **2019**, *123*, 10267–10274.

(172) Joshi, C. P.; Panda, D.; Martella, D. J.; Andoy, N. M.; Chen, T. Y.; Gaballa, A.; Helmann, J. D.; Chen, P. Direct Substitution and Assisted Dissociation Pathways for Turning off Transcription by a MerR-Family Metalloregulator. *Proc. Natl. Acad. Sci. U. S. A.* **2012**, *109*, 15121–15126.

(173) Zeng, Y.; Gao, R.; Wu, T.; Cho, C.; Tan, K. Fluorescent Probe Encapsulated in SNAP-Tag Protein Cavity To Eliminate Nonspecific Fluorescence and Increase Detection Sensitivity. *Bioconjug. Chem.* **2016**, *27*, 1872–1879.

(174) Lakowicz, J. R. *Principles of Fluorescence Spectroscopy*, 3rd Edn.; Springer-Verlag New York Inc.: New York, 2006.

(175) Khan, S.; Li, W.; Karedla, N.; Thiart, J.; Gregor, I.; Chizhik, A. M.; Enderlein, J.; Nandi, C. K.; Chizhik, A. I. Charge-Driven Fluorescence Blinking in Carbon Nanodots. *J. Phys. Chem. Lett.* **2017**, *8*, 5751–5757.

(176) Das, S. K.; Liu, Y.; Yeom, S.; Kim, D. Y.; Richards, C. I. Single-Particle Fluorescence Intensity Fluctuations of Carbon Nanodots. *Nano Lett.* **2014**, *14*, 620–625.

(177) Dubey, R.; Desiraju, G. R. Combinatorial Crystal Synthesis: Structural Landscape of Phloroglucinol:1,2-Bis(4-Pyridyl)Ethylene and Phloroglucinol:Phenazine. *Angew. Chemie - Int. Ed.* **2014**, *53*, 13178–13182.

(178) Kazimierczuk, K. Charge-Assisted $N^{(+)}$–H···$^{(-)}$S Hydrogen Bonds in the Crystal Structure of Selected Diammonium Thiophenolates. *Struct. Chem.* **2016**, *27*, 1005–1016.

(179) Mishra, M. K.; Mukherjee, A.; Ramamurty, U.; Desiraju, G. R. Crystal Chemistry and Photomechanical Behavior of 3,4-Dimethoxycinnamic Acid: Correlation between Maximum Yield in the Solid-State Topochemical Reaction and Cooperative Molecular Motion. *IUCrJ* **2015**, *2*, 653–660.

(180) Lieber, E.; Rao, C. N. R.; Ramachandran, J. The Infrared Spectra of Organic Thiocyanates and Isothiocyanates. *Spectrochim. Acta* **1959**, *13*, 296–299.

(181) Huang, S.; Sinha, J.; Podgórski, M.; Zhang, X.; Claudino, M.; Bowman, C. N. Mechanistic Modeling of the Thiol-Michael Addition Polymerization Kinetics: Structural Effects of the Thiol and Vinyl Monomers. *Macromolecules* **2018**, *51*, 5979–5988.

(182) Kemp, W. Organic Spectroscopy. *Palgrave Macmillan* **2008**.

(183) Mao, X.; Liu, C.; Hesari, M.; Zou, N.; Chen, P. Super-Resolution Imaging of Non-Fluorescent Reactions via Competition. *Nat. Chem.* **2019**, *11*, 687–694.

(184) Das, S. K.; Dickinson, C.; Lafir, F.; Brougham, D. F.; Marsili, E. Synthesis, Characterization and Catalytic Activity of Gold Nanoparticles Biosynthesized with Rhizopus Oryzae Protein Extract. *Green Chem.* **2012**, *14*, 1322–1334.

(185) Frisch, M. J.; Trucks, G. W.; Schlegel, H. B.; Scuseria, G. E.; Robb, M. A.; Cheeseman, J. R.; Scalmani, G.; Barone, V.; Petersson, G. A.; Nakatsuji, H.; et Al., , Revision C.01, Gaussian, Inc., Wallingford CT, 2016. *Gaussian 16,* **2016**,

(186) Panda, D.; Mishra, P. P.; Khatua, S.; Koner, A. L.; Sunoj, R. B.; Datta, A. Anomalous Excited-State Dynamics of Lucifer Yellow CH in Solvents of High Polarity: Evidence for an Intramolecular Proton Transfer. *J. Phys. Chem. A* **2006**, *110*, 5585–5591.

(187) Halim, S. A.; Khalil, A. K. TD-DFT Calculations, NBO Analysis and Electronic Absorption Spectra of Some Thiazolo[3,2-a]Pyridine Derivatives. *J. Mol. Struct.* **2017**, *1147*, 651–667.

(188) Panda, D.; Datta, A. The Role of the Ring Nitrogen and the Amino Group in the Solvent Dependence of the Excited-State, Dynamics of 3-Aminoquinoline. *J. Chem. Phys.* **2006**, *125*, 1–9.

(189) Mishra, P. P.; Bhatnagar, J.; Datta, A. The Interplay of Hydrophobic and Electrostatic Effects in the Surfactant-Induced Aggregation/Deaggregation of Chlorin P6. *J. Phys. Chem. B* **2005**, *109*, 24225–24230.

(190) Iyer, E. S. S.; Datta, A. Importance of Electrostatic Interactions in the Mobility of Cations in Nafion. *J. Phys. Chem. B* **2011**, *115*, 8707–8712.

(191) Mukherjee, T. K.; Panda, D.; Datta, A. Excited-State Proton Transfer of 2-(2′-Pyridyl)Benzimidazole in Microemulsions: Selective Enhancement and Slow Dynamics in Aerosol OT Reverse Micelles with an Aqueous Core. *J. Phys. Chem. B* **2005**, *109*, 18895–18901.

(192) Gong, J.; Li, C.; Wasielewski, M. R. Advances in Solar Energy Conversion. *Chem. Soc. Rev.* **2019**, *48*, 1862–1864.

(193) Liu, J.; Mantell, J.; Jones, M. R. Minding the Gap between Plant and Bacterial Photosynthesis within a Self-Assembling Biohybrid Photosystem. *ACS Nano* **2020**, 14, 4536-4549.

(194) Li, D.; Li, W.; Zhang, H.; Zhang, X.; Zhuang, J.; Liu, Y.; Hu, C.; Lei, B. Far-Red Carbon Dots as Efficient Light-Harvesting Agents for Enhanced Photosynthesis. *ACS Appl. Mater. Interfaces* **2020**, *12*, 21009–21019.

(195) Wu, D.; Sedgwick, A. C.; Gunnlaugsson, T.; Akkaya, E. U.; Yoon, J.; James, T. D. Fluorescent Chemosensors: The Past, Present and Future. *Chem. Soc. Rev.* **2017**, *46*, 7105–7123.

(196) Carter, K. P.; Young, A. M.; Palmer, A. E. Fluorescent Sensors for Measuring Metal Ions in Living Systems. *Chem. Rev.* **2014**, *114*, 4564–4601.

(197) Zhang, Z.; Zhao, Z.; Wu, L.; Lu, S.; Ling, S.; Li, G.; Xu, L.; Ma, L.; Hou, Y.; Wang, X.; Li, X.; He, G.; Wang, K.; Zou, B.; Zhang, M. Emissive Platinum(II) Cages with Reverse Fluorescence Resonance Energy Transfer for Multiple Sensing. *J. Am. Chem. Soc.* **2020**, *142*, 2592–2600.

(198) Benitez-Martin, C.; Guadix, J. A.; Pearson, J. R.; Najera, F.; Perez-Pomares, J. M.; Perez-Inestrosa, E. Indolenine-Based Derivatives as Customizable Two-Photon Fluorescent Probes for PH Bioimaging in Living Cells. *ACS Sensors* **2020**, *5* (4), 1068–1074.

(199) Cao, D.; Liu, Z.; Verwilst, P.; Koo, S.; Jangjili, P.; Kim, J. S.; Lin, W. Coumarin-Based Small-Molecule Fluorescent Chemosensors. *Chem. Rev.* **2019**, *119* (18), 10403–10519.

(200) Park, Y. I.; Postupna, O.; Zhugayevych, A.; Shin, H.; Park, Y. S.; Kim, B.; Yen, H. J.; Cheruku, P.; Martinez, J. S.; Park, J. W.; Tretiak, S.; Wang, H. L. A New PH Sensitive Fluorescent and White Light Emissive Material through Controlled Intermolecular Charge Transfer. *Chem. Sci.* **2015**, *6*, 789–797.

(201) Naumann, R.; Lehmann, F.; Goez, M. Generating Hydrated Electrons for Chemical Syntheses by Using a Green Light-Emitting Diode (LED). *Angew. Chemie - Int. Ed.* **2018**, *57*, 1078–1081.

(202) Wang, G.; Adil, M. A.; Zhang, J.; Wei, Z. Large-Area Organic Solar Cells: Material Requirements, Modular Designs, and Printing Methods. *Adv. Mater.* **2019**, *31*, 1–34.

(203) Meng, L.; Zhang, Y.; Wan, X.; Li, C.; Zhang, X.; Wang, Y.; Ke, X.; Xiao, Z.; Ding, L.; Xia, R.; Yip, H. L.; Cao, Y.; Chen, Y. Organic and Solution-Processed Tandem Solar Cells with 17.3% Efficiency. *Science.* **2018**, *361* (6407), 1094–1098.

(204) Chan, J.; Dodani, S. C.; Chang, C. J. Reaction-Based Small-Molecule Fluorescent Probes for Chemoselective Bioimaging. *Nat. Chem.* **2012**, *4*, 973–984.

(205) Murfin, L. C.; Weber, M.; Park, S. J.; Kim, W. T.; Lopez-Alled, C. M.; McMullin, C. L.; Pradaux-Caggiano, F.; Lyall, C. L.; Kociok-Köhn, G.; Wenk, J.; Bull, S. D.; Yoon, J.; Kim, H. M.; James, T. D.; Lewis, S. E. Azulene-Derived Fluorescent Probe for Bioimaging: Detection of Reactive Oxygen and Nitrogen Species by Two-Photon Microscopy. *J. Am. Chem. Soc.* **2019**, *141*, 19389–19396.

(206) Jiang, K.; Sun, S.; Zhang, L.; Lu, Y.; Wu, A.; Cai, C.; Lin, H. Red, Green, and Blue Luminescence by Carbon Dots: Full-Color Emission Tuning and Multicolor Cellular Imaging. *Angew. Chemie - Int. Ed.* **2015**, *54* (18), 5360–5363.

(207) Wang, Y.; Zhou, D.; Huang, H.; Wang, Y.; Hu, Z.; Li, X. A Yellow-Emissive Carbon Nanodot-Based Ratiometric Fluorescent Nanosensor for Visualization of Exogenous and Endogenous Hydroxyl Radicals in the Mitochondria of Live Cells. *J. Mater. Chem. B* **2019**, *7*, 3737–3744.

(208) Banerjee, R.; Mukherjee, G.; Patra, K. C. Microbial Transformation of Tannin-Rich Substrate to Gallic Acid through Co-Culture Method. *Bioresour. Technol.* **2005**, *96*, 949–953.

(209) Jiao, P.; Yang, C.; Yang, L.; Deng, Z.; Shao, J.; Zeng, G.; Yan, Z. The Recovery of Gallic Acid from Wastewater by Extraction with Tributyl Phosphate/4-Methyl-2-Pentanone/: N -Hexane, Tributyl Phosphate/ n -Octanol/ n -Hexane and n -Hexanol. *RSC Adv.* **2016**, *6*, 93626–93639.

(210) Houshyar, Z.; Khoshfetrat, A. B.; Fatehifar, E. Influence of Ozonation Process on Characteristics of Pre-Alkalized Tannery Effluents. *Chem. Eng. J.* **2012**, *191*, 59–65.

(211) Yin, Z.; Rabeah, J.; Brückner, A.; Wu, X. F. Gallic Acid-Promoted SET Process for Cyclobutanone Oximes Activation and (Carbonylative-)Alkylation of Olefins. *ACS Catal.* **2018**, *8*, 10926–10930.

(212) Stathi, P.; Louloudi, M.; Deligiannakis, Y. Efficient Low-Temperature H_2 Production from HCOOH/HCOO- by [Pd0@SiO_2-Gallic Acid] Nanohybrids: Catalysis and the Underlying Thermodynamics and Mechanism. *Energy and Fuels* **2016**, *30*, 8613–8622.

(213) Muzart, J. N,N-Dimethylformamide: Much More than a Solvent. *Tetrahedron* **2009**, *65*, 8313–8323.

(214) Shamsi, J.; Urban, A. S.; Imran, M.; De Trizio, L.; Manna, L. Metal Halide Perovskite Nanocrystals: Synthesis, Post-Synthesis Modifications, and Their Optical Properties. *Chem. Rev.* **2019**, *119*, 3296–3348.

(215) Parekh, B. P.; Tangonan, A. A.; Newaz, S. S.; Sanduja, S. K.; Ashraf, A. Q.;

Krishnamoorti, R.; Lee, T. R. Use of DMF as Solvent Allows for the Facile Synthesis of Soluble MEH-PPV. *Macromolecules* **2004**, *37*, 8883–8887.

(216) Outin, J.; Quellier, P.; Bélanger, G. Sequential One-Pot Vilsmeier-Haack and Organocatalyzed Mannich Cyclizations to Functionalized Benzoindolizidines and Benzoquinolizidines. *J. Org. Chem.* **2020**, *85*, 4712–4729.

(217) Lu, S. R.; Lai, Y. H.; Chen, J. H.; Liu, C. Y.; Mong, K. K. T. Dimethylformamide: An Unusual Glycosylation Modulator. *Angew. Chemie - Int. Ed.* **2011**, *50*, 7315–7320.

(218) Ermakova, Y. G.; Sen, T.; Bogdanova, Y. A.; Smirnov, A. Y.; Baleeva, N. S.; Krylov, A. I.; Baranov, M. S. Pyridinium Analogues of Green Fluorescent Protein Chromophore: Fluorogenic Dyes with Large Solvent-Dependent Stokes Shift. *J. Phys. Chem. Lett.* **2018**, *9*, 1958–1963.

(219) Anantharaj, S.; Nithiyanantham, U.; Ede, S. R.; Ayyappan, E.; Kundu, S. π-Stacking Intercalation and Reductant Assisted Stabilization of Osmium Organosol for Catalysis and SERS Applications. *RSC Adv.* **2015**, *5*, 11850–11860.

(220) Mooney, J.; Kambhampati, P. Get the Basics Right: Jacobian Conversion of Wavelength and Energy Scales for Quantitative Analysis of Emission Spectra. *J. Phys. Chem. Lett.* **2013**, *4*, 3316–3318.

(221) Koti, A. S. R.; Krishna, M. M. G.; Periasamy, N. Time-Resolved Area-Normalized Emission Spectroscopy (TRANES): A Novel Method for Confirming Emission from Two Excited States. *J. Phys. Chem. A* **2001**, *105*, 1767–1771.

(222) Bhattacharyya, K.; Bagchi, B. Slow Dynamics of Constrained Water in Complex Geometries. *J. Phys. Chem. A* **2000**, *104*, 10603–10613.

(223) Balasubramanian, S.; Pal, S.; Bagchi, B. Hydrogen-Bond Dynamics near a Micellar Surface: Origin of the Universal Slow Relaxation at Complex Aqueous Interfaces. *Phys. Rev. Lett.* **2002**, *89*, 1–12.

(224) Smirnov, A. V.; Das, K.; English, D. S.; Wan, Z.; Kraus, G. A.; Petrich, J. W. Excited-State Intramolecular H Atom Transfer of Hypericin and Hypocrellin A Investigated by Fluorescence Upconversion. *J. Phys. Chem. A* **1999**, *103*, 7949–7957.

(225) Rumble, C. A.; Breffke, J.; Maroncelli, M. Solvation Dynamics and Proton Transfer in Diethylaminohydroxyflavone. *J. Phys. Chem. B* **2017**, *121*, 630–637.

(226) Ekimova, M.; Hoffmann, F.; Bekçioğlu-Neff, G.; Rafferty, A.; Kornilov, O.; Nibbering, E. T. J.; Sebastiani, D. Ultrafast Proton Transport between a Hydroxy Acid and a Nitrogen Base along Solvent Bridges Governed by the Hydroxide/Methoxide Transfer Mechanism. *J. Am. Chem. Soc.* **2019**, *141*, 14581–14592.

(227) Dettori, R.; Ceriotti, M.; Hunger, J.; Colombo, L.; Donadio, D. Energy Relaxation and Thermal Diffusion in Infrared Pump-Probe Spectroscopy of Hydrogen-Bonded Liquids. *J. Phys. Chem. Lett.* **2019**, 3447–3452.

(228) Fu, W.; Yan, C.; Guo, Z.; Zhang, J.; Zhang, H.; Tian, H.; Zhu, W. H. Rational Design of Near-Infrared Aggregation-Induced-Emission-Active Probes: In Situ Mapping of Amyloid-β Plaques with Ultrasensitivity and High-Fidelity. *J. Am. Chem. Soc.* **2019**, *141*, 3171–3177.

(229) Hong, Y.; Lam, J. W. Y.; Tang, B. Z. Aggregation-Induced Emission: Phenomenon, Mechanism and Applications. *Chem. Commun.* **2009**, No. 29, 4332–4353.

(230) Mazumdar, P.; Maity, S.; Shyamal, M.; Das, D.; Sahoo, G. P.; Misra, A. Proton Triggered Emission and Selective Sensing of Picric Acid by the Fluorescent Aggregates of 6,7-Dimethyl-2,3-Bis-(2-Pyridyl)-Quinoxaline. *Phys. Chem. Chem. Phys.* **2016**, *18*, 7055–7067.

(231) Bu, F.; Duan, R.; Xie, Y.; Yi, Y.; Peng, Q.; Hu, R.; Qin, A.; Zhao, Z.; Tang, B. Z. Unusual Aggregation-Induced Emission of a Coumarin Derivative as a Result of the Restriction of an Intramolecular Twisting Motion. *Angew. Chemie - Int. Ed.* **2015**, *54*, 14492–14497.

(232) Chen, J.; Ma, S.; Zhang, J.; Wang, L.; Ye, L.; Li, B.; Xu, B.; Tian, W. Proton-Triggered Hypsochromic Luminescence in 1,1′-(2,5-Distyryl-1,4- Phenylene) Dipiperidine. *J. Phys. Chem. Lett.* **2014**, *5*, 2781–2784.

(233) Deng, Y.; Yuan, W.; Jia, Z.; Liu, G. H- and J-Aggregation of Fluorene-Based Chromophores. *J. Phys. Chem. B* **2014**, *118*, 14536–14545.

(234) Nyren-erickson, E. K.; Haldar, M. K.; Totzauer, J. R.; Ceglowski, R.; Patel, D. S.; Friesner, D. L.; Srivastava, D. K.; Mallik, S. Glycosaminoglycan-Mediated Selective Changes in the Aggregation States, Zeta Potentials, and Intrinsic Stability of Liposomes. *Langmuir* **2012**, 28, 16115−16125.

(235) Kawasaki, M.; Inokuma, H. Contribution of Electrostatic Cohesive Energy in Two-Dimensional J-Aggregation of Cyanine Dye. **1999**, 1233–1241.

(236) Vella, F. *Principles of Bioinorganic Chemistry*; University Science Books: New York, 1995; Vol. 23.

(237) Rondeau, V.; Commenges, D.; Jacqmin-Gadda, H.; Dartigues, J. F. Relation between Aluminum Concentrations in Drinking Water and Alzheimer’s Disease: An 8-Year Follow-up Study. *Am. J. Epidemiol.* **2000**, *152*, 59–66.

(238) Sarkar, D.; Ghosh, P.; Gharami, S.; Mondal, T. K.; Murmu, N. A Novel Coumarin Based Molecular Switch for the Sequential Detection of Al^{3+} and F^{-}: Application in Lung Cancer Live Cell Imaging and Construction of Logic Gate. *Sensors Actuators, B Chem.* **2017**, *242*, 338–346.

(239) Haedler, A. T.; Kreger, K.; Issac, A.; Wittmann, B.; Kivala, M.; Hammer, N.; Köhler, J.; Schmidt, H. W.; Hildner, R. Long-Range Energy Transport in Single Supramolecular Nanofibres at Room Temperature. *Nature* **2015**, *523*, 196–199.

(240) Desiraju, G. R. The C-H···O Hydrogen Bond: Structural Implications and Supramolecular Design. *Acc. Chem. Res.* **1996**, *29* (9), 441–449.

(241) Sarkhel, B.; Chatterjee, A.; Das, D. Covalent Catalysis by Cross β Amyloid Nanotubes. *J. Am. Chem. Soc.* **2020**, *142*, 4098–4103.

(242) Sarkar, A.; Sasmal, R.; Empereur-mot, C.; Bochicchio, D.; Kompella, S. V. K.; Sharma, K.; Dhiman, S.; Sundaram, B.; Agasti, S. S.; Pavan, G. M.; George, S. J. Self-Sorted, Random, and Block Supramolecular Copolymers via Sequence Controlled, Multicomponent Self-Assembly. *J. Am. Chem. Soc.* **2020**, *142*, 7606–7617.

(243) Fukaya, N.; Ogi, S.; Sotome, H.; Fujimoto, K. J.; Yanai, T.; Nils, B.; Fern, G.; Miyasaka, H.; Yamaguchi, S. Impact of Hydrophobic/Hydrophilic Balance on Aggregation Pathways, Morphologies, and Excited-State Dynamics of Amphiphilic Diketopyrrolopyrrole Dyes in Aqueous Media. *J. Am. Chem. Soc.* **2022**, 144, 22479–2249.

(244) Jalani, K.; Dhiman, S.; Jain, A.; George, S. J. Temporal Switching of an Amphiphilic Self-Assembly by a Chemical Fuel-Driven Conformational Response. *Chem. Sci.* **2017**, *8*, 6030–6036.

(245) Sikder, A.; Ghosh, S. Hydrogen-Bonding Regulated Assembly of Molecular

and Macromolecular Amphiphiles. *Mater. Chem. Front.* **2019**, *3*, 2602–2616.

(246) Lu, Y.-C.; Lee, C.-H.; Kuo, H.-H.; Chiang, H.-C.; Yao, C.-T.; Sung, H.-L.; Lee, G.-H.; Lai, L.-L. Reversible Photoluminescence of an H-Bonded Organic Framework Based on Macrocyclic Triazine in Solvation and Desolvation. *Cryst. Growth Des.* **2020**, *20*, 6421–6429.

(247) Hisaki, I.; Xin, C.; Takahashi, K.; Nakamura, T. Designing Hydrogen-Bonded Organic Frameworks (HOFs) with Permanent Porosity. *Angew. Chemie Int. Ed.* **2019**, *58*, 11160–11170.

(248) Tu, T.-H.; Chen, Y.-T.; Chen, Y.-A.; Wei, Y.-C.; Chen, Y.-H.; Chen, C.-L.; Shen, J.-Y.; Chen, Y.-H.; Ho, S.-Y.; Cheng, K.-Y.; Lee, S.-L.; Chen, C.; Chou, P.-T. The Cyclic Hydrogen-Bonded 6-Azaindole Trimer and Its Prominent Excited-State Triple-Proton-Transfer Reaction. *Angew. Chemie Int. Ed.* **2018**, *57*, 5020–5024.

(249) Greenwald, J.; Friedmann, M. P.; Riek, R. Amyloid Aggregates Arise from Amino Acid Condensations under Prebiotic Conditions. *Angew. Chemie Int. Ed.* **2016**, *55*, 11609–11613.

(250) He, Y.; Ye, T.; Su, M.; Zhang, C.; Ribbe, A. E.; Jiang, W.; Mao, C. Hierarchical Self-Assembly of DNA into Symmetric Supramolecular Polyhedra. *Nature* **2008**, *452*, 198–201.

(251) Zhang, J.; Piunova, V. A.; Liu, Y.; Tek, A.; Yang, Q.; Frommer, J.; Liu, G.; Sly, J. Controlled Molecular Assembly via Dynamic Confinement of Solvent. *J. Phys. Chem. Lett.* **2018**, *9*, 6232–6237.

(252) Thakuria, R.; Cherukuvada, S.; Nangia, A. Crystal Structures of Pyrogallol, Its Hydrate, and Stable Multiple z ′ Cocrystals with n-Heterocycles Containing Metastable Conformers of Pyrogallol. *Cryst. Growth Des.* **2012**, *12*, 3944–3953.

(253) Roy, S.; Gaur, R.; Paul, M.; Rajkumar, M.; Desiraju, G. R. Synthetic Strategies toward Higher Cocrystals of Some Resorcinols. *Cryst. Growth Des.* **2022**, *22*, 7578–7589.

(254) Shin, M.; Park, E.; Lee, H. Plant-Inspired Pyrogallol-Containing Functional Materials. *Adv. Funct. Mater.* **2019**, *29*, 1903022.

(255) Fahlman, M.; Fabiano, S.; Gueskine, V.; Simon, D.; Berggren, M.; Crispin, X. Interfaces in Organic Electronics. *Nat. Rev. Mater.* **2019**, *4*, 627–650.

(256) Tang, X.; Zhang, Y.; Kothalawala, N. L.; Wen, X.; Kim, D. Y.; Yang, F. MAPbBr 3 Nanocrystals from Aqueous Solution for Poly(Methyl Methacrylate)-MAPbBr 3 Nanocrystal Films with Compression-Resistant Photoluminescence. *Nanotechnology* **2022**, *33*, 235605.

(257) Spano, F. C.; Silva, C. H- and J-Aggregate Behavior in Polymeric Semiconductors. *Annu. Rev. Phys. Chem.* **2014**, *65*, 477–500.

(258) Hestand, N. J.; Spano, F. C. Expanded Theory of H- and J-Molecular Aggregates: The Effects of Vibronic Coupling and Intermolecular Charge Transfer. *Chem. Rev.* **2018**, *118*, 7069–7163.

(259) Flanders, N. C.; Kirschner, M. S.; Kim, P.; Fauvell, T. J.; Evans, A. M.; Helweh, W.; Spencer, A. P.; Schaller, R. D.; Dichtel, W. R.; Chen, L. X. Large Exciton Diffusion Coefficients in Two-Dimensional Covalent Organic Frameworks with Different Domain Sizes Revealed by Ultrafast Exciton Dynamics. *J. Am. Chem. Soc.* **2020**, *142*, 14957–14965.

(260) Bricks, J. L.; Slominskii, Y. L.; Panas, I. D.; Demchenko, A. P. Fluorescent J-Aggregates of Cyanine Dyes: Basic Research and Applications Review. *Methods Appl. Fluoresc.* **2018**, *6*, 1.

(261) Belko, N. V.; Gusakov, G. A.; Poznyak, S. K.; Tikhomirov, S. A.; Lugovski, A. P.; Samtsov, M. P. H*- and J-Aggregates of an Indotricarbocyanine Dye: Steady-State Spectral Properties and Excited-State Dynamics. *J. Phys. Chem. C* **2021**, 126, 7922–7932.

(262) Krieg, E.; Niazov-Elkan, A.; Cohen, E.; Tsarfati, Y.; Rybtchinski, B. Noncovalent Aqua Materials Based on Perylene Diimides. *Acc. Chem. Res.* **2019**, *52*, 2634–2646.

(263) Cheng, H.; Zhang, S.; Bai, E.; Cao, X.; Wang, J.; Qi, J.; Liu, J.; Zhao, J.; Zhang, L.; Yoon, J. Future-Oriented Advanced Diarylethene Photoswitches: From Molecular Design to Spontaneous Assembly Systems. *Adv. Mater.* **2022**, *34* (16), 2108289.

(264) Maiti, N. C.; Mazumdar, S.; Periasamy, N. J- and H-Aggregates of Porphyrin−Surfactant Complexes: Time-Resolved Fluorescence and Other Spectroscopic Studies. *J. Phys. Chem. B* **1998**, *102*, 1528–1538.

(265) Kano, H.; Kobayashi, T. Time-Resolved Fluorescence and Absorption Spectroscopies of Porphyrin J-Aggregates. *J. Chem. Phys.* **2002**, *116*, 184.

(266) Li, P.; Xu, G.; Wang, N.; Guan, B.; Zhu, S.; Chen, P.; Liu, M. 0D, 1D, and 2D Supramolecular Nanoassemblies of a Porphyrin: Controllable Assembly, and Dimensionality-Dependent Catalytic Performances. *Adv. Funct. Mater.* **2021**, *31*, 2100367.

(267) Das, J.; Maiti, D. An Atom Economical Approach for Enantioselective Cross Dehydrogenative Coupling. *Chem Catal.* **2022**, *2*, 5–7.

(268) Lin, L.; Yin, Y.; Starostin, S. A.; Xu, H.; Li, C.; Wu, K.; He, C.; Hessel, V. Microfluidic Fabrication of Fluorescent Nanomaterials: A Review. *Chem. Eng. J.* **2021**, *425*, 131511.

(269) Grover, J.; Prakash, G.; Goswami, N.; Maiti, D. Traditional and Sustainable Approaches for the Construction of C–C Bonds by Harnessing C–H Arylation. *Nat. Commun.* **2022**, *13*, 1085.

(270) Gutmann, B.; Cantillo, D.; Kappe, C. O. Continuous-Flow Technology-A Tool for the Safe Manufacturing of Active Pharmaceutical Ingredients. *Angew. Chemie Int. Ed.* **2015**, *54*, 6688–6728.

(271) McDonough, J. R.; Armett, J.; Law, R.; Harvey, A. P. Coil-in-Coil Reactor: Augmenting Plug Flow Performance by Combining Different Geometric Features Using 3D Printing. *Ind. Eng. Chem. Res.* **2019**, *58*, 21363–21371.

(272) Zhang, C.; Nandakumar, K. Enhancement of Heat Transfer in Laminar Flows Using a Toroidal Helical Pipe. *Ind. Eng. Chem. Res.* **2020**, *59*, 3922–3933.

(273) Pal, S. K.; Kanrar, B. B.; Yogeshwar, P.; Panda, D. Green Switching and Light-Harvesting Abilities of Red-Emissive Carbon Nanodot. *J. Phys. Chem. C* **2022**, *126*, 9143–9153.

(274) Panda, S.; Soni, A.; Gupta, V.; Niranjan, R.; Panda, D. PVDF-Directed Synthesis, Stability and Anion Exchange of Cesium Lead Bromide Nanocrystals. *Methods Appl. Fluoresc.* **2022**, *10*, 44005.

(275) Manzano, H.; Esnal, I.; Marqués-Matesanz, T.; Bañuelos, J.; López-Arbeloa, I.; Ortiz, M. J.; Cerdán, L.; Costela, A.; García-Moreno, I.; Chiara, J. L. Unprecedented J-Aggregated Dyes in Pure Organic Solvents. *Adv. Funct. Mater.* **2016**, *26*, 2756–2769.

(276) Würthner, F.; Kaiser, T. E.; Saha-Möller, C. R. J-Aggregates: From Serendipitous Discovery to Supramolecular Engineering of Functional Dye Materials. *Angew. Chemie Int. Ed.* **2011**, *50*, 3376–3410.

(277) Jelley, E. E. Spectral Absorption and Fluorescence of Dyes in the Molecular

State. *Nature* **1936**, *138*, 1009–1010.

(278) Spano, F. C. The Spectral Signatures of Frenkel Polarons in H- and J-Aggregates. *Acc. Chem. Res.* **2010**, *43*, 429–439.

(279) Liess, A.; Arjona-Esteban, A.; Kudzus, A.; Albert, J.; Krause, A.; Lv, A.; Stolte, M.; Meerholz, K.; Würthner, F. Organic Electronics: Ultranarrow Bandwidth Organic Photodiodes by Exchange Narrowing in Merocyanine H- and J-Aggregate Excitonic Systems. *Adv. Funct. Mater.* **2019**, *29*, 1970144.

(280) Anantharaman, S. B.; Stöferle, T.; Nüesch, F. A.; Mahrt, R. F.; Heier, J. Exciton Dynamics and Effects of Structural Order in Morphology-Controlled J-Aggregate Assemblies. *Adv. Funct. Mater.* **2019**, *29*, 1806997.

(281) Rakshit, S.; Datta, A.; Das, S. Interplay of Multiexciton Relaxation and Carrier Trapping in Photoluminescent CdS Quantum Dots Prepared in Aqueous Medium. *J. Phys. Chem. C* **2020**, *124*, 28313–28322.

(282) Datta, S.; Kato, Y.; Higashiharaguchi, S.; Aratsu, K.; Isobe, A.; Saito, T.; Prabhu, D. D.; Kitamoto, Y.; Hollamby, M. J.; Smith, A. J.; Dagleish, R.; Mahmoudi, N.; Pesce, L.; Perego, C.; Pavan, G. M.; Yagai, S. Self-Assembled Poly-Catenanes from Supramolecular Toroidal Building Blocks. *Nature* **2020**, *583*, 400–405.

(283) Niu, R.; Pan, C.; Chen, Z.; Wang, L.; Wang, L. Enhanced Thermoelectric Performance from Self-Assembled Alkyl Chain-Linked Naphthalenediimide/Single Walled Carbon Nanotubes Composites. *Chem. Eng. J.* **2020**, *381*, 122650.

(284) Lai, W. H.; Huang, S. W.; Chen, Y. H.; Cheng, C.; Liu, C. Y. Formation Mechanism of Self-Formed Triangular Pyramidal Patterns on Sapphire Substrate. *Cryst. Growth Des.* **2020**, *20*, 4811–4817.

(285) Ma, X.; Sun, R.; Cheng, J.; Liu, J.; Gou, F.; Xiang, H.; Zhou, X. Fluorescence Aggregation-Caused Quenching versus Aggregation-Induced Emission: A Visual Teaching Technology for Undergraduate Chemistry Students. *J. Chem. Educ.* **2016**, *93*, 345–350.

(286) Besford, Q. A.; Merlitz, H.; Schubotz, S.; Yong, H.; Chae, S.; Schnepf, M. J.; Weiss, A. C. G.; Auernhammer, G. K.; Sommer, J.-U.; Uhlmann, P.; Fery, A. Mechanofluorescent Polymer Brush Surfaces That Spatially Resolve Surface Solvation. *ACS Nano* **2022**, *16*, 3383–3393.

(287) Sahu, A.; Kanrar, B. B.; Panda, D. Evolution of Micron-Spaced Patterns within Precipitating Patterns of In Situ Synthesized Silver Nanoparticles in a Nanodot-Embedded PVA/PVP Film. *Langmuir* **2021**, *37*, 4460–4467.

(288) Brixner, T.; Hildner, R.; Köhler, J.; Lambert, C.; Würthner, F. Exciton Transport in Molecular Aggregates - From Natural Antennas to Synthetic Chromophore Systems. *Adv. Energy Mater.* **2017**, *7*, 1700236.

Research Publications:

S. K. Pal, V. Jha, V.; A. Mandal, E.S.S.; Iyer, D. Panda, Continuous Making, Stretch Breaking, and Exciton Dynamics of Red-Emissive Organic Submicron-sized Triangular Pyramid. *Journal of Physical Chemistry C 2023, 127, 21, 10174–10184* *(Featured on Front Cover page)*	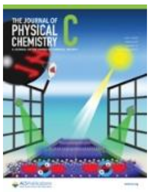
S. K. Pal, B.B. Kanrar, P. Yogeshwar, D. Panda, Green Switching and Light Harvesting Abilities of Red-Emissive Carbon Nanodot, *Journal of Physical Chemistry C 126 (2022) 9143–9153* *(Featured on Front Cover page)*	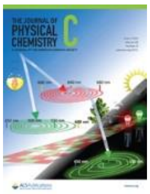
S. K. Pal, M. Parashar, B.B. Kanrar, S. Panda, N. Roy, P. Paira, D. Panda, N-doped yellow-emissive carbon nanodots from Gallic acid: reaction engineering, stimuli-responsive red emission, and intracellular localization, *Journal of Physical Chemistry C 125 (2021) 5748–5759* *(Featured on Front Cover page)*	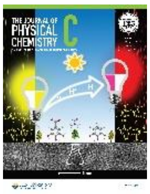
A Nandy, A Kumar, S. Dwivedi, S. K. Pal, D. Panda, Connecting the dots of Carbon Nanodots: Excitation (in) Dependency and White-Light Emission in one-step. *Journal of Physical Chemistry C 123 (2019) 20502* *(Featured on Front Cover page)*	
F. Abbas, S. Kumar, S. K. Pal, D. Panda, Carbon Nanodot doped in polymer film: Plasmophore enhancement, catalytic amination and white-light generation. *Journal of Molecular Liquids 347 (2022) 118001*	
B.B. Kanrar, S. Singh, S. K. Pal, D. Panda, Mild-temperature Organosolv Treatment of Rice-straw: Extracting Ability of Dimethyl Formamide and Material Applications. International Journal of Environmental Science and Technology, 20 (2023) 3121–3132	
S. K. Pal, B. Amulya, D. Panda Green emissive Light-harvesting system for Efficient Production of Hydrogen, 2023 (Manuscript under preparation)	
S. K. Pal, B. Singh, A. Mandal, D. Panda, Two-Birds-One-Stone: Hydrogen-bonded Organic framework for Iodine Separation and CO_2 *Sequestration, 2023 (Manuscript under preparation)*	

Participation in National & International Conference:

1.	**Presented an Oral (online):** “Cutting the Carbon-Dot Clutter: Beyond Photoluminescence" 12th National Workshop on Fluorescence and Raman Spectroscopy 29th November-4th December, 2021 Organized by **IISER Thiruvananthapuram.**
2.	**Presented a Poster (offline):** "Green Switching and Light-Harvesting Abilities of Red-Emissive Carbon Nanodot” 59th Annual Convention of Chemistry, International Conference on Recent Trends in Chemical Sciences-16th -18th Dec. 2022, Organized by **IIT(ISM) Dhanbad.**
3.	**Presented a Poster (online):** "N-Doped Yellow-Emissive Carbon Nanodots from Gallic Acid: Stimuli-Responsive Red Emission" International Conference on Aggregation-induced emission from fundamentals to applications"(ICAIEFA), 16th -18th December 2022, organized by **BITS Pilani.**
4.	**Presented a Poster (offline):** "Continuous Making and Exciton Dynamics of a Red-Emissive Organic Submicrometer-sized Triangular Pyramid" International Conference on Emerging Materials, 13th -15th July 2023, Organized by **IISER Pune.**
5.	**Presented a Poster (offline):** “Carbon Nanodot: Self-assembly of Molecular Fluorophores and Potential Applications” International Conference on Molecular Matter-Emerging Directions for Sustainability, 16-18th December 2023, organized by **IIT Madras.**
6.	**Presented a Poster (online):** "What is Carbon Nanodot? H-bonded Self-Assembly of Molecular Fluorophores" RSC Poster conference, 5-6th March 2024, organized by the **Royal Society of Chemistry (RSC)**